Design and development of calcium titanate photocatalysts for endergonic reactions with water activation

AKIHIKO ANZAI

CONTENTS

Part I: Photocatalytic CO_2 reduction with water as an electron donor over calcium titanate

Part II: Photocatalytic steam reforming of methane over calcium titanate

Introduction of Part I

Photocatalytic reduction of CO_2 with water over calcium titanate

Before the industrial revolution, atmospheric CO_2 concentration was about 280 ppm[1], which was hardly increased. However, the atmospheric CO_2 concentration has been increasing at an accelerating rate and now reached 407.8 ppm[2]. The atmospheric CO_2 concentration has increased by more than 40%. This is a result of human beings consuming a large amount of fossil fuels since the industrial revolution. Global warming is one of the most serious environmental problems for us. Climate change associated with global warming is attributed to an increase in greenhouse gases represented by CO_2 produced by human activity. To create an ecologically sustainable society, we must reduce emissions of CO_2.

Based on the above, in order to curb large-scale climate change due to an increase in CO_2 concentration, we will promote the introduction and expansion of renewable energy and reduce the amount of fossil fuel samples. Alternatively, in addition to measures such as improving the efficiency of existing energy utilization technologies, it is essential to research and develop technologies that actively reduce CO_2 emissions. Carbon dioxide capture and storage (CCS), which captures and stores CO_2, has been attracting attention as a measure to reduce CO_2 emissions into the atmosphere, but in recent years, CO_2 has been regarded as a resource, and it has been separated and recovered and recovered. There is growing interest in CCU technology that actively converts CO_2 emissions into valuable resources. As CCU technology, methanation known as Sabatier reaction, methanol synthesis, artificial photosynthesis, etc. are being promoted. Four measures are being considered to reduce CO_2 in the atmosphere. Reduce fossil fuel usage. CCS. Use new energy that does not generate CO_2. CO_2 is reduced to make useful compounds for use. CO_2 is the most oxidized carbon compound. Since it is one of the most stable molecule, in order to convert CO_2 to another carbon compound, it is necessary to reduce CO_2, that is, to inject an electron to convert CO_2.

This is because if we can build a system that converts a large amount of water existing on the earth into valuable chemicals by reducing agent and CO_2 by endergonic reaction like photosynthesis, it may be possible to solve it all at once. The reduction reaction of carbon dioxide is shown in Table 1. The multi-electron reduction reaction of CO_2 requires protons, and two two-electrons of H^+ are required to obtain CO. When the CO_2 reduction reaction is carried out in water, it competes with the hydrogen production reaction due to the reduction of protons. The equilibrium potential of carbon dioxide reduction reaction with 4 electrons or less is more likely to generate hydrogen than CO_2 reduction because the potential of hydrogen generation by reduction of protons is higher in the bubble. Therefore, it is necessary to develop a catalyst that can suppress hydrogen generation and selectively reduce CO_2.

Table 1. Here E_o^0 is the formal potential vs. the normal hydrogen electrode (NHE) under standard conditions in aqueous solution: pH = 7, 25 °C, 1 atmosphere of gases, and 1 M solutes.[3]

$CO_2 + e^- \rightarrow CO_2^{-\cdot}$	$E_o^0 = 1.90$ V	(1)
$CO_2 + 2H^+ + 2e^- \rightarrow CO + H_2O$	$E_o^0 = 0.53$ V	(2)
$CO_2 + 2H^+ + 2e^- \rightarrow HCOOH$	$E_o^0 = 0.61$ V	(3)
$CO_2 + 4H^+ + 4e^- \rightarrow HCHO + H_2O$	$E_o^0 = 0.48$ V	(4)
$CO_2 + 6H^+ + 6e^- \rightarrow CH_3OH + H_2O$	$E_o^0 = 0.38$ V	(5)
$CO_2 + 8H^+ + 8e^- \rightarrow CH_4 + H_2O$	$E_o^0 = 0.24$ V	(6)
$2H^+ + 2e^- \rightarrow H_2$	$E_o^0 = 0.41$ V	(7)

Ag is known to act as an electrochemical catalyst for CO_2 reduction, while having a high overvoltage for hydrogen production reactions. In 2011, H_2, CO, and HCOOH were obtained as Iizuka et al. Reduction products, and their total production was consistent with the production of oxygen, which is a participating product. This study was a milestone in Our research. field. After that, Table 2 summarizes the systems using Ag cocatalyst loaded semiconductor photocatalyst. Ag as a cocatalyst.

Table 2. Summary of photocatalysts for the reduction of CO_2 using water as an electron donor under similar experimental condition.

Photocatalysts	Weight / g	Volume of water / L	Light source	Formation rate of CO / µmol h^{-1}	Selectivity toward CO (%)	Ref.
Ag/$BaLa_4Ti_4O_{15}$	0.3	0.36	400-W	22	67	[4]
Ag/$NaTaO_3$:Ba	1.0	0.35	400-W	318	91	[5]
Ag/$KCaSrTa_5O_{15}$	0.5	0.35	400-W	97	87	[6]
Ag/$LaTa_7O_{19}$	0.5	0.36	400-W	25	74	[7]
Ag/$La_2Ti_2O_7$	1.0	1.0	400-W	5.2	51.5	[8]
Ag/SrO/Ta_2O_5	1.0	1.0	400-W	6.8	64.2	[9]
Ag/$ZnGa_2O_4$	1.0	1.0	400-W	155	94.8	[10]
Ag/$ZnTa_2O_6$	0.5	1.0	400-W	21.9	49.5	[11]
Ag/$Sr_2KTa_5O_{15}$	1.0	1.0	400-W	65.5	88.7	[12]
Ag/$SrNb_2O_6$	0.5	1.0	400-W	51.2	97.9	[13]
Ag/Mg−Al LDH/ Ga_2O_3	1.0	1.0	400-W	212	61.7	[14]
Ag/$SrTiO_3$:Al	0.5	1.0	400-W	5.5	98.8	[15]
Ag-Cr/CaO/$CaGa_4O_7$/Ga_2O_3	0.5 g	1.0	400-W	835	95	[16]
Ag/$CaTiO_3$	0.3	0.35	100-W	8.9	94	[17]
Ag/$Na_2Ti_6O_{13}$	0.3	0.35	100-W	2.8	82	[18]
Ag-Mn/$K_2Ti_6O_{13}$	0.3	0.4	100-W	10	98	[19]
Ag/$CaZrO_3$	0.5	1.0	400-W	2.4	65	[20]

The experimental conditions for CO_2 photocatalytic reduction were set according to the knowledge found in the literatures[21][22][23][8]. Water acts as a reducing agent in the photocatalytic reduction of CO_2, but in this reaction an aqueous bicarbonate solution is used. It is the amount of dissolved CO_2 gas can be dissolved in baicarbonate solution than pure water. As it dissolves, the amount of dissolved CO_2 increases, （ii） bicarbonate enhances CO_2 reduction rates by increasing the effective reducible CO_2 concentration in solution through rapid equilibrium exchange between the two species.

In the photocatalytic reduction of CO_2 over semiconductor photocatalysts, tiny amount of surface carbon source produce CH_4 in CO_2 reduction reactions using semiconductor photocatalysts, contaminants present in trace amounts on the surface often act as carbon sources to give methane, etc., so the balance of electrons and holes to give reduction products and oxidation products is balanced. It means that the substance that becomes the electron source is water, and its participating product is O_2. In the present study, we have developed Ag-cocatalyst loaded $CaTiO_3$ photocatalyst for reduction of CO_2 with water as an electron donor with highly selective CO. $NaHCO_3$ aqueous solution. We examined a flux method and modification by alkaline earth metal to improve the photocatalytic activity.

Semiconductors have a band structure consisting of a valence band and a conduction band in which electrons can exist, and a forbidden band, i.e., band gap in which electrons cannot exist. In the case of semiconductor materials represented by TiO_2, the band gap corresponds to the energy difference between the upper end of the valence band and the lower end of the conduction band. Figure 1 shows energy diagram of reaction by semiconductor photocatalyst. When the semiconductor photocatalyst absorbs a light whose energy is larger than the bandgap, electrons in the valence band are excited to the conduction band, and excited electrons and holes are generated in the conductor and the valence band, respectively. Many of these photoexicited carriers recombine in a short period of time to generate heat and issuance, which is energetically mitigated. Some can move to the surface of the semiconductor photocatalyst without recombination. The electrons and holes that can reach the surface contribute to the reduction reaction and oxidation reaction, respectively, according to the order of the band ends. In order to decompose CO_2 into CO and oxygen using a single photocatalyst, it is thermodynamically necessary that the bandgap sandwiches the CO_2 reduction potential and the oxygen evolution potential located between the conduction band minimum and the valence band maximum.

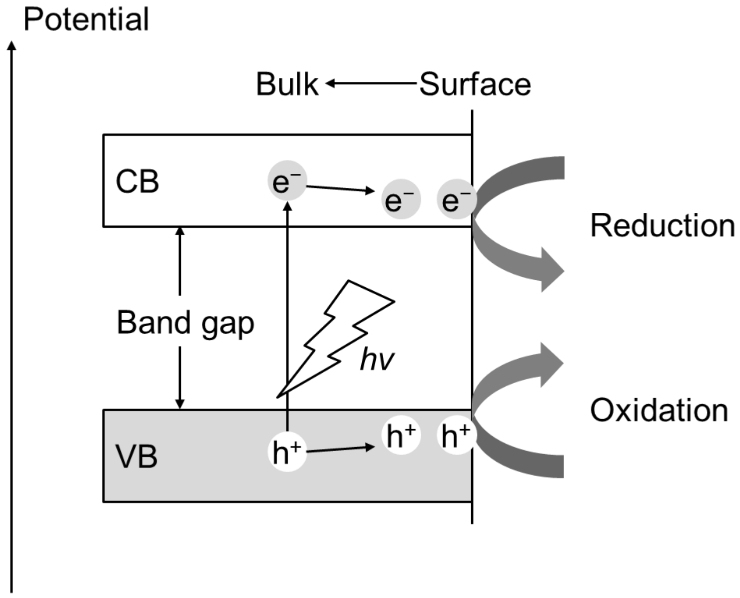

Figure 1. Energy diagram for the photocatalytic reduction of CO_2.

CaTiO$_3$ is one of the candidates for materials that meet this condition. Figure 2 shows the density of states distribution of CaTiO$_3$ and the contribution of each atom. The top of the valence band was set as zero of energy. The conduction band is mainly composed of Ti3d orbitals (examined by band structure CaTiO$_3$). The valence band is composed of 2p orbitals of oxygen. The upper end is located at V. The top of valence band was mainly formed by the O2p with little contribution from the Ca and Ti. The bottom of conduction band is mainly composed of threefold degenerate Ti3d t_{2g} orbitals. Scaife reported the relationship between flat band potential (E_{fb}) and band gap (E_g) of various metal oxide semiconductors.[24] In the case of metal oxide, the E_{fb} measured electrochemically is almost equal to the bottom of the conduction band (E_{CB}). The E_{fb} and E_g of $CaTiO_3$ are 0.6 eV and 3.5 eV, respectively. Assuming $E_{fb} = E_{CB}$, the top of the valence band (E_{VB}) is 2.9 eV. Therefore, $CaTiO_3$ has a band structure for the decomposition of CO_2 to CO since the reduction potential of CO_2 to CO and the oxidation potential of water to O_2 are located between the energy positions of E_{CB} and E_{VB}. As mentioned above, it can be said that $CaTiO_3$ is not only a unique compound, but also a resource-rich material with highly environmental friendliness because $CaTiO_3$ are composed of only ubiquitous elements (the ten most abundant elements within the Earth's crust).

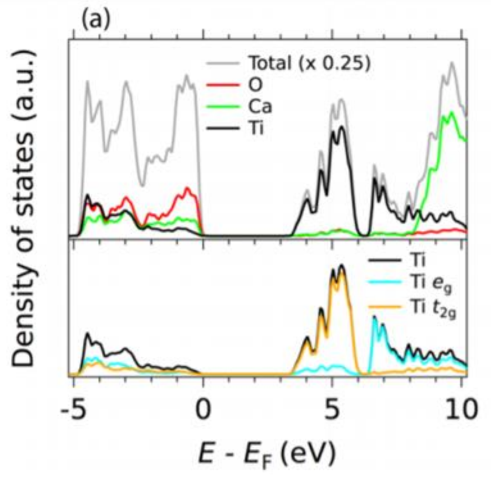

Figure 2 Density of states distribution of $CaTiO_3$ and contribution of each atom.[25]

In order to promote the photocatalytic reaction with high efficiency, electrons and holes must be separated before recombination and move to the active site on the surface. In addition, the charge transferred to the surface must be selectively consumed in the target CO_2 reduction reaction. Therefore, photocatalysts for CO_2 reduction usually modified by fine particles such as metals and metal oxides on the semiconductor surface. The modified particles here are called co-catalysts, and various materials have been developed.[26] The co-catalyst affects the band structure at the interface with the photocatalyst, promotes charge separation by trapping charges, promotes redox reactions on the surface, lowers the overvoltage of CO_2 reduction, and band bending.[27]

If all the photoexcited electrons migrated to the surface of the photocatalyst are consumed by the CO_2 reduction reaction instead of hydrogen evolution, and all the photoexcited holes migrated to the surface of the photocatalyst are consumed by oxygen evolution, the reaction proceeds according to Eq.1. That is, CO and O_2 were produced in a ratio of 2 : 1. This is the objective reaction.

$$\mathrm{CO_2(g) + 2H^+ + 2e^- \rightarrow CO(g) + H_2O(l)} \qquad E^{\mathrm{o}}(\mathrm{CO_2/CO}) = -0.106\ \mathrm{V\ vs.\ RHE} \tag{1}$$

$$\mathrm{2H^+ + 2e^- \rightarrow H_2(g)} \qquad E^{\mathrm{o}}(\mathrm{H^+/H_2}) = 0\ \mathrm{V\ vs.\ RHE} \tag{2}$$

$$\mathrm{2\ H_2O\ (l) + 4\ h^+ \rightarrow O_2(g) + 4H^+} \qquad E^{\mathrm{o}}(\mathrm{O_2/H_2O}) = +1.23\ \mathrm{V\ vs.\ RHE} \tag{3}$$

$$\mathrm{2\ CO_2\ (g) \rightarrow 2\ CO(g) + O_2(g)} \tag{4}$$

Outline of Part I

Part 1 focused on developing highly active $CaTiO_3$-based photocatalysts for CO_2 reduction to form CO using water as an electron donor. In Chapter 1, the Ag-modified $CaTiO_3$ photocatalyst was reexamined by optimizing the Ag loading amount and using a conventional photochemical reactor. It is suggested that the high photocatalytic performance in current condition originates from not only the optimized amount of cocatalyst and the high irradiation light intensity but also the high concentration of dissolved CO_2 that was achieved by a bubbling flow of CO_2 at the lower reaction temperature. In chapter 2, the structure of $CaTiO_3$ photocatalysts prepared by a flux method and a solid state reaction method and its photocatalytic activity were investigated. In chapter 3, the effect of the modification with Ag-nanoparticles and alkaline earth metal oxides on the photocatalytic activity of $CaTiO_3$ was investigated. Here, we found that the modification with Ag-nanoparticles and alkaline earth metal oxides on $CaTiO_3$ can much improved the photocatalytic activity. In chapter 4, the effect of particle size of $CaTiO_3$ photocatalyst on the photocatalytic activity was investigated. As a result of adding Ag to $CaTiO_3$ having different particle sizes and evaluating the photocatalytic activity, it was suggested that the sample having a large specific surface area had higher photocatalytic activity.

Reference

[1] W. Steffen, P. J. Crutzen, J. R. McNeill, *Ambio* **2007**, *36*, 614–621.

[2] M. Holmgren, A. Kabanshi, L. Langeborg, S. Barthel, J. Colding, O. Eriksson, P. Sörqvist, *J. Environ. Psychol.* **2019**, *64*, 48–55.

[3] J. Schneider, H. Jia, J. T. Muckerman, E. Fujita, *Chem. Soc. Rev.* **2012**, *41*, 2036–2051.

[4] K. Iizuka, T. Wato, Y. Miseki, K. Saito, A. Kudo, *J. Am. Chem. Soc.* **2011**, *133*, 20863–20868.

[5] H. Nakanishi, K. Iizuka, T. Takayama, A. Iwase, A. Kudo, *ChemSusChem* **2017**, *10*, 112–118.

[6] A. K. Tomoaki Takayama, Akihide Iwase, *Bull. Chem. Soc. Jpn.* **2015**, *88,* 538–543.

[7] T. Takayama, H. Nakanishi, M. Matsui, A. Iwase, A. Kudo, *J. Photochem. Photobiol. A Chem.* **2018**, *358,* 416–421.

[8] Z. Wang, K. Teramura, S. Hosokawa, T. Tanaka, *Appl. Catal. B Environ.* **2015**, *163*, 241–247.

[9] K. Teramura, H. Tatsumi, Z. Wang, S. Hosokawa, T. Tanaka, *Bull. Chem. Soc. Jpn.* **2015**, *88*, 431–437.

[10] K. Teramura, Z. Wang, S. Hosokawa, Y. Sakata, T. Tanaka, *Chem. - A Eur. J.* **2014**, *20*, 9906–9909.

[11] S. Iguchi, K. Teramura, S. Hosokawa, T. Tanaka, *Catal. Sci. Technol.* **2016**, *6*, 4978–4985.

[12] Z. Huang, K. Teramura, S. Hosokawa, T. Tanaka, *"Applied Catal. B, Environ.* **2016**, *199*, 272–281.

[13] R. Pang, K. Teramura, H. Asakura, S. Hosokawa, T. Tanaka, *Appl. Catal. B Environ.* **2017**, *218*, 770–778.

[14] S. Iguchi, Y. Hasegawa, K. Teramura, S. Kidera, S. Kikkawa, S. Hosokawa, H. Asakura, T. Tanaka, *Sustain. Energy Fuels* **2017**, *1*, 1740–1747.

[15] S. Wang, K. Teramura, T. Hisatomi, K. Domen, **2020**, 8779–8786.

[16] R. Pang, K. Teramura, *Commun. Chem.* **n.d.**, 1–8.

[17] A. Anzai, N. Fukuo, A. Yamamoto, H. Yoshida, *Catal. Commun.* **2017**, *100*, 134–138.

[18] X. Zhu, A. Anzai, A. Yamamoto, H. Yoshida, *Appl. Catal. B Environ.* **2019**, *243*, 47–56.

[19] X. Zhu, A. Yamamoto, S. Imai, A. Tanaka, H. Kominami, H. Yoshida, *Chem. Commun.* **2019**, *55*, 13514–13517.

[20] T. Ishii, A. Anzai, A. Yamamoto, H. Yoshida, *Appl. Catal. B Environ.* **2020**, *277*, 119192.

[21] and K. H. T. Inoue, A. Fujishima, S. Konishi, *Nature* **1979**, *277*, 637.

[22] K. Sayama, H. Arakawa, *J. Phys. Chem.* **1993**, *97*, 531–533.

[23] K. Iizuka, T. Wato, Y. Miseki, K. Saito, A. Kudo, *J. Am. Chem. Soc.* **2011**, *133*, 20863–20868.

[24] D. E. Scaife, *Sol. Energy* **1980**, *25*, 41–54.

[25] T. C. Rödel, M. Vivek, F. Fortuna, P. Le Fèvre, F. Bertran, R. Weht, J. Goniakowski, **2017**, *041121*, 1–6.

[26] J. Ran, M. Jaroniec, S. Z. Qiao, *Adv. Mater.* **2018**, *30*, 1–31.

[27] Z. Zhang, J. T. Yates, *Chem. Rev.* **2012**, *112*, 5520–5551.

Chapter 1

Highly selective photocatalytic reduction of carbon dioxide with water over silver-loaded calcium titanate

Abstract

The Ag-modified $CaTiO_3$ photocatalyst was examined by optimizing the Ag loading amount and using a conventional photochemical reactor. This revealed that the Ag-modified $CaTiO_3$ photocatalyst actually showed both high production rate of CO (54 μmol h^{-1}) and excellent selectivity toward CO formation (94%) by suppressing the H_2 production via water splitting. It is suggested that the high photocatalytic performance originates from not only the optimized amount of cocatalyst and the high irradiation light intensity but also the high concentration of dissolved CO_2 that was achieved by a bubbling flow of CO_2 at the lower reaction temperature. These reaction conditions provided ca. 40 times higher CO formation rate. It was proposed that the deposited small Ag nanoparticles are the selective active sites for CO formation and the $CaTiO_3$ crystal surface produces H_2 preferably.

Introduction

Heterogeneous photocatalytic reduction of CO_2 by using water has been widely studied as one of the possible ways to convert CO_2 to other beneficial chemicals such as CO, CH_3OH, CH_4, etc. by using solar energy[1][2][3], which is called as artificial photosynthesis[4][5][6][7]. Recently, various heterogeneous powder photocatalysts that can constantly produce CO, H_2 and O_2 with the stoichiometric ratio of the reductive and oxidative products have been reported[8][9][10][11][12][13][14][15][16], such as Cu-loaded ZrO_2[8], Ag-loaded $ALa_4Ti_4O_{15}$ (A = Ca, Sr and Ba)[9], Ag-loaded $KCaSrTa_5O_{15}$[10], Ag-loaded $La_2Ti_2O_7$[11], and Ag-loaded $ZnTa_2O_6$[12]. In these photocatalytic reaction systems, the reduction of CO_2 to CO (eq. 1) and the reduction of proton to hydrogen (eq. 2), and the oxidation of water to O_2 (eq. 3) are promoted simultaneously, and thus, the CO_2 decomposition to CO and O_2 (eq. 4) and the water decomposition to H_2 and O_2 (eq. 5) take place competitively. From the equations 1 and 3, it is obvious that water is necessary for the CO_2 decomposition as an electron source in the oxidation part.

Since the redox potential for proton (0.0 V, vs. SHE) is higher than that for CO_2 to CO (−0.12 V, vs. SHE)[17], H_2 has always been observed as the competitive reductive products through water splitting. When no other reductive products than CO and H_2 are observed in these systems, the CO selectivity, S_{CO} (%), and the ratio of the consumed electron and hole, e^-/h^+, can be calculated according to the equations 6 and 7, respectively[14], where the production rate of CO, H_2 and O_2 are referred to as R_{CO}, R_{H2} and R_{O2}, respectively.

$$CO_2 + 2\,H^+ + 2\,e^- \rightarrow CO + H_2O \tag{1}$$

$$2\,H^+ + 2\,e^- \rightarrow H_2 \tag{2}$$

$$H_2O + 2\,h^+ \rightarrow 1/2\,O_2 + 2\,H^+ \tag{3}$$

$$CO_2 \rightarrow CO + 1/2\,O_2 \tag{4}$$

$$H_2O \rightarrow H_2 + 1/2\,O_2 \tag{5}$$

$$S_{CO}\,(\%) = 100 \times R_{CO} / (R_{CO} + R_{H2}) \tag{6}$$

$$e^- / h^+ = (\text{electrons consumed for } H_2 \text{ and CO formation}) / (\text{holes consumed for } O_2 \text{ formation}) = (R_{CO} + R_{H2}) / 2\,R_{O2} \tag{7}$$

Recently, several photocatalysts have been found to exhibit high CO selectivity, i.e., higher production rate of CO than that of H_2, for example, Ag-loaded $NaTaO_3$:Ba[13], Ag-loaded $Sr_2KTa_5O_{15}$ [14], and Ag-loaded, Zn-doped Ga_2O_3[15][16]. Among them, especially, Ag/$ZnGa_2O_4$ recorded a very high CO selectivity such as 96 %[16]. In these studies, some reasons for the high CO selectivity has been proposed, e.g., the bubbling CO_2 in the presence of sodium bicarbonate ($NaHCO_3$) would increase the concentration of CO_2 as a reactant around the photocatalyst[13][14], and the number of the active sites for H_2 formation would be decreased by the loaded Ag cocatalyst[15] or the inactive surface layer such as $ZnGa_2O_4$ on Ga_2O_3 photocatalyst[16].

Calcium titanate has been studied as a photocatalyst for water splitting[18][19], photocatalytic steam reforming[19] and so on. The $CaTiO_3$ photocatalyst has a conduction band with a high potential enough to reduce both CO_2 and proton to produce CO and H_2, respectively[20]. Previously, we once reported that Ag-loaded $CaTiO_3$ polyhedral crystals can promote the photocatalytic reduction of CO_2 to produce CO and O_2 along with the water splitting to form H_2 and O_2[21], where the CO selectivity was not so high such as 45% at the steady state[21]. In the present study, we examined the Ag-loaded $CaTiO_3$ photocatalyst by optimizing Ag-loading amount and changing the reactor. As a results, the original photocatalytic activity of the Ag-loaded $CaTiO_3$ photocatalyst was uncovered, i.e., the new reaction condition much improved the photocatalytic activity of the Ag-loaded $CaTiO_3$ photocatalyst for the CO_2 reduction, not only the CO production rate but also the CO selectivity, compared to those in the previous study[21].

Experimental

Catalyst preparation

$CaTiO_3$ sample was similarly prepared via a flux method[21] from $CaCO_3$ (Kojundo 99.99%) and TiO_2 (rutile, Kojundo 99.99%) as starting materials with NaCl (Kishida 99.5%) as a flux. The starting materials and the flux were physically mixed by a mortar, where the molar ratio of $CaCO_3$ to TiO_2 was 1:1 and that of the starting materials to the flux was 4:6. The mixed powder in an aluminum crucible was heated by an electric muffle furnace up to 1373 K at a rate of 200 K h^{-1}, held at this temperature for 10 h, cooled down to 773 K at a rate of 100 K h^{-1} and then naturally cooled down to room temperature. The resulting powder was washed four times with hot water (353 K, totally 2 L). Ag cocatalyst was loaded on the surface of the $CaTiO_3$ photocatalysts by a photodeposition method. The $CaTiO_3$ powder of 1.0 g was introduced to a quartz tube with 20 ml of aqueous $NaHCO_3$ solution (1.0 mol L^{-1}) and required amount of aqueous $AgNO_3$ solution. Bubbling with a helium gas, photoirradiation was carried out using a 300 W xenon lamp for 24 h, where the light intensity was measured to be 50 mW cm^{-2} at 365±20 nm in wavelength. The irradiation wavelength was limited to the range from 350 to 500 nm by using both a UV cold mirror and an ultraviolet-cut filter. The loading amount of Ag was confirmed by X-ray florescence analysis. The obtained samples were referred as to Ag(x)/$CaTiO_3$, where x means the loading amount of Ag cocatalyst in weight %.

Characterizations

Scanning electron microscopy (SEM) image was recorded by a JEOL JSM-890 in a secondary electron detection mode. Powder X-ray diffraction (XRD) pattern was recorded by a Shimadzu Lab X XRD-6000 with Cu Kα radiation (40 kV, 30 mA). Diffuse reflectance UV–Vis spectrum was recorded on a JASCO V-670 equipped with an integrating sphere covered with $BaSO_4$ as the reference.

Photocatalytic reduction of CO_2

Photocatalytic reaction test was carried out in a commercially obtained conventional inner irradiation photochemical reactor equipped with a 100 W high pressure mercury lamp, where the light intensity was measured to be 44 mW cm^{-2} at 254±10 nm in wavelength (Table 1, Reactor B). The reaction temperature was 288 K. The irradiation area was 154.5 cm^2. The Ag(x)/$CaTiO_3$ photocatalyst powder of 0.3 g was dispersed in 360 mL of an aqueous $NaHCO_3$ solution (1.0 mol L^{-1}), where bicarbonate ion (HCO_3^-) derived from $NaHCO_3$ works as a buffer to enable the dissolution of much more CO_2 into the solution[22]. The photocatalyst was suspended with magnetically stirring in a bubbling flow of gaseous CO_2 at a flow rate of 30 mL min^{-1} for 4 h in the dark, and then the lamp was switched on to start the photocatalytic reaction. The light intensity became the maximum in a few minutes. The reaction temperature was around 288 K. The produced gases were carried with the bubbling flow of

CO_2 from the reactor and a portion was periodically sampled to be analyzed by an on-line chromatograph (Shimadzu, GC-8A, TCD, Shincarbon ST, He carrier). In order to find the other products in the liquid phase, a part of the liquid phase was sampled and analyzed by GC-MS (GCMS−Q5050).

Table 1. Reaction conditions in the previous and present studies

Reaction condition	Previous study [a]	Present study
Name of reactor	Reactor A	Reactor B
Type of reactor	homemade quarts cell	commercially obtained photochemical reactor
Light source	Xe lamp, 300 W	high pressure Hg lamp, 100 W
Location of the light source	below	in an inner jacket
Light intensity [b] / mW cm^{-2}	22	44
Light irradiation area / cm^2	19.6	154.5
Relative light intensity to the reaction mixture [c]	1.0	1.2
Volume of the aqueous solution / mL	10	360
Concentration of $NaHCO_3$ / M	1.1	1.0
Introduction of CO_2 gas	through the head space	bubbling into the solution
Flow rate of CO_2 / mL min^{-1}	3	30
Amount of catalyst / g	0.2	0.3
Reaction temperature	ca. 323 K	ca. 288 K

[a] Reference[21]. [b] Measured at 254±10 nm in wavelength. [c] Relative area intensity of the irradiation light less than 350 nm in wavelength, which was estimated from the reported spectra and the measured intensity as listed. This value might include a large error.

Results and discussion

Characterization of photocatalysts

Figure 1a shows a SEM image of the Ag(3.5)/$CaTiO_3$ photocatalyst before the reaction test. The $CaTiO_3$ particles had a polyhedral crystal shape covered with flat facets. The particle size of the $CaTiO_3$ crystals observed was in the range of 0.2−3 μm. The Ag nanoparticles with the size of 10−120 nm were observed to be deposited preferably on the selected facets. Figure 1b shows a XRD pattern of the sample, confirming the presence of $CaTiO_3$ crystallites and Ag metal particles. The average crystallites size of the Ag nanoparticles was estimated to be 31.5 nm from the diffraction at 38.1 degree by using Scherrer equation, which consists with the SEM observation. These observations are almost consistent with those in the previous study[21].

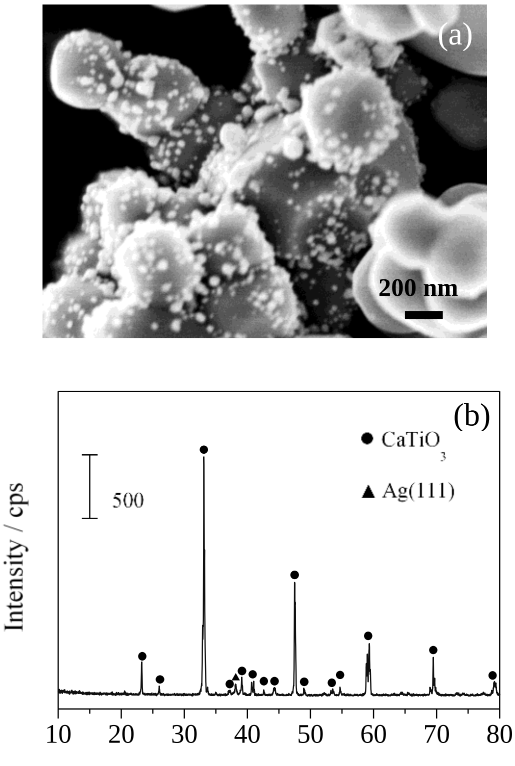

Figure 1. SEM image (a) and XRD pattern (b) of the Ag(3.5)/$CaTiO_3$ sample before use for the photocatalytic reaction test.

Photocatalytic reduction of CO_2

Figure 2 shows the time course of the production rates in the photocatalytic CO_2 reduction with water over the Ag(3.5)/$CaTiO_3$ sample in the standard condition with the CO_2 bubbling flow at 288 K. The products were mainly CO and O_2 as well as a small amount of H_2. The production rate of CO and O_2 gradually increased and that of H_2 decreased for initial 6 h. After that, the production rates became constant to be 54 μmol h^{-1} for CO and 25 μmol h^{-1} for O_2, where the former is almost two times higher than the latter. It is noted that the reduction of H^+ to H_2 was very suppressed, i.e., the rate for H_2 production at the initial and the steady state were only 6.3 and 3.1 μmol h^{-1}, respectively, even though the redox potential for H_2 formation (0.0 V, vs. SHE) is obviously higher than that for CO formation (−0.12 V, vs. SHE)[17].

Other gaseous reduction product such as methane was not detected by online TCD-GC. Any other products in the liquid phase, such as methanol, formic acid, and formaldehyde, were not detected by GC-MS. The consumed ratio of the photoexcited electrons and holes was calculated from the production rate of CO, H_2, and O_2 was almost unity ($e^-/h^+=1.1$) according to the eq. 7, meaning that the products would be almost limited to CO, H_2, and O_2. Based on these facts, the CO selectivity can be calculated as mentioned above (eq. 6). As a result, the reaction selectivity for the CO_2 reduction to CO reached 94% over the Ag(3.5)/$CaTiO_3$ photocatalyst.

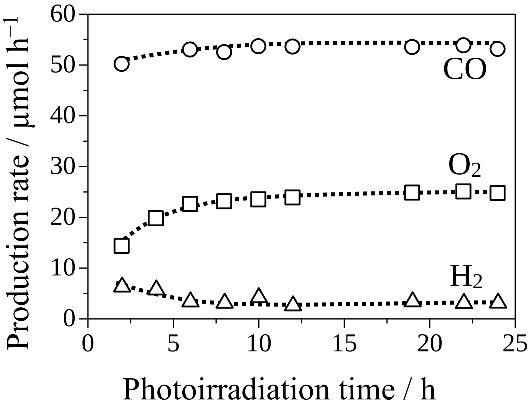

Figure 2. Time courses of the production rates of CO (circle), H_2 (triangle), and O_2 (square) in the photocatalytic reduction of CO_2 with water over the Ag(3.5)/$CaTiO_3$ sample.

In the present study, the optimum loading amount of Ag was examined and found to be 3.5 wt% as shown in Figure 3. The photocatalyst without Ag cocatalyst produced H_2 at 6.0 μmol h^{-1} as the main product and the CO very slowly at 2.2 μmol h^{-1}, where the CO selectivity was low such as 26%. This shows that the surface of the bare $CaTiO_3$ photocatalyst would be preferably responsible for the H_2 evolution and the Ag cocatalyst promotes the CO formation. It is suggested that the loading Ag cocatalyst would diminish the active sites for H_2 production on the $CaTiO_3$ surface, and thus increase the high CO selectivity.

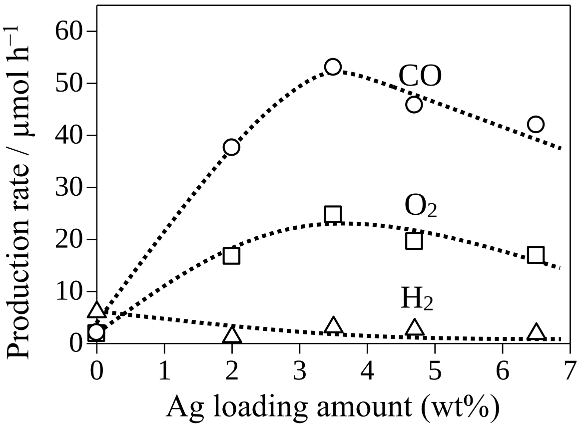

Figure 3. Production rates of CO (circle), H_2 (triangle), and O_2 (square) over various Ag(*x*)/$CaTiO_3$ photocatalysts with different loading amount of Ag cocatalyst.

The products were not detected without the photocatalyst or without photoirradiation. As mentioned above, the consumed ratio of the photoexcited electrons and holes was consistent ($e^-/h^+=1.1$). The formation rates for these products became constant and the reaction continuously proceeded for a long time in a steady state. These facts support that this reaction is evidently a photocatalytic reaction. The chemical equations for the predominant reaction can be described as follows: The photocatalytic reduction of CO_2 with photoexcited electrons and protons can form CO and water (eq. 1) and the photocatalytic oxidation of water can produce oxygen and protons (eq. 2). These equations give the total equation of the photocatalytic CO_2 splitting into CO and O_2 (eq. 3), which is a multi-photon process. Although water does not appear in the total equation, it works as an electron source.

Compared with the previous study, many parameters in the reaction condition were changed by changing the reactor as listed in Table 1, such as the amount of catalyst, the light intensity, the irradiation area, the light source giving the light with the specific wavelength distribution, the introducing method of CO_2 gas, and the reaction temperature. As a result, it is the fact that the production rate of CO was improved as 154 times larger, and also the CO selectivity was improved from 45% to 94%. The selectivity is almost the same level as, or rather slightly higher than, that reported in the electrochemical CO_2 reduction by using a Ag electrode (87%)[23], implying that the high CO selectivity would originate from the property of the Ag cocatalyst. This high selectivity is one of the highest records so far[13][16] and the best value among the heterogeneous photocatalytic CO_2 reduction with water over titanium-based photocatalysts such as Ag-loaded $BaLa_4Ti_4O_{15}$ (69%) [9] and Ag-loaded $La_2Ti_2O_7$ (51%)[11].

The reaction test was additionally performed in the reactor employed in the previous study (reactor A) with the present Ag(3.5)/$CaTiO_3$ sample (Figure 4). The production rates of CO, H_2 and O_2 were 1.3, 0.65, and 0.98 μmol h^{-1}, respectively, and the CO selectivity was 67%. Both the photocatalytic activity and the selectivity towards CO formation with the reactor A were certainly much less than those with the reactor B. When the same photocatalyst was used, the CO formation rate with the reactor B was 41 times higher than that with the reactor A. This fact evidences that the new reaction condition using the present reactor is essential for the high and selective formation of CO. To discuss the reason for the high conversion, the intensity of light that reached to the photocatalyst was roughly estimated to be 0.05 and 0.10 mW for the previous and current reactor, respectively, which were calculated by multiplying the following three values, the light intensity (22 and 44 mW cm^{-2} at 254 nm in wavelength), the photoirradiation area of the reactor (20 and 155 cm^2), and the relative area of the light emission spectra from each lamp (1.0 and 0.13, in the range of 200–350 nm in wavelength). Thus, it was confirmed that the current reactor provided 2 times larger light intensity than the previous one. It is expected that the production rate of CO would become 2 times larger. In the separate experiment, the reaction test was carried out by using 0.1 g of photocatalyst. The CO production rate was almost the same (49 μmol h^{-1}), meaning that the amount of photocatalyst around 0.1−0.3 g does not influence the production rate so much. Therefore, the difference of the light condition and the catalyst amount cannot explain the high CO formation rate such as 41 times in the present condition, even though the high light intensity would be helpful for the multi-photon reaction to some extent.

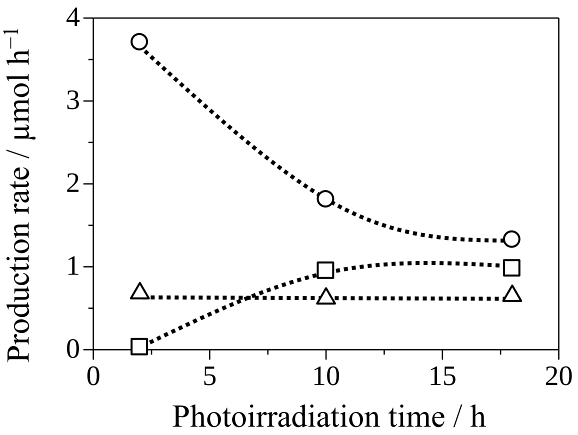

Figure 4. Time courses of the production rates of CO (circle), H_2 (triangle), and O_2 (square), in the photocatalytic reduction of CO_2 with water over the Ag(3.5)/$CaTiO_3$ sample by using the reactor A.

Here, it is suggested that another clear factor would be the flow of bubbling CO_2 directly into the liquid phase. Figure 5 shows the time course of the reaction test when the CO_2 gas was introduced to the reactor without the bubbling. The flow of CO_2 passed through the headspace of the reactor before the reaction for 24 h and also during the photocatalytic reaction. It is obvious that the formation rate of CO was lower than that with the CO_2 bubbling flow even at the initial state, and further it drastically decreased with time. This means that the CO_2 concentration in the aqueous solution would be low at the start of the reaction test and decreased further under photoirradiation. Thus, it is suggested that the bubbling flow is quite efficient for the dissolution of CO_2 into the aqueous solution. The concentration of CO_2 molecules in the liquid phase should be very important for this photocatalytic reaction. Lower reaction temperature in the present study (Table 1) would also contribute to increase the CO_2 concentration in the solution. To confirm the effect of the concentration of dissolved CO_2 in the solution, the reaction test was carried out at higher temperature (306 K) in the reactor B (Figure. 6). The production rate of H_2 was almost the same as that performed at lower temperature. But the production rate of CO was lower at higher temperature.

Therefore, selectivity towards CO formation was lower at higher temperature. This result supports that the higher concentration of dissolved CO_2 provides the higher CO production rate and the higher CO selectivity. In addition, as another possibility, the bubbles might physically facilitate the desorption of gaseous products as small bubbles from the photocatalyst surface.

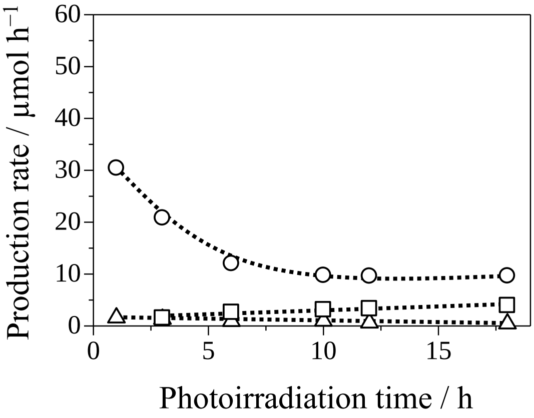

Figure 5. Time courses of the production rates of CO (circle), H_2 (triangle), and O_2 (square) in the photocatalytic reduction of CO_2 with water over the Ag(3.5)/$CaTiO_3$ sample without the CO_2 bubbling flow.

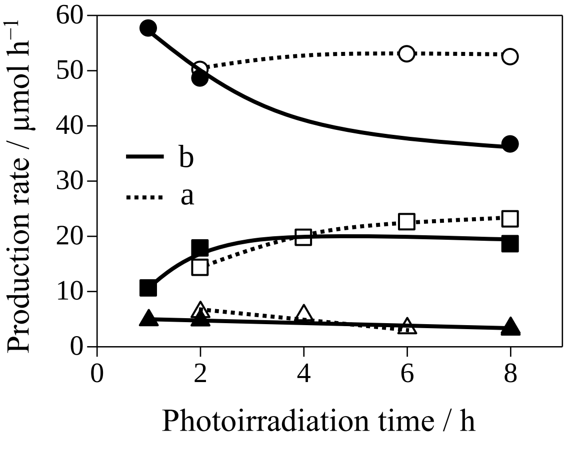

Figure 6. Time courses of the production rates of CO (circle), H_2 (triangle), and O_2 (square) in the photocatalytic reduction of CO_2 with water over the Ag(3.5)/$CaTiO_3$ sample at 288 K (a) and 306 K (b).

As mentioned above, the product selectivity varied from 89% to 94% with time at the initial period. This implies that the state of the photocatalyst might change as pointed out in the previous study[21]. Figure 7 shows diffuse reflectance UV−Vis spectra of the Ag(3.5)/$CaTiO_3$ photocatalyst before and after the photocatalytic reaction test, along with that of the pristine $CaTiO_3$ sample. The absorption bands due to the Ag nanoparticles are clearly shown in the range of 350–800 nm in wavelength. Before the reaction, a very broad band with the maximum around 520 nm was observed, which would be derived from the surface plasmon resonance of the Ag nanoparticles. After the reaction, the maximum of the band shifted to 400 nm. These bands depend on silver nanoparticle size [24]. The broad absorption band in fresh catalyst is attributed to the wide particle size distribution, while the relatively narrow absorption band in spent catalyst is attributed to the narrow particle size distribution with smaller particles. As mentioned above, Ag nanoparticles in the fresh Ag(3.5)/$CaTiO_3$ sample was in the size range 10−120 nm estimated from SEM (Figure 1) and the average crystallites size was 31.5 nm from XRD (Figure 1b). In contrast, Ag nanoparticles in the used sample had relatively narrow size distribution in the range of 20−80 nm after use as shown in the SEM image (Figure 8a), and the average crystallites size was 21.7 nm estimated from XRD (Figure 8b). In addition, Ag loading amount before and after use was almost the same, which was confirmed by XRF analysis. It is suggested that the Ag atoms of the nanoparticles on the oxidative facets are photooxidized to Ag^+ cations and dissolved in the aqueous solution, and the Ag^+ cations are photodeposited on the reductive facets to form more dispersed Ag nanoparticles. Thus, the Ag nanoparticles responsible for the CO production dispersed via the photooxidation and photodeposition process of the Ag species and diminish the number of the active sites for the H_2 production on the reductive facets of $CaTiO_3$ photocatalyst. From the above reasons, the structural variation of the Ag nanoparticles would increase the production rates of CO slightly and decreased that of H_2 by half at the early stage in Figure 2.

Here, it is notable that, although the change in the DR UV-Vis spectra was drastic during the reaction test as mentioned above (Figure 7), the change in the photocatalytic production rates in the time course was not so large (Figure 2). This means that the Ag species showing the adsorption bands in the visible light region would less contribute to the production rates while the other species would contribute dominantly. In literature, it is proposed that very small Ag nanoclusters exhibiting the absorption band around 350 nm are responsible as the efficient cocatalyst for the photocatalytic reduction of CO_2[25]. Thus, in the present system, it can be suggested that the dispersed Ag species like as small nanoclusters exhibiting the absorption band in the UV light region are the predominant cocatalyst for CO_2 decomposition.

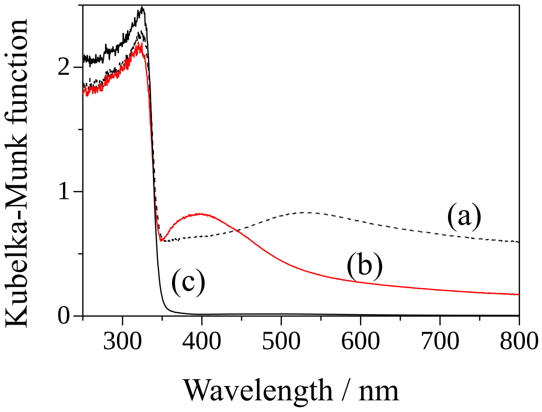

Figure 7. Diffuse reflectance spectra of the Ag(3.5)/$CaTiO_3$ sample (a) before and (b) after the photocatalytic reaction for CO_2 reduction, and (c) that of the pristine $CaTiO_3$ sample.

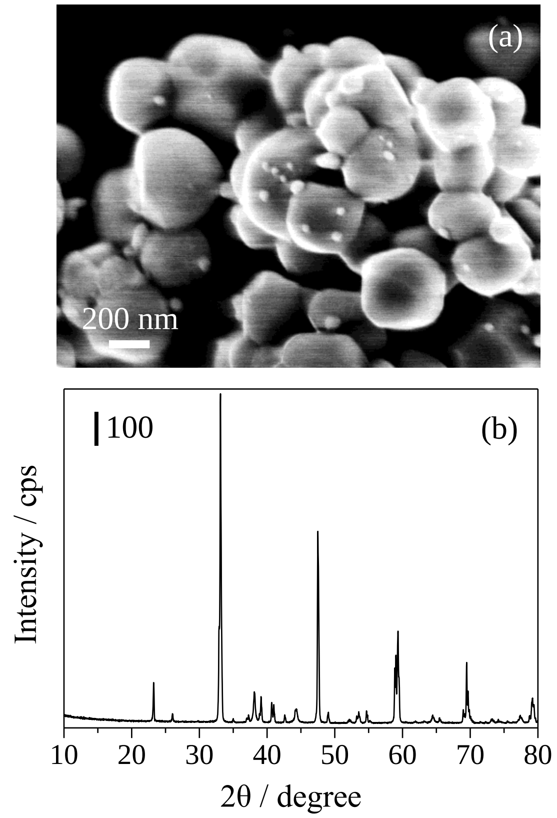

Figure 8. SEM image (a) and XRD pattern (b) of the Ag(3.5)/$CaTiO_3$ sample after use for the photocatalytic reaction test.

On the other hand, the evolution rate of O_2 at the initial stage was not consistent with the production rates of CO and H_2, where the consumed ratio of the photoexcited electrons and holes was apart from unity ($e^-/h^+=1.9$). The lack of the amount of evolved O_2 was estimated as 46 µmol. Although the reason was not clarified in this study, oxygen might be photoadsorbed on the surface of photocatalyst as pointed out in the case of TiO_2[26].

Conclusions

In conclusion, in the present study it was revealed that the Ag loaded $CaTiO_3$ crystals is one of the most selective photocatalysts for the photocatalytic CO_2 reduction into CO and O_2 in an aqueous $NaHCO_3$ solution. The selectivity for the CO_2 reduction reached 94%, where the water splitting to produce H_2 was almost suppressed even though the redox potential for H_2 formation is obviously higher than that for the CO formation. It was confirmed that the introducing gaseous CO_2 by a bubbling flow into the reaction solution is quite efficient.

References

[1] T. Inoue, A. Fujishima, S. Konishi, *Nature* **1979**, *277*, 637.

[2] J. K. M. Halmann, V. Katzir, E. Borgarello, *Sol. Energy Mater.* **1984**, *10*, 85–91.

[3] O. Ishitani|, C. Inoue, Y. Suzuki, T. Ibusuki, *J. Photochem. Photobiol. A Chem.* **1993**, *72*, 269–271.

[4] T. J. Meyer, *Acc. Chem. Res.* **1989**, *22*, 163–170.

[5] H. Inoue, T. Shimada, Y. Kou, Y. Nabetani, D. Masui, S. Takagi, H. Tachibana, **2011**, *4*, 173–179.

[6] N. S. L. and D. G. Nocera, *Proc. Natl. Acad. Sci. U. S. A.* **2006**, *103*, 15729–15735.

[7] A. Kubacka, M. Fernández-García, G. Colón, *Chem. Rev.* **2012**, *112*, 1555–1614.

[8] K. Sayama, H. Arakawa, *J. Phys. Chem.* **1993**, *97*, 531–533.

[9] K. Iizuka, T. Wato, Y. Miseki, K. Saito, A. Kudo, *J. Am. Chem. Soc.* **2011**, *133*, 20863–20868.

[10] T. Takayama, K. Tanabe, K. Saito, A. Iwase, A. Kudo, *Phys. Chem. Chem. Phys.* **2014**, *16*, 24417–24422.

[11] Z. Wang, K. Teramura, S. Hosokawa, T. Tanaka, *Appl. Catal. B Environ.* **2015**, *163*, 241–247.

[12] S. Iguchi, K. Teramura, S. Hosokawa, T. Tanaka, *Catal. Sci. Technol.* **2016**, *6*, 4978–4985.

[13] H. Nakanishi, K. Iizuka, T. Takayama, A. Iwase, A. Kudo, *ChemSusChem* **2017**, *10*, 112–118.

[14] Z. Huang, K. Teramura, S. Hosokawa, T. Tanaka, *Appl. Catal. B Environ.* **2016**, *199*, 272–281.

[15] K. Teramura, Z. Wang, S. Hosokawa, Y. Sakata, **2014**, *2*, 9906–9909.

[16] Z. Wang, K. Teramura, Z. Huang, S. Hosokawa, Y. Sakata, T. Tanaka, *Catal. Sci. Technol.* **2016**, *6*, 1025–1032.

[17] V. P. Indrakanti, J. D. Kubicki, H. H. Schobert, *Energy Environ. Sci.* **2009**, *2*, 745–758.

[18] H. Mizoguchi, K. Ueda, M. Orita, S. C. Moon, K. Kajihara, M. Hirano, H. Hosono, *Mater. Res. Bull.* **2002**, *37*, 2401–2406.

[19] K. Shimura, H. Yoshida, *Energy Environ. Sci.* **2010**, *3*, 615.

[20] J. S. Jang, P. H. Borse, J. S. Lee, K. T. Lim, O. S. Jung, E. D. Jeong, J. S. Bae, H. G. Kim, *Bull. Korean Chem. Soc.* **2011**, *32*, 95–99.

[21] H. Yoshida, L. Zhang, M. Sato, T. Morikawa, T. Kajino, T. Sekito, S. Matsumoto, H. Hirata, *Catal. Today* **2015**, *251*, 132–139.

[22] K. Teramura, K. Hori, Y. Terao, Z. Huang, S. Iguchi, Z. Wang, H. Asakura, S. Hosokawa, T. Tanaka, *J. Phys. Chem. C* **2017**, *121*, 8711–8721.

[23] Y. Hori, H. Wakebe, T. Tsukamoto, O. Koga, *Electrochim. Acta* **1994**, *39*, 1833–1839.

[24] J. J. Mock, M. Barbic, D. R. Smith, D. A. Schultz, S. Schultz, *J. Chem. Phys.* **2002**, *116*, 6755–6759.

[25] M. Yamamoto, T. Yoshida, N. Yamamoto, T. Nomoto, Y. Yamamoto, S. Yagi, H. Yoshida, *J. Mater. Chem. A* **2015**, *3*, 16810–16816.

[26] F. S. S. R. I. Bickley, *J. Catal.* **1973**, *31*, 389–397.

Chapter 2

Drastic improvement by flux mediated impurity doping in the photocatalytic activity of $CaTiO_3$ for the reduction of CO_2 in water

Abstract

Photocatalytic reduction of CO_2 with water as an electron donor is one of the attractive methods of the CO_2 utilization. $CaTiO_3$ titanate samples were prepared by a flux method. The kinds of fluxes and holding temperature during crystal growth had a large influence on the particle size, morphology, and photoabsorption bands derived from defect levels. The photocatalytic activity for the photocatalytic reduction of CO_2 with water as an electron donor was evaluated using the samples loaded with Ag-cocatalyst (Ag/$CaTiO_3$). It was found that the $CaTiO_3$ sample prepared by a flux method using NaCl as a flux at 1373 K showed 3.3 times higher photocatalytic activity than the sample prepared by a solid-state reaction method. We also found that heating in an Al_2O_3 crucible with a flux induced Al incorporation into Ti^{4+} site in the $CaTiO_3$, which presumably contributed to improving the photocatalytic activity.

Introduction

The reducing CO_2 emission have become a global issue. CO_2 utilization technologies have been developed as an important method for reducing CO_2. Among the CO_2 utilization technologies, the photocatalytic reduction of CO_2 is one of the attractive reactions in photocatalysis since it has potential to convert into valuable chemicals, namely CO[1], CH_4[2], and HCOOH,[3] etc. through photon-energy uphill reaction. Many semiconductor photocatalysts for the reaction have been developed.[4] CO is one of the most valuable chemicals since CO can be converted into a large number of carbon fuels. CO can be easily separated from water. It is known that Ag was effective metal for CO_2 reduction toward CO in the electrochemistry field.[5] Iizuka et al. reported that Ag-loaded $BaLa_4Ti_4O_{15}$ showed the photocatalytic activity for the photocatalytic reduction of CO_2 in water.[6]

We reported that Ag-loaded $CaTiO_3$ photocatalyst showed the photocatalytic activity for the photocatalytic reduction of CO_2 with water. However, the photocatalytic activity was still low.
Takata and Domen have reported that substitution of Ti^{4+} with lower-valence cations such as Al^{3+} enhances the photocatalytic activity.[7] Al is doped into $SrTiO_3$ during the flux treatment from the Al_2O_3 crucible.[8] Incorporation of Al^{3+} into $SrTiO_3$ was drastically improved the photocatalytic activity for the overall water splitting.[9] In this study, to improve the photocatalytic activity of $CaTiO_3$ photocatalyst. $CaTiO_3$ samples were prepared by a flux method in Al_2O_3 crucible with various parameters such as selection of the flux, presence or absence of the flux, and holding temperature in the molten mixture with the flux.

Experimental

Catalyst preparation

$CaTiO_3$ sample was similarly prepared via a flux method[21] from $CaCO_3$ (Kojundo 99.99%) and TiO_2 (rutile, Kojundo 99.99%) as starting materials with a flux. The starting materials and the flux were physically mixed by a mortar, where the molar ratio of $CaCO_3$ to TiO_2 was 1:1 and that of the starting materials to the flux was 1:1. The mixed powder in an aluminum crucible was heated by an electric muffle furnace up to 1373 K at a rate of 200 K h^{-1}, held at this temperature for 10 h, cooled down to 773 K at a rate of 100 K h^{-1} and then naturally cooled down to room temperature. The resulting powder was washed four times with hot water (353 K, totally 2 L).

Ag cocatalyst was loaded on the surface of the $CaTiO_3$ samples by photodeposition method. The Ag loading by the PD method was carried out in an inner-irradiation photochemical reactor, where 0.5 g of sample was dispersed in 350 mL of ion-exchanged water and an aqueous solution of $AgNO_3$ (0.5 mol L^{-1}, 93.6 µL) was added to the suspension. After Ar gas was bubbled into the suspension at a flow rate of 30 mL min^{-1} for 1.0 h, the suspension was irradiated using a 100 W high-pressure Hg lamp with a quartz jacket connected to a water-cooling system with the bubbling flow of Ar. Subsequently, the obtained powder was filtrated with suction filtration, and dried at ambient temperature in air.

Characterization

X-ray diffraction (XRD) measurement was carried out at room temperature with a Shimadzu Lab X XRD-6000 using Cu Kα radiation (40 kV, 30 mA). The crystallite size of Ag nanoparticle was determined by Scherrer equation using the full width at half maximum (FWHM) of the diffraction line at 2θ=38.1° in the XRD patterns of Ag. Images of scanning electron microscopy (SEM) was taken by a JEOL JSM-890. Diffuse reflectance (DR) UV-visible spectrum was recorded on a JASCO V-670 equipped with an integrating sphere covered with a $BaSO_4$ reference. The band gap was estimated from the spectrum according to Tauc plot.[10] The BET specific surface area was estimated from the amount of N_2 adsorption at 77 K, which was measured using a Quantachrome Monosorb MS-21. Raman spectra of solid samples were measured on a LabRam HR800 (Horiba Ltd.) spectrometer. which has a Ar^+ ion laser light source (Kimmon, IK4401R-D) with a wavelength of excitation (excitation wavelength: 488 nm).

Photocatalytic activity test

The reaction tests for photocatalytic reduction of CO_2 with water were carried out in the inner-irradiation photochemical reactor mentioned above, as described in our previous study.[11] The photocatalyst powder of 0.3 g was dispersed in 350 mL of an aqueous $NaHCO_3$ solution (0.5 mol L^{-1}), where bicarbonate ions (HCO_3^-) worked as a buffer (pH=ca. 9) to enrich molecular CO_2 in the solution.[12] The photocatalyst was suspended with magnetically stirring in a bubbling flow of gaseous CO_2 at a flow rate of 30 mL min^{-1} for 1 h in the dark, and then the lamp was switched on to start the photocatalytic reaction. The gaseous products were sampled by a six-way valve and analyzed by an online gas chromatograph with a thermal conductivity detector (Shimadzu, GC-8A, Shincarbon ST, Ar carrier). The CO selectivity, S_{CO} (%), can be calculated as follows (eq. 1), where the production rate of CO, H_2 and O_2 are referred to as R_{CO}, R_{H2} and R_{O2}, respectively. The ratio of the consumed electron and hole for products formation, $R(e^-/h^+)$, can be calculated as follows (eq. 2).

$$S_{CO}\ (\%) = 100 \times R_{CO} / (R_{CO} + R_{H2}) \quad (1)$$

$$R(e^-/h^+) = (\text{electrons consumed for } H_2 \text{ and CO formation}) / (\text{holes consumed for } O_2 \text{ formation}) \quad (2)$$

$$= (R_{CO} + R_{H2}) / 2\, R_{O2}$$

Results and discussion

Figure 1 shows XRD patterns of calcium titanates prepared using various flux. All the samples showed clear diffraction lines assignable to orthorhombic calcium titanate crystal and no other diffraction lines from impurity was observed in these profiles. The (242) peak at 69.5° of orthorombic $CaTiO_3$ phase for the bulk samples is enlarged shown in Figure 1. Using $CaCl_2$, LiCl, NaCl, and KCl flux, the diffraction peak was slightly shifted to a higher angle. Using RbCl flux, the diffraction peak was not shifted. There are two possibilities for the phenomena. (i) Ions derive from a flux substitute for the Ca^{2+} in the A-site. (ii) Al^{3+} ions derive from alumina crucible substitute for the Ti^{4+} ion in the B-site. Ionic radii of 12-coordinated Li^+ ion (1.25 Å) was smaller than that of Ca^{2+} (1.34 Å). Ionic radii of 6-coordinated Al^{3+} ion (0.535 Å) also smaller than that of Ti^{4+} (0.605 Å). On the other hand, ionic radii of 12-coordinated Na^+ ion (1.39 Å), K^+ ion (1.64 Å), and Rb^+ ion (1.72 Å) was larger than that of Ca^{2+} (1.34 Å). In the sample prepared by a flux method using LiCl as a flux, (i)The Li^+ ions substitute for Ca^{2+} ions. (ii) The Al^{3+} ions substitute for Ti^{4+} ions. (iii) The Li^+ ions substitute for Ca^{2+} ions and the Al^{3+} ions substitute for Ti^{4+} ions, simultaneously. While in the sample prepared by a flux method using $CaCl_2$, NaCl, KCl, and RbCl as a flux, the case (ii) occur.

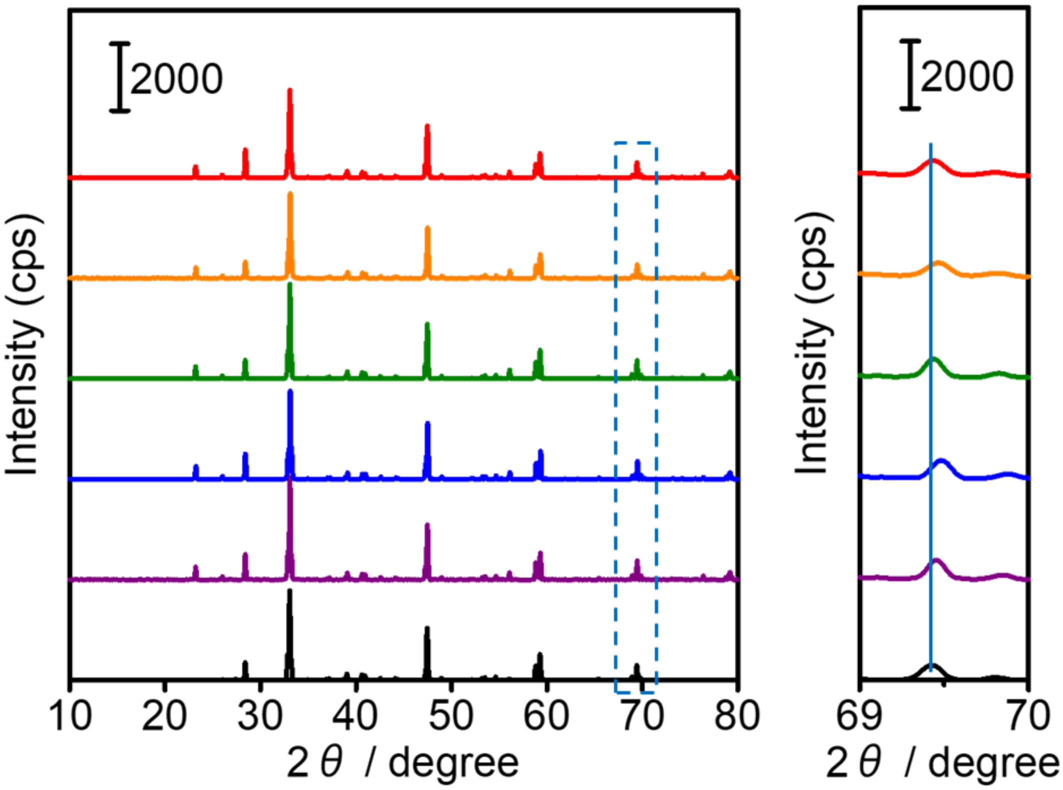

Figure 1 XRD patterns of the prepared $CaTiO_3$ samples heated at 1373 K for 10 h in $CaCl_2$ flux (a), LiCl flux (b), NaCl flux (c), KCl flux (d), RbCl flux (f), and without flux (g).

Figure 2 shows Raman spectra of calcium titanates prepared using various flux. In all samples, the bands derive from $CaTiO_3$-based material appeared.[14] The another band at 800 cm^{-1} appeared when NaCl was used as a flux. This band attributed to an A_{1g} mode, symmetrical octahedral breathing mode of the oxygens. This mode is inactive for compositions with single B-site species.[15] This indicated that another ion occupied the Ti^{4+} ion in the B-site or Ti cation vacancies, V_{Ti}'''', was introduced. Given the XRD results, this indicated that the Al^{3+} occupied the Ti^{4+} ion in the B-site. No A_{1g} band appeared when LiCl, $CaCl_2$, and KCl were used as a flux, although the higher angle shifts were observed in the XRD patterns. Li^+ ions occupied only the Ca^{2+} ion in the

A-site. Tiny amount Al^{3+} ion, which is not enough to give peak of A_{1g} mode, occupied the Ti^{4+} ion in the B-site. The intensity of A_{1g} band decrease with introducing oxygen vacancies.[16] There would be some effect of oxygen vacancy formation.

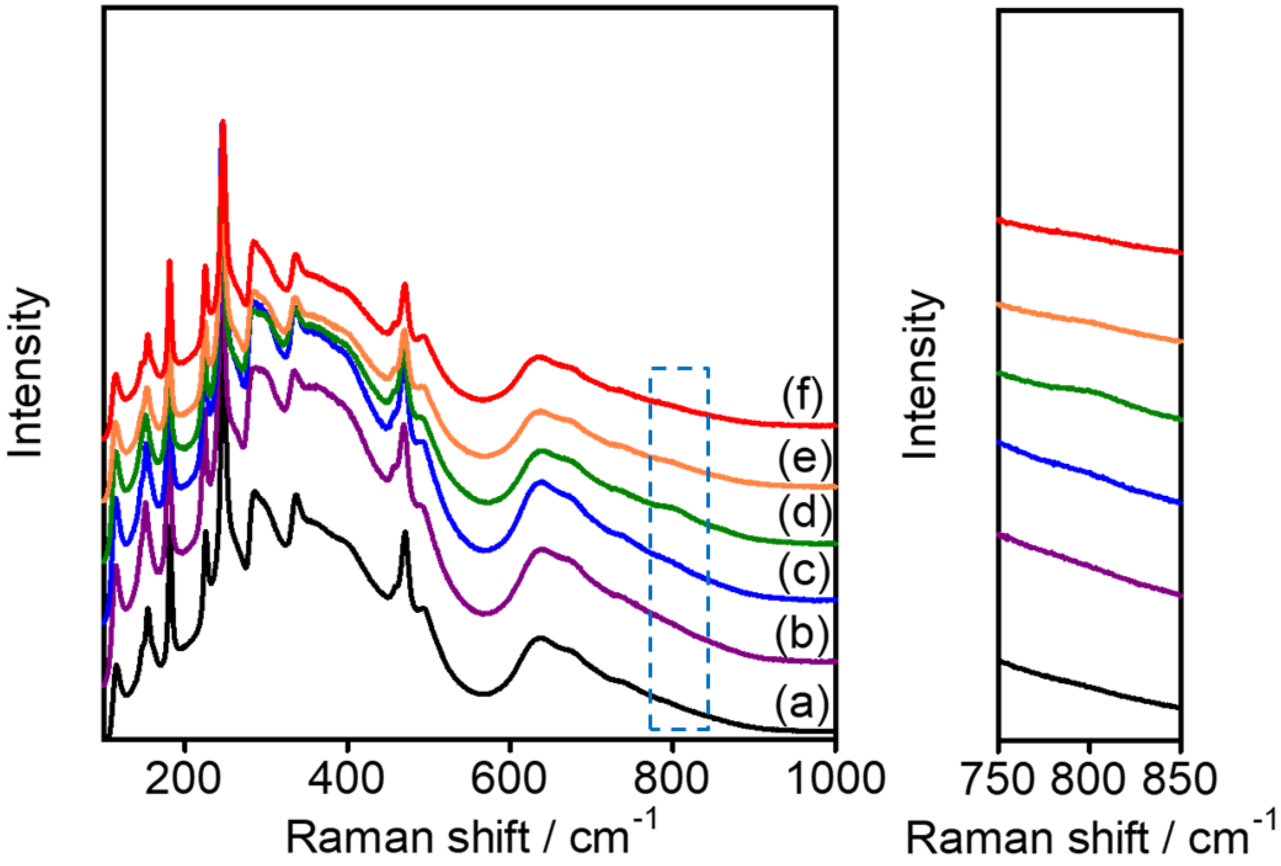

Figure 2 Raman spectra of the prepared $CaTiO_3$ samples heated at 1373 K for 10 h in $CaCl_2$ flux (a), LiCl flux (b), NaCl flux (c), KCl flux (d), RbCl flux (f), and without flux (g).

Figure 3 shows difuse reflectance absorption spectra of the samples. All sample showed the absorption band derive from band to band transition. It is noticed that there are small characteristic absorption bands at 350-400 nm and 420-800 nm. Absorbance drastically changed by flux. The absorption near the absorption edge appeared strongly in the sample prepared by solid state reaction method. However, the absorption around 370 nm decreased in the sample prepared by flux method. Former band would be amorphous TiO_2 species or the structure related to the degree of disorder, bond angle distortions or deep defects such as dangling bond. When $CaCl_2$ and LiCl were used, large absorption around 420-800 nm appeared. When NaCl was used, the intensity of this band is medium. When KCl and RbCl were used, small absorption gave small absorption appered. It can be assumed that oxygen vacancies, $V_O^{\cdot\cdot}$, introduced into the $CaTiO_3$ by Al^{3+} doping in order to maintain a charge neutrality as below.

$Al_2O_3 = 2Al_{Ti}^{'} + 3O_O^{\times} + V_O^{\cdot\cdot}$

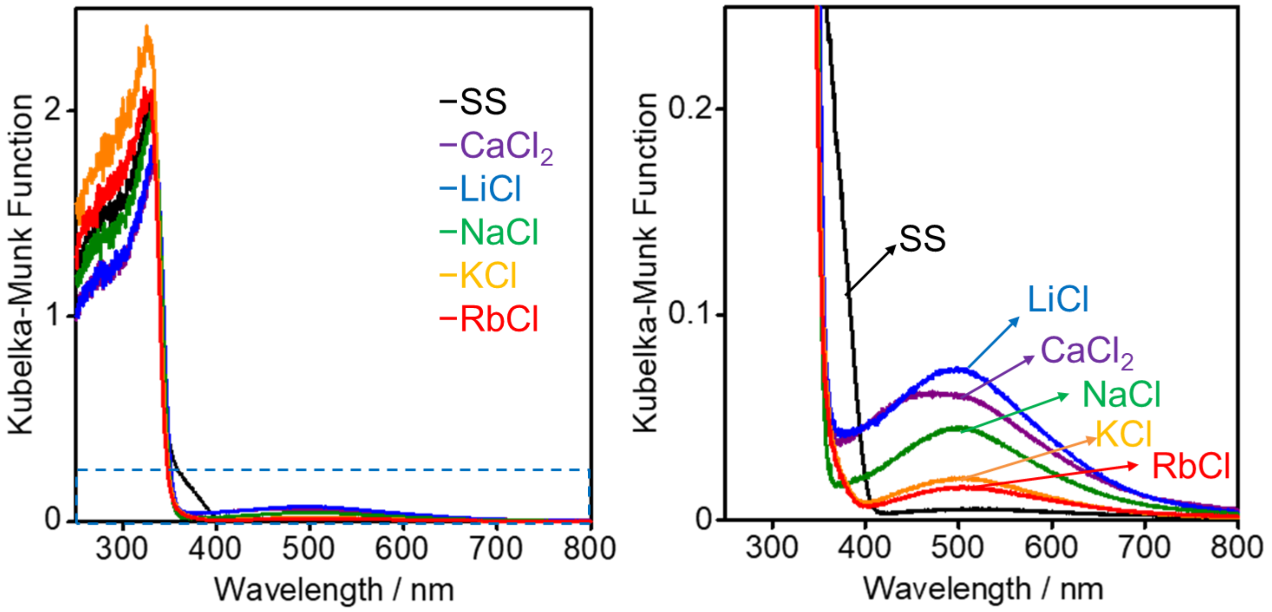

Figure 3 Diffuse reflectance UV–Vis spectra of the prepared $CaTiO_3$ samples heated at 1373 K for 10 h in $CaCl_2$ flux (a), LiCl flux (b), NaCl flux (c), KCl flux (d), RbCl flux, and without flux

(f).XRD patterns of the prepared $CaTiO_3$ samples heated at 1373 K for 10 h in $CaCl_2$ flux (a), LiCl flux (b), NaCl flux (c), KCl flux (d), RbCl flux (f), and without flux (g).

Figure 4 shows SEM images of the samples. solid state reaction method irregular shape particle. The average particle size is around 1 µm. The samples prepared by a flux method using CaCl2 as a flux shows cubic shape particle. The size of particle was around 2 µm. The samples preapared by a flux method using LiCl, NaCl, KCl, and RbCl shows polyhedral shape particle. The order in size of these particle was LiCl > NaCl > KCl > RbCl.

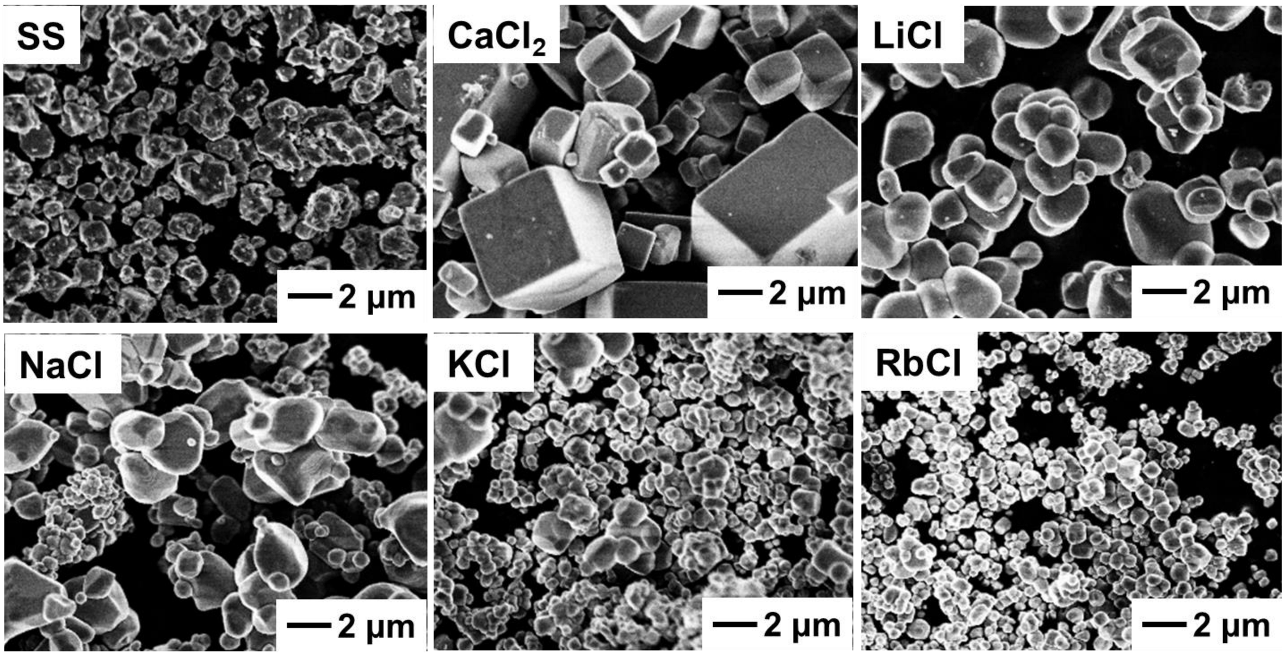

Figure 4 SEM images of the prepared $CaTiO_3$ samples heated at 1373 K for 10 h in $CaCl_2$ flux (a), LiCl flux (b), NaCl flux (c), KCl flux (d), RbCl flux, and without flux (f).XRD patterns of the prepared $CaTiO_3$ samples heated at 1373 K for 10 h in $CaCl_2$ flux (a), LiCl flux (b), NaCl flux (c), KCl flux (d), RbCl flux (f), and without flux (g).

Photocatalytic activity

A typical time course of photocatalytic reduction of CO_2 in aqueous $NaHCO_3$ solutin over Ag (3.5 wt %)/$CaTiO_3$ (sample B, Table 1) is shown in Figure 5. CO and O_2 evolved steadily and stoichiometrically with tiny amount of H_2 evolution after 4 h. The ratio of consumed electrons and holes was almost unity, $R(e^-/h^+)=1.1$. This suggests that the photocatalytic CO_2 reduction into CO and O_2 proceeded using water as a reducing agent.

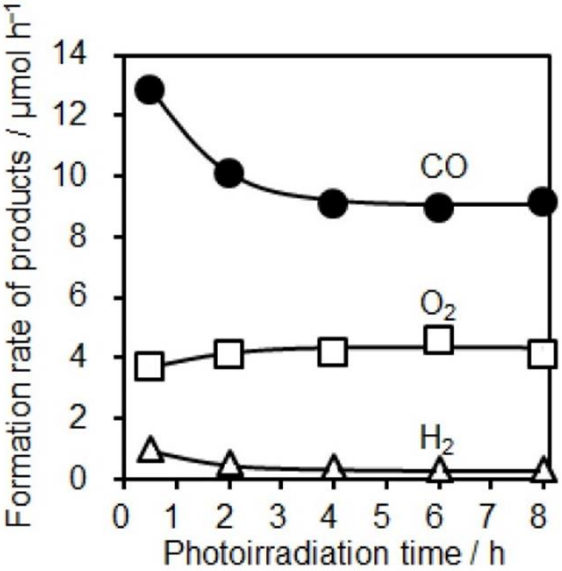

Figure 5 Time courses of the production rates of CO (closed circles), H_2 (closed triangles), and O_2 (open squares) in the photocatalytic reduction of CO_2 with water over the Ag(3.5 wt%)/$CaTiO_3$ (NaCl, 1373) sample. Amount of photocatalyst: 0.3 g, volume of reaction solution (H_2O): 350 mL, additive: 0.5 M $NaHCO_3$, CO_2 flow rate: 30 mL min^{-1}, and light source: 100 W high pressure Hg lamp with a quarts jacket.

Figure 6 shows the formation rates of CO, O_2, and H_2 for the photocatalytic reduction of CO_2 with water over Ag-loaded $CaTiO_3$ photocatalyst prepared by a solid state reaction method and a flux method. Compared with the sample prepared by a solid state method, the sample prepared by using $CaCl_2$ and NaCl as the flux showed much higher photocatalytic activity more than two times. Among them, the sample prepared by using NaCl as the flux showed the highest CO formation rate (9 µmol

h^{-1}). This was three times higher than that prepared by a solid state reaction method. When LiCl was used as a flux, the CO formation rate was almost the same as that prepared by a solid state reaction method. However, the sample prepared using KCl and RbCl as a flux shoed lower photocatalytic activity than the sample prepared by a solid state reaction method.

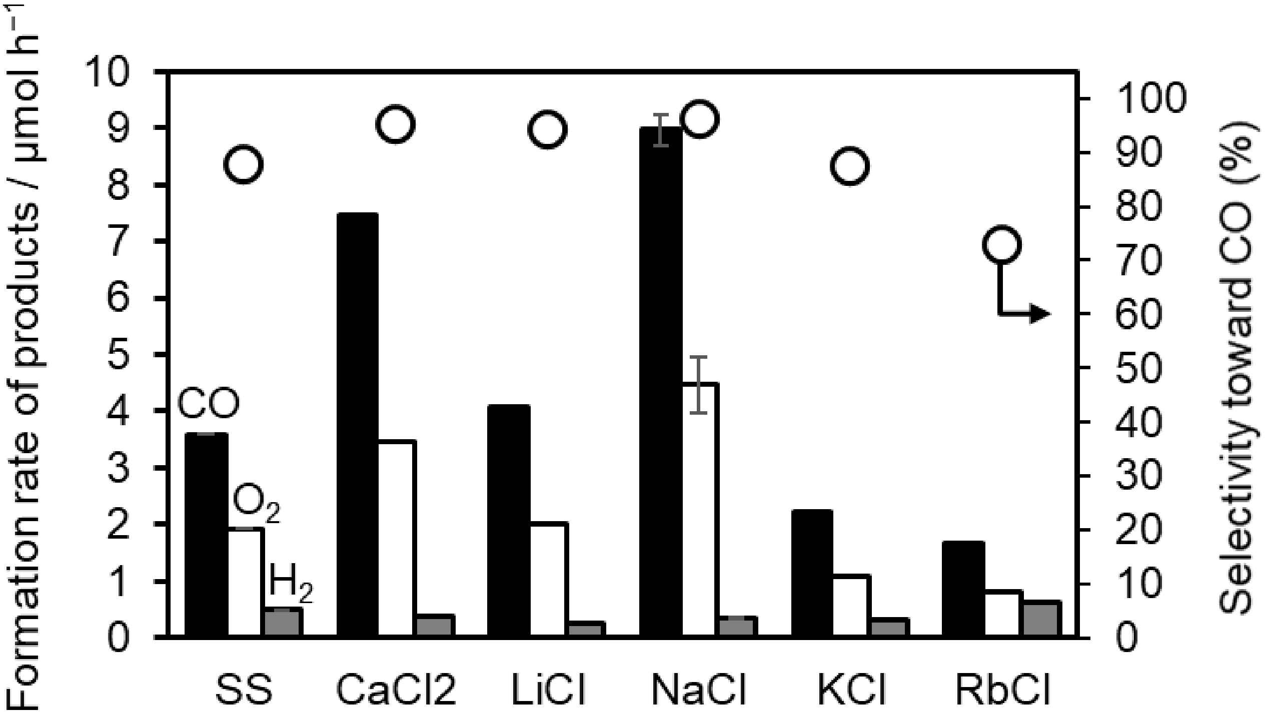

Figure 6 Formation rates of CO(black), O_2(white), and H_2(gray) and CO selectivity (closed circles) in the photocatalytic CO_2 reduction tests with various photocatalyst samples, (a) the Ag/CTO sample, (b) Ag/$CaTiO_3$ ($CaCl_2$), (c) Ag/$CaTiO_3$ (LiCl), (d) Ag/$CaTiO_3$ (KCl), (e) Ag/$CaTiO_3$ (RbCl). The values shown here were recorded after 8 h from the start of the photoirradiation. Amount of photocatalyst: 0.3 g, volume of reaction solution (H_2O): 350 mL, additive: 0.5 M $NaHCO_3$, CO_2 flow rate: 30 mL min^{-1}, and light source: 100 W high pressure Hg lamp with a quarts jacket.

Yamakata et al. elucidated that Al doping prolongs the lifetime of shallowly trapped electrons.[17] In our case, the Al substitution would contribute to prolong the life time of photoexcited electron. This might be one of the possible reason why the sample prepared by a flux method using NaCl flux showed high photocatalytic activity.

Conclusions

We found that $CaTiO_3$ photocatalyst prepared by a flux method using NaCl as a flux exhibited much higher photocatalytic activity for the photocatalytic reduction of CO_2 in aqueous $NaHCO_3$ solution. The $CaTiO_3$ crystal had well-defined polyhedral shaped crystals. Al^{3+} ions derive from alumina crucible were incoorpotated into the Ti^{4+} site in B-site. The incorporation of Al^{3+} ion attributed unique defect structure, such as oxygen vacancies and Ti vacancies. This would contribute the high photocatalytic activity.

References

[1] R. Pang, K. Teramura, *Commun. Chem.* **n.d.**, 1–8.

[2] O. Ishitani|, C. Inoue, Y. Suzuki, T. Ibusuki, *J. Photochem. Photobiol. A Chem.* **1993**, *72*, 269–271.

[3] S. Sato, T. Arai, T. Morikawa, K. Uemura, T. M. Suzuki, H. Tanaka, T. Kajino, **2011**, 15240–15243.

[4] S. N. Habisreutinger, L. Schmidt-mende, J. K. Stolarczyk, **2013**, 7372–7408.

[5] Y. Hori, H. Wakebe, T. Tsukamoto, O. Koga, *Electrochim. Acta* **1994**, *39*, 1833–1839.

[6] K. Iizuka, T. Wato, Y. Miseki, K. Saito, A. Kudo, *J. Am. Chem. Soc.* **2011**, *133*, 20863–20868.

[7] T. Takata, K. Domen, **2009**, 19386–19388.

[8] Y. Ham, T. Hisatomi, Y. Goto, Y. Moriya, Y. Sakata, A. Yamakata, J. Kubota, K. Domen, *J. Mater. Chem. A* **2016**, *4*, 3027–3033.

[9] T. Takata, J. Jiang, Y. Sakata, M. Nakabayashi, N. Shibata, V. Nandal, K. Seki, T. Hisatomi, K. Domen, *Nature* **2020**, *581*, DOI 10.1038/s41586-020-2278-9.

[10] J. Tauc, R. Grigorovici, A. Vancu, *Phys. Status Solidi* **1966**, *15*, 627–637.

[11] A. Anzai, N. Fukuo, A. Yamamoto, H. Yoshida, *Catal. Commun.* **2017**, *100*, 134–138.

[12] K. Teramura, K. Hori, Y. Terao, Z. Huang, S. Iguchi, Z. Wang, H. Asakura, S. Hosokawa, T. Tanaka, *J. Phys. Chem. C* **2017**, *121*, 8711–8721.

[13] Z. Huang, K. Teramura, S. Hosokawa, T. Tanaka, *Appl. Catal. B Environ.* **2016**, *199*, 272–281.

[14] H. Zheng, I. M. Reaney, G. D. C. C. De Gyo, **2004**.

[15] J. A. Phys, **2017**, *114110*, DOI 10.1063/1.3592192.

[16] E. Sediva, T. Defferriere, N. H. Perry, H. L. Tuller, J. L. M. Rupp, **2019**, *1902493*, 1–9.

[17] A. Yamakata, H. Yeilin, M. Kawaguchi, T. Hisatomi, J. Kubota, Y. Sakata, K. Domen, *"Journal Photochem. Photobiol. A Chem.* **2015**, *313*, 168–175.

[18] and R. F. Robert Lowndes, Marco Deluca, Feridoon Azough, *J. Appl. Phys.* **2013**, *113*, 044115.

Chapter 3

Photocatalytic Reduction of Carbon Dioxide by Water over Calcium Titanate with a Silver-Magnesium Cocatalyst

Abstract

Photocatalytic CO_2 reduction has attracted attention as an artificial photosynthesis. To improve photocatalytic activity of $CaTiO_3$ photocatalyst for CO_2 conversion, modification with Ag-nanoparticles and alkaline earth metal oxides was examined. As a result, the photocatalytic activity was successfully improved by the synergetic effect of Ag and alkaline earth metal oxide species. The addition of MgO species enhanced the photocatalytic activity of Ag loaded $CaTiO_3$ by 2 times, where the CO formation rate was 7 µmol h^{-1} and the CO selectivity was as high as 98%.

Introduction

There are urgent requirements for not only reducing atmospheric CO_2 as one of greenhouse gases but also utilizing CO_2 as a carbon source. Conversion of CO_2 into valuable compounds such as CO, CH_3OH, and CH_4 by photocatalysis using solar energy would be one of significantly valuable strategies for realizing a sustainable low-carbon society[1]. Recently, heterogeneous photocatalytic CO_2 reduction by using water as an electron source has been widely studied.[2] On conducting the photocatalytic CO_2 reduction in an aqueous solution, CO is one of the most useful products among the possible products from CO_2 mentioned above, because it can be easily separated from the aqueous solution into the gas phase and catalytically converted with H_2 into various chemical intermediates for industrial use. [3]

In aqueous solution, the photocatalyst can reduce proton also by the photoexcited electron as a competitive reaction. The reduction of proton is thermodynamically preferred compared with the CO_2 reduction to CO, i.e., the redox potential of CO_2 to CO (−0.53 V vs normal hydrogen electrode (NHE) at pH=7, 298 K, 1 atm) is more negative than that of proton to H_2 (−0.41 V)[4]. Therefore, in order to improve the efficiency of photocatalytic reduction of CO_2 to CO with water, it is necessary to design the photocatalyst to reduce CO_2 selectively in the presence of water.

Iizuka et al. reported that Ag cocatalyst-loaded $BaLa_4Ti_4O_{15}$ photocatalyst can preferentially reduce CO_2 to CO using water as an electron donor,[5] where Ag cocatalyst deposited on the photocatalyst surface plays an important role for the photocatalytic reduction of CO_2. After this research, many kinds of Ag-loaded photocatalysts have been reported, e.g., Sr-doped $NaTaO_3$,[6] $KCaSrTa_5O_{15}$,[7] $LaTa_7O_{19}$,[8] $Sr_2KTa_5O_{15}$,[9] Zn-doped Ga_2O_3,[10] $SrNb_2O_6$,[11] $La_2Ti_2O_7$[12], and so on. Our group has also developed highly selective photocatalytic CO_2 reduction with water using several Ag loaded titanate photocatalysts, such as Ag/$CaTiO_3$[13], Ag/$Na_2Ti_6O_{13}$,[14] and Ag-MnO_x/$K_2Ti_6O_{13}$,[15] where the CO selectivity reached to 74–98%. Among them, Ag-loaded $CaTiO_3$ photocatalyst exhibits high activity for CO_2 reduction.[10] However, the photocatalytic activity was still low, which should be further improved.

In order to achieve highly efficient CO_2 reduction, improvement of CO_2 adsorption properties on the photocatalyst surface is an important point. Alkaline earth metal oxides are typical solid bases.

Its high CO_2 adsorption capacity is well known.[16] It has been reported that a surface modification of photocatalyst by alkaline earth metal oxides for adsorbing CO_2 is effective to improve the photocatalytic performance for CO_2 reduction.[17][18][19][20]

In the present study, the surface modification with alkaline earth metal oxide species such as MgO and Ag cocatalyst on a $CaTiO_3$ photocatalyst was examined to improve the photocatalytic activity for CO_2 reduction with water. As a result, the surface modification with alkaline earth metal oxide species significantly improved the photocatalytic activity of Ag-loaded $CaTiO_3$ photocatalyst. Especially, a $CaTiO_3$ photocatalyst modified with a Ag-Mg cocatalyst exhibited 2 times higher CO evolution rate (7 μmol h^{-1}) than the Ag-loaded $CaTiO_3$ photocatalyst and a very high selectivity (98%) was achieved in the present conditions.

Experimental

Preparation of photocatalysts

$CaTiO_3$ photocatalyst (denoted as CTO hereafter) was synthesized by a conventional solid-state reaction method. The starting materials, $CaCO_3$ (Kojundo, 99.99%) and TiO_2 (rutile, Kojundo, 99.9%), were mixed in an alumina mortar in the presence of ethanol. The mixture was heated in an aluminum crucible covered by a lid at a rate of 10 K min^{-1} to 1373 in an electric furnace, and held at this temperature for 10 h, followed by natural cooling to room temperature in the furnace.

Loading cocatalysts

The CTO samples modified with alkaline-earth metal oxide (AO), that is MgO, CaO, SrO, and BaO, were prepared by an impregnation method. The synthesized CTO sample was dispersed into 50 mL of an aqueous solution including a required amount of $A(NO_3)_2$ (A=Mg, Ca, Sr, or Ba). The suspension was dried up at 353, followed by calcination in an electric muffle furnace at typically 1023 for 2 h in an air atmosphere. The obtained samples loaded with *x* mol% of alkaline-earth metal oxide are referred to as AO(*x*)/CTO, e.g., MgO(5)/CTO, and if necessary, the calcination temperature is shown as AO(*x*)/CTO_*y*K, e.g. Sr(3)/CTO_773. In practice, the amount of AO species in the samples decreased by the deposition of Ag as mentioned later due to leaching into the aqueous solution (Table 1). For convenience, the value of *x* mol% in the sample name shows the initially loaded amount of alkaline-earth metal oxide.

Ag co-catalyst was loaded on the surface of the prepared CTO and AO/CTO samples by a photodeposition method. The CTO or AO/CTO powder of 0.5 g was introduced to a commercially-obtained conventional inner-irradiation photochemical reactor equipped with a 100 W high pressure mercury lamp (UM102) with 350 mL of an aqueous $NaHCO_3$ solution (0.5 mol L^{-1}) containing a required amount of $AgNO_3$. The pH value of this solution was ca. 8. The mixture was magnetically stirred in a bubbling flow of gaseous CO_2 at a flow rate of 30 mL min^{-1} for 1 h in the dark, photoirradiated for 5 h, and filtered with suction, and then dried overnight at 353. The loading amount of Ag was 4.2 mol% in the present study. The notation was omitted. The obtained samples were referred to as Ag/AO(*x*)/CTO such as Ag/MgO(5)/CTO.

Characterization of photocatalysts

X-ray diffraction (XRD) measurement was carried out at room temperature with a Shimadzu Lab X XRD-6000 using Cu Kα radiation (40 kV, 30 mA). The crystallite size was determined by Scherrer equation using the full width at half maximum (FWHM) of the diffraction line at 2θ=33.1° in the XRD patterns of $CaTiO_3$. The equation was used only if it does not exceed the limit of the equation, i.e. 100–200 nm.[21] Composition analysis was conducted on a Shimadzu EDX-8000 energy dispersive X-ray fluorescence spectrometer (XRF). Images of scanning electron microscopy (SEM) was taken by a JEOL JSM-890. Diffuse reflectance (DR) UV-visible spectrum was recorded on a JASCO V-670 equipped with an integrating sphere covered with a $BaSO_4$ reference. The band gap was estimated from the spectrum according to Tauc plot.[22] The BET specific surface area was estimated from the amount of N_2 adsorption at 77 K, which was measured using a Quantachrome Monosorb MS-21.

Sr K-edge X-ray absorption fine structures (XAFS) were recorded at NW-10A of the Photon Factory (KEK, Tsukuba, Japan). The spectra of the reference samples were measured in a transmission mode, while the spectra of the prepared samples were measured in a fluorescence mode due to the small amount of the Sr species.

Transmission infrared spectra of the samples after reaction were recorded with a JASCO FT/IR-4700 at room temperature by the KBr pellet method. The solid after the reaction was dried at 353 overnight to obtain a measurement sample. KBr powder was ground in an agate mortar, and then the KBr powder and the sample were dried at 383 for three hours. 3 mg of the sample was mixed with 300 mg of the KBr powder. The mixture was pelletized under approximately 10 MPa pressure for 3 min. The background was measured with a pure KBr pellet.

Images of transmission electron microscopy (TEM) and scanning transmission electron microscopy (STEM) with energy dispersive X-ray analysis (EDX) were taken by a JEOL JEM-2100F at 200 kV in the Joint Research Centre of Kindai University. The samples were dispersed in methanol and sonicated for 5 min, dropped onto a carbon-coated copper grid, and dried at ambient temperature for 5 h.

Photocatalytic reaction tests

The reaction tests for photocatalytic reduction of CO_2 with water were carried out in the inner-irradiation photochemical reactor mentioned above as described in our previous studies.[13] The photocatalyst powder of 0.3 g was dispersed in 350 mL of an aqueous $NaHCO_3$ solution (0.5 mol L^{-1}), where bicarbonate ions (HCO_3^-) worked as a buffer (pH=ca. 9) to enrich molecular CO_2 in the solution.[23] The photocatalyst was suspended with magnetically stirring in a bubbling flow of gaseous CO_2 at a flow rate of 30 mL min^{-1} for 2 h in the dark, and then the lamp was switched on to start the photocatalytic reaction. The gaseous products were sampled by a six-way valve and analyzed by an online gas chromatograph with a thermal conductivity detector (Shimadzu, GC-8A, Shincarbon ST, Ar carrier). The CO selectivity, S_{CO} (%), can be calculated as follows (eq. 1).[9] where the production rate of CO, H_2 and O_2 are referred to as R_{CO}, R_{H2} and R_{O2}, respectively. The ratio of the consumed electron and hole, e^-/ h^+, can be calculated as follows (eq. 2).[9]

$$S_{CO}\ (\%) = R_{CO} / (R_{CO} + R_{H2}) \times 100 \qquad (1)$$

$$e^{-} / h^{+} = (R_{CO} + R_{H2}) / 2\, R_{O2} \qquad (2)$$

Results and discussion

Structure and properties of the alkaline earth metal oxide modified $CaTiO_3$ photocatalyst

$CaTiO_3$ photocatalyst was prepared by solid state reaction method. Figure 1 shows XRD patterns of the $CaTiO_3$ (CTO) sample and some $CaTiO_3$ samples modified with 3 mol% of alkaline earth oxide (AO(3)/CTO) calcined at various temperatures. For the pristine CTO sample, all diffraction lines were assignable to a single phase of $CaTiO_3$ orthorhombic perovskite. The MgO(3)/CTO_1023 and CaO(3)/CTO_1023 samples that were prepared by calcination at 1023 K showed diffraction lines assigned to the rock salt structures of MgO and CaO at 43 and 38 degrees, respectively, except for the diffractions from $CaTiO_3$. The SrO(3)/CTO_773 and BaO(3)/CTO_773 samples exhibited diffraction lines assigned to $SrCO_3$ and $BaCO_3$ at 43 and 38 degrees, respectively. The lines in the patterns of SrO(3)/CTO_1023 and BaO(3)/CTO_1023 samples at 31 and 30 degrees were assignable to the corresponding titanate phases of $SrTiO_3$ and $BaTi_4O_9$, respectively. The peak positions for $CaTiO_3$ perovskite were not shifted before and after the modification with alkaline earth metal oxide. These suggest that alkaline earth metal oxide species, carbonate species, and additional titanate phases would be formed on the CTO surface.

Figure 2 shows diffuse reflectance UV-visible spectra of the AO(3)/CTO(A=Mg, Ca, Sr, and Ba) samples calcined at 1023 K. The $CaTiO_3$ moiety showed a large band at the UV range. From the clear threshold, each band gap was calculated to be 3.55–3.56 eV, which were similar to each other. The absorption that seemed to be a defect at 400–600 nm disappeared when AO was placed on it, and slightly changed below 400 nm. These facts suggest that the modification with the alkaline earth metal did not so much influence the band structure of $CaTiO_3$, but changed the properties of the surface defects.

SEM images of the samples were shown in Figure 3 and 4. The CTO particles consisted of irregular round-shape particles with smooth surface, the size of which were ca. 500–1000 nm, although they were connected to each other to some extent. Although the deposited alkaline earth metal species were not so clearly observed, small MaO species can be found on the smooth CTO particles (Fig. 4). With increasing loading amount of Mg species, they became clear on the images.

The amount of alkaline earth metal species on the catalyst decreased after Ag loading. The amount of alkaline earth metal species on the catalyst estimated by XRF was very small in comparison with initially loaded amount. Figure 5 and 6 shows XRD patterns of the Ag loaded alkaline earth metal oxide modified CTO samples. All diffraction lines were assigned to $CaTiO_3$ and metallic Ag and no diffractions derived from the alkaline earth metal oxide species were observed. Figure 7 and 8 shows diffuse reflectance UV-visible spectra of the Ag/CTO, Ag/AO(3)/CTO (A=Mg, Ca, Sr, and Ba), Ag/MgO(x)/CTO samples. By modification of alkaline earth metal species, the absorption at 350-800 nm derived from localized surface plasmon resonance of Ag was slightly increased compared to Ag / CTO. On the other hand, Ag/MgO(x)/CTO showed a similar absorption spectrum regardless of the amount of Mg. Figure 9 and 10 shows SEM images of the Ag/CTO, Ag/AO(3)/CTO (A=Mg, Ca, Sr, and Ba), Ag/MgO(x)/CTO samples. After the reaction, MgO particles mostly decreased and Ag nanoparticles seem to observed instead. on the Ag/MgO(x)/CTO catalyst as seen on MgO(x)/CTO, but only Ag nanoparticles were dispersed on the CTO surface.

Photocatalytic performances

Figure 11 shows the representative result of the photocatalytic CO_2 reduction test as time course of the production rates of CO, H_2, and O_2. No other gas phase products were detected. Initial rate of each products was 12.0, 1.1, and 0.63 μmol h^{-1}, respectively. Formation rate of CO and H_2 decreased, while that of O_2 increased over 4 hours after photoirradiation. And then each formation rate became stable. The formation rates of CO, H_2, and O_2 reached 7.3, 3.4, 0.15 μmol h^{-1}, respectively. The calculated selectivity toward CO in reductive products was 98%. At 8 h after the start of the irradiation, the ratio of consumed electrons to consumed holes (e^-/h^+), calculated from the production rate of CO, H_2, and O_2 according to the Eq. 1, was almost unity (1.1). This implies that photocatalytic reduction of CO_2 by H_2O proceeds stoichiometrically. These results show that CO_2 reduction by water took place as a major reaction and water splitting competitively proceeded as a very minor reaction, where the selectivity for CO formation between the two reductive reactions, CO_2 and proton reductions, was calculated to be 98% over the Ag/MgO(5)/CTO_1023 photocatalyst.

Table 1 shows the effect of cocatalysts and calcination temperature on the photocatalytic CO_2 reduction rate over the Ag/AO(x)/CTO samples (A=Mg, Ca, Sr, and Ba). Without the Ag cocatalyst, only H_2 and O_2 were generated on the bare CTO and Mg(5)/CTO photocatalysts, and CO as CO_2 reduction product was not obtained (entries 1 and 2). In contrast, all Ag loaded photocatalysts mainly produced CO and O_2 with a tiny amount of H_2. Each sample with Ag cocatalyst showed very high CO selectivity (>96%) (entries 3–13). These facts indicate that Ag cocatalyst is essential for the CO production on these CTO photocatalysts.

Figure 12 depicts the formation rates of the products and the CO selectivity over the Ag/CTO and Ag/AO(3)/CTO samples. Since the SrO/CTO_1023 and BaO/CTO_1023 samples contained the $SrTiO_3$ and $BaTi_4O_9$ phases, the samples obtained by calcination at 773 K are also shown here. The Ag/AO/CTO samples showed higher photocatalytic activity than the Ag/CTO sample except for the Ag/BaO/CTO_773 sample. The Ag/MgO/CTO and Ag/CaO/CTO samples showed about 2 times higher CO formation rate than the Ag/CTO sample.

Ag/SrO/CTO_773 showed higher activity than Ag/SrO/CTO_1023. Figure 13 shows Sr K-edge X-ray absorption near-edge structure (XANES) spectra of these Ag/SrO(3)/CTO samples with the $SrCO_3$, and $SrTiO_3$ samples as references. XANES spectrum of Sr species on the Ag/SrO(3)/CTO_773 sample were similar to $SrCO_3$. The XANES of the Ag/SrO(3)/CTO_1023 sample was almost the same as that of $SrTiO_3$, confirming that the Sr species would react with the $CaTiO_3$ surface to form $SrTiO_3$ structure, which is consistent with that shown in the XRD pattern (Fig. 1d). Ag/$SrTiO_3$ showed much lower activity than Ag/CTO for photocatalytic CO_2 reduction(Fig. 14), The photocatalytic activity of Ag/SrO(3)/CTO_1023 was slightly higher than that of Ag/CTO. Low-temperature EPR measurement of P-25, a mixed-phase TiO_2, showed that the trapped electrons generated in the rutile crystal were transferred to the anatase crystal.[24] The STO phase formed on the CTO is expected to help charge separation in the Ag/SrO(3)/CTO_1023 photocatalyst, which would contribute higher photocatalytic activity of Ag/SrO(3)/CTO_1023 than Ag/CTO. Ag/SrO(3)/BTO_773 showed lower photocatalytic activity than Ag/CTO. The basic strength as a solid-base material decreases in the order as BaO>SrO>CaO>MgO.[25] On the other hand, the number of basic sites per unit weight increases in the order as BaO<SrO<CaO<MgO.[25] BaO adsorbs CO_2 most strongly among the alkali metal oxides, that is, $BaCO_3$ is most stable among alkaline earth metal carbonates. It would not contribute the improvement for CO formation. Ag/BaO(3)/CTO showed higher activity than Ag/CTO. Figure 15 shows time courses of the production rates in the photocatalytic reduction of CO_2 with water over the Ag(4.3)/$BaTi_4O_9$ sample. Ag/$BaTi_4O_9$ showed higher activity than Ag/CTO. The $BaTi_4O_9$ phase formed on the CTO would contribute higher photocatalytic activity of Ag/BaO(3)/CTO_1023 than Ag/CTO.

Figure 16 shows the formation rate of the products over the Ag/MgO(*x*)/CTO samples with different Mg contents. The volcano-type curve indicates that Mg in catalysts containing about 5 mol% Mg is most effectively enhanced the photocatalytic activity, where the Ag/MgO(5)/CTO sample exhibited the highest CO formation rate of 7 μmol h^{-1} and 2.7 times higher than the Ag/CTO sample. This indicating that the moderate amount of the MgO species on the CTO surface much enhanced the photocatalytic CO_2 reduction to produce CO. All these samples showed very high CO selectivity >97%, suggesting that the addition of MgO species does not vary the selective CO formation promoted by the Ag cocatalyst. Figure S5 shows the UV-Vis spectra of the Ag/MgO(x)/CTO samples, which were recorded after the reaction tests. The absorption bands due to the local surface plasmon resonance (LSPR) of Ag nanoparticles are clearly shown in the range of 350–800 nm in wavelength. Almost no differences were observed among Ag/CTO and Ag/MgO(x)/CTO. This suggests that there is no difference in Ag nanoparticles size to give LSPR. These results indicated that the change in the activity was not mainly a result of the change in the states of the Ag cocatalyst. This proposed that the MgO species would contribute to other steps such as CO_2 adsorption as a solid base.

Figure 17 shows the results of the photocatalytic reaction tests with the Ag/CTO sample, the Ag/MgO(5)/CTO sample, and a physical mixture of the Ag/CTO sample and 5 mol% of commercially obtained MgO (Nacalai Tesque, 99.0%). As mentioned above, Ag/MgO(5)/CTO sample showed twice higher activity than that of Ag/CTO. In this case, the Ag/CTO sample in the presence of dissolved MgO showed almost the same activity as the Ag/CTO sample. Physical mixed MgO did not affect the photocatalytic activity. For the sample (c), the real amount of Mg species in the sample after reaction was 0.23 mol%. Most Mg species in the physical mixture dissolved into the solution during the reaction. Dissolved Mg species also did not affect the improvement of photocatalytic activity. This indicates that the surface modification by loading the MgO species before the photodeposition of the Ag cocatalyst resulted in the highly active Ag/MgO/CTO sample, implying that an interaction between the MgO species deposited on CTO in advance and the Ag nanoparticles photodeposited afterward would provide some contribution to the high activity.

Structure of silver and alkaline earth metal species

Figure 18 shows TEM images of the CTO, MgO(5)/CTO, MgO(15)/CTO, Ag/CTO, Ag/MgO(5)/CTO, and Ag/MgO(15)/CTO samples. The bare CTO sample consisted of crystals with smooth and rather flat surface. In the MgO(5)/CTO and MgO(15)/CTO sample, MgO species existed as an irregular-shape particles. In the Ag/CTO sample, the spherical Ag nanoparticles of 10–60 nm were observed on the CTO surface. Also in the Ag/MgO(15)/CTO sample, similar Ag particles were found. In contrast, it is notable that the TEM image of the Ag/MgO(5)/CTO sample shows unique aggregation forms consisting of many small dark particles and holes, which would originate from the characteristic structure of the Mg species in the MgO(5)/CTO samples. Since the Ag/MgO(5)/CTO sample contained 4.2 mol% of Ag and 0.067 mol% of Mg species (Table 1), it can be proposed that the Ag nanoparticles were decorated by small amount of the residual Mg species so as to form the unique aggregations. Combination of STEM image with EDX mappings and line analysis for this sample shown in Figure 19 clarified that the unique aggregates consisted of Ag (major) and Mg (minor). FT-IR revealed that the Mg species exist as $MgCO_3$ like species (Figure 20). It is proposed that the Ag nanoparticles strongly interacted with the $MgCO_3$ moieties would have the unique property, or rather, the aggregates, the Ag nanoparticles attached with the $MgCO_3$ moieties, would play dual roles such as adsorption by the $MgCO_3$ moieties and reduction of CO_2 to CO by the Ag nanoparticles.

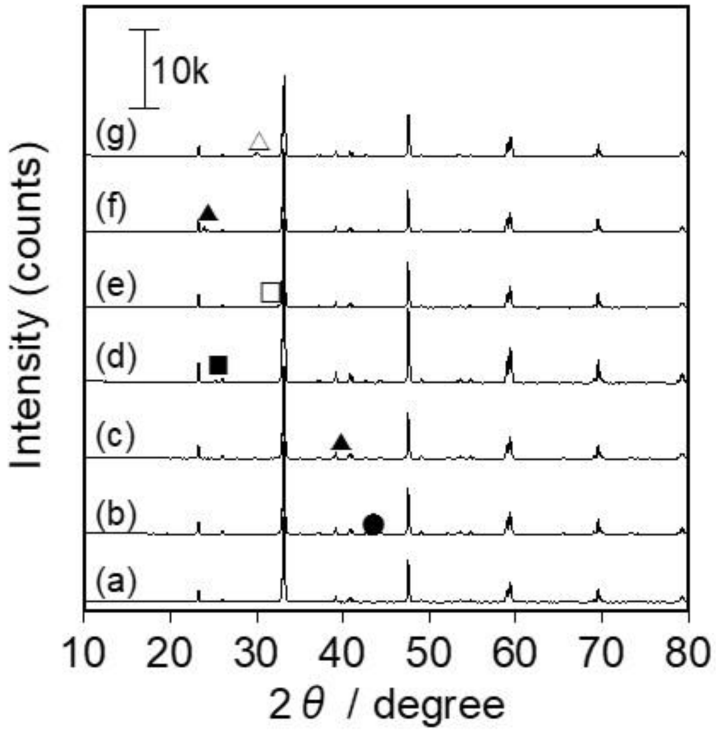

Figure 1. XRD patterns of the prepared samples, (a) bare CTO, (b) MgO(3)/CTO_1023K, (c) CaO(3)/CTO_1023K, (d) SrO(3)/CTO_773K, (e) SrO(3)/CTO_1023K, (f) BaO(3)/CTO_773K, and (g) BaO(3)/CTO_1023K. Symbols are indicated for the diffraction lines from MgO (closed circle), CaO (closed triangle), $SrCO_3$ (closed square), $SrTiO_3$ (open square), $BaCO_3$ (closed diamond), and $BaTi_4O_9$ (open diamond).

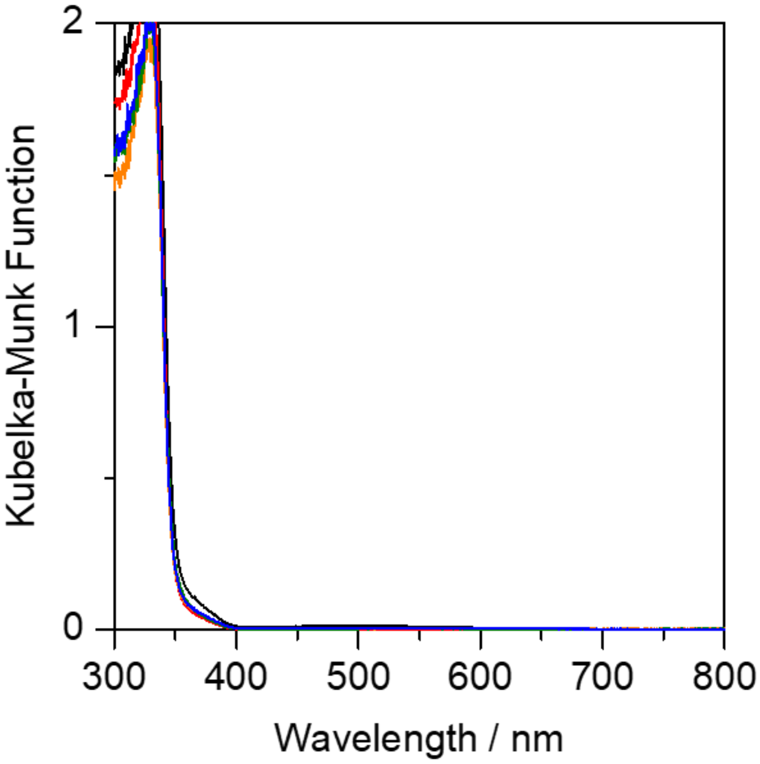

Figure 2. Diffuse reflectance UV-visible spectra of Ag(4.2)/AO(3)/CTO_1023K (A=Mg, Ca, Sr, and Ba) photocatalysts (a) bare CTO, (b) MgO(3)/CTO, (c) CaO(3)/CTO, (d) SrO(3)/CTO, and (e) BaO(3)/CTO.

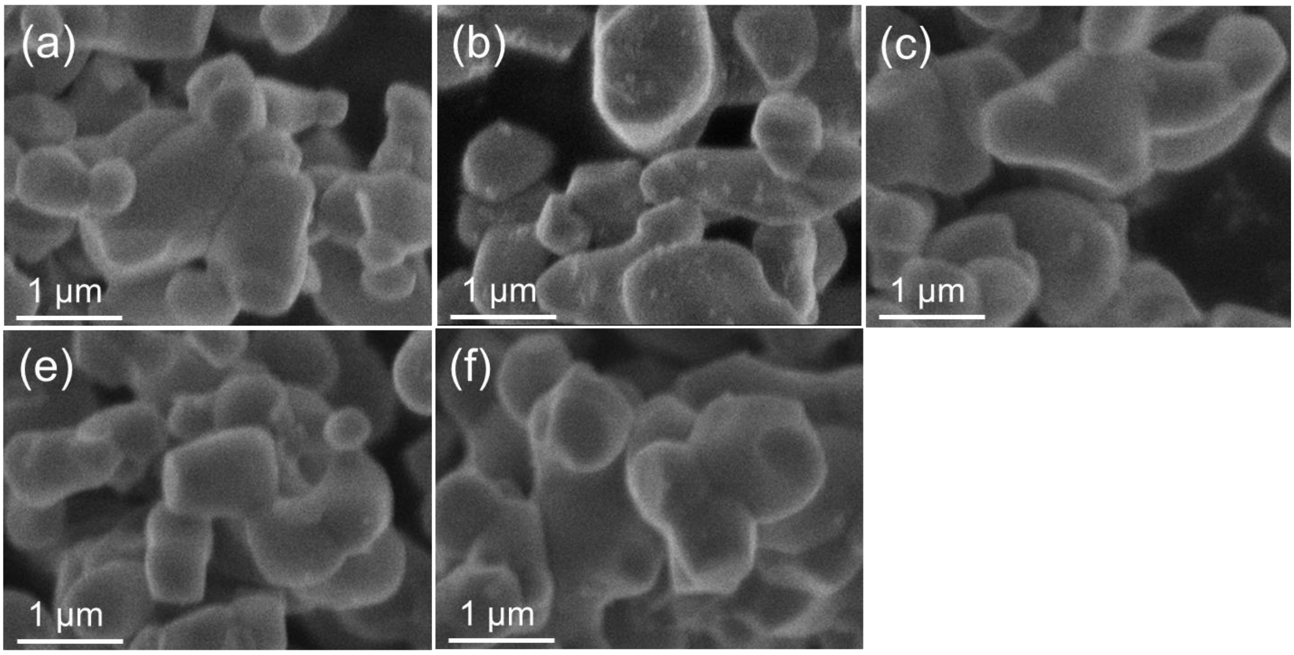

Figure 3. SEM images of (a) the bare CTO sample, (b) the MgO(3)/CTO sample, (c) the CaO(3)/CTO sample, (d) the SrO(3)/CTO sample, and (e) the BaO(3)/CTO sample. These AO loaded CTO samples were obtained by calcination at 1023 K.

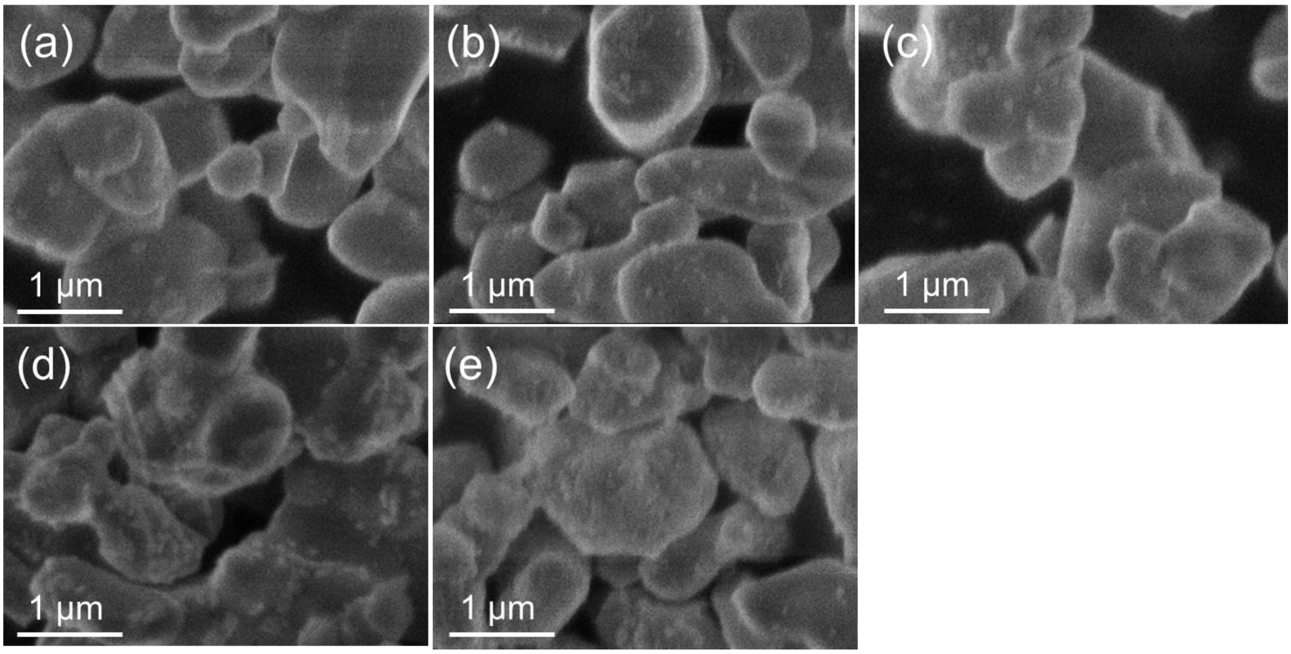

Figure 4. SEM images of (a) MgO(1)/CTO, (b) MgO(3)/CTO, (d) MgO(c)/CTO, (d) MgO(10)/CTO and (e) MgO(15)/CTO. These MgO loaded CTO samples were obtained by calcination at 1023 K.

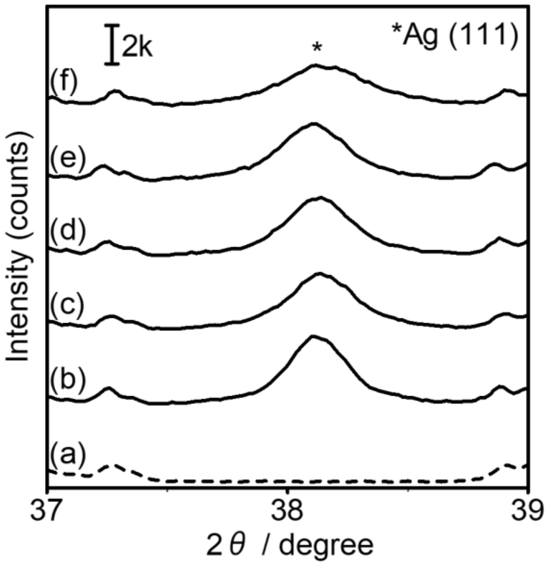

Figure 5. XRD patterns of the samples used in the photocatalytic reaction test for 8 h, (a) pure CTO, (b) Ag/CTO, (c)Ag/MgO(3)/CTO, (d) Ag/CaO(3)/CTO, (e)Ag/SrO(3)/CTO, (f)Ag/BaO(3)/CTO.

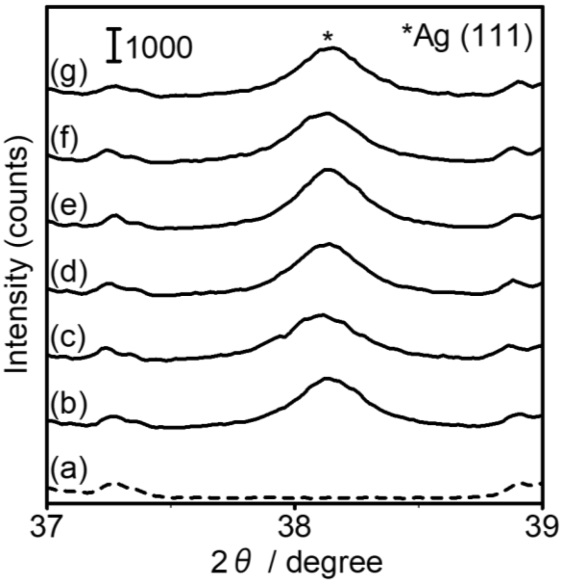

Figure 6. XRD patterns of the samples used in the photocatalytic reaction test for 8 h, (a) pure CTO, (b) Ag/CTO, (c) Ag/MgO(1)/CTO, (d) Ag/MgO(3)/CTO, (e)Ag/MgO(5)/CTO, (f)Ag/MgO(10)/CTO, and (g)Ag/MgO(15)/CTO.

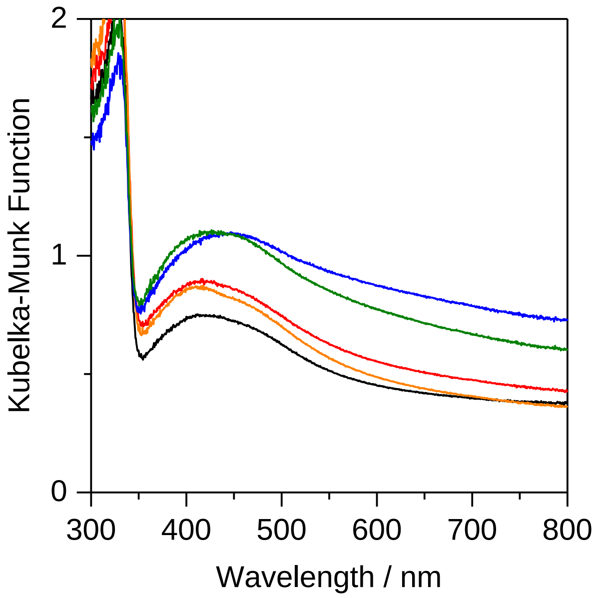

Figure 7. Diffuse reflectance UV-visible spectra of the samples used in the photocatalytic reaction test for 8 h, (a) Ag/CTO, (b)Ag/MgO(3)/CTO, (c) Ag/CaO(3)/CTO, (d)Ag/SrO(3)/CTO, (e) Ag/BaO(3)/CTO. Calcination temperature was 1023 K.

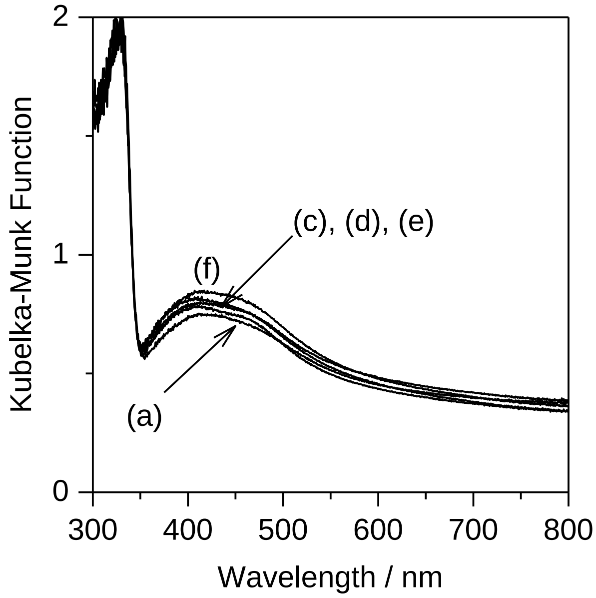

Figure 8. Diffuse reflectance UV-visible spectra of the samples used in the photocatalytic reaction test for 8 h, (a) Ag/CTO, (b)Ag/MgO(1)/CTO, (c) Ag/MgO(3)/CTO, (d)Ag/MgO(5)/CTO, (e)Ag/MgO(10)/CTO, and (e)Ag/MgO(15)/CTO. Calcination temperature was 1023 K.

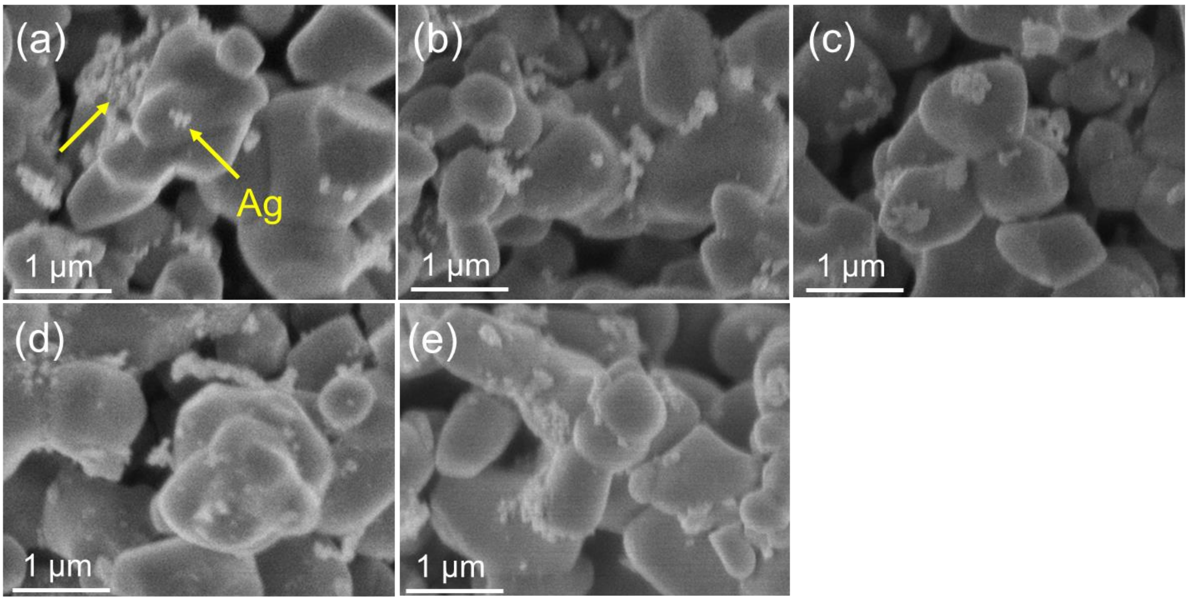

Figure 9. SEM images of the samples used in the photocatalytic reaction test for 8 h, (a) Ag/CTO, (b)Ag/MgO(3)/CTO, (c) Ag/CaO(3)/CTO, (d)Ag/SrO(3)/CTO, (e)Ag/BaO(3)/CTO. Calcination temperature was 1023 K.

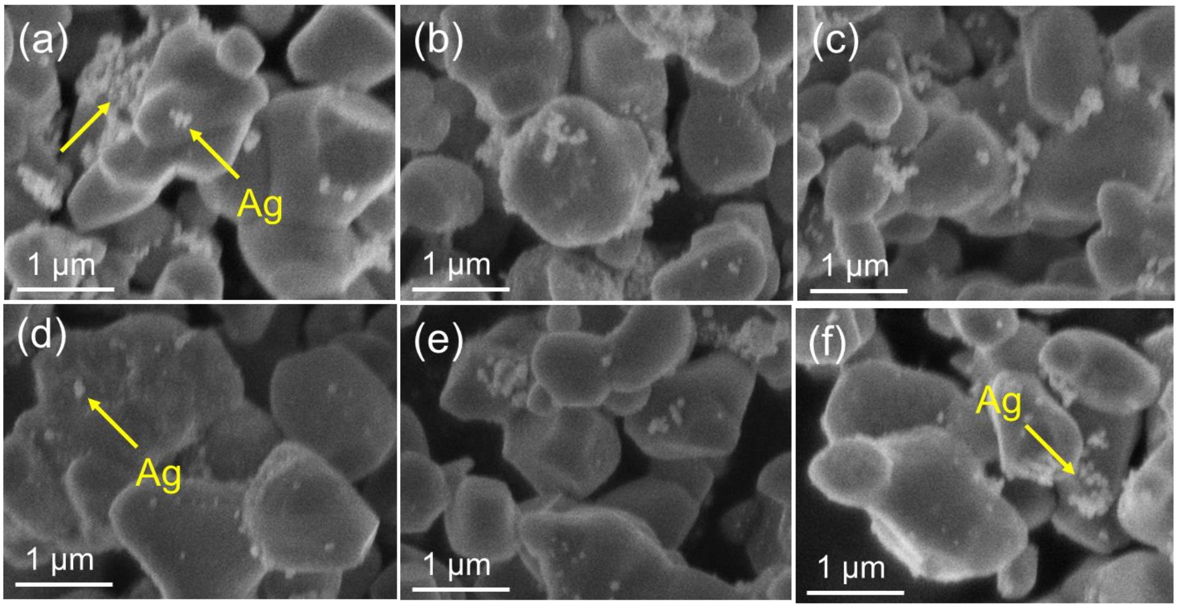

Figure 10. SEM images of the samples used in the photocatalytic reaction test for 8 h, (a) Ag/CTO, (b)Ag/MgO(1)/CTO, (c) Ag/MgO(3)/CTO, (d)Ag/MgO(5)/CTO, (e)Ag/MgO(10)/CTO, and (e)Ag/MgO(15)/CTO. Calcination temperature was 1023 K.

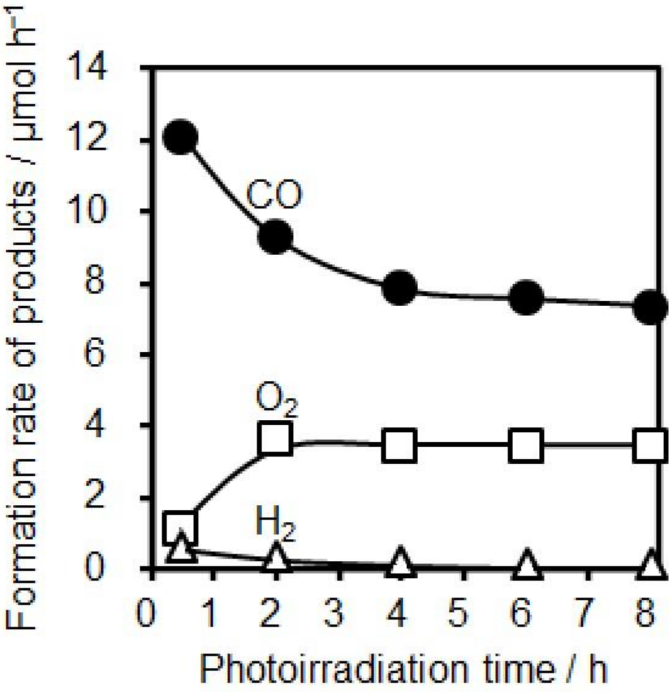

Figure 11. Time courses of the production rates of CO (closed circles), H_2 (closed triangles), and O_2 (open squares) in the photocatalytic reduction of CO_2 with water over the Ag(4.3)/MgO(5)/CTO sample. Amount of photocatalyst: 0.3 g, volume of reaction solution (H_2O): 350 mL, additive: 0.5 M $NaHCO_3$, CO_2 flow rate: 30 mL min^{-1}, and light source: 100 W high pressure Hg lamp with a quarts jacket. The values in parentheses represent the loading amount (mol%) of each species.

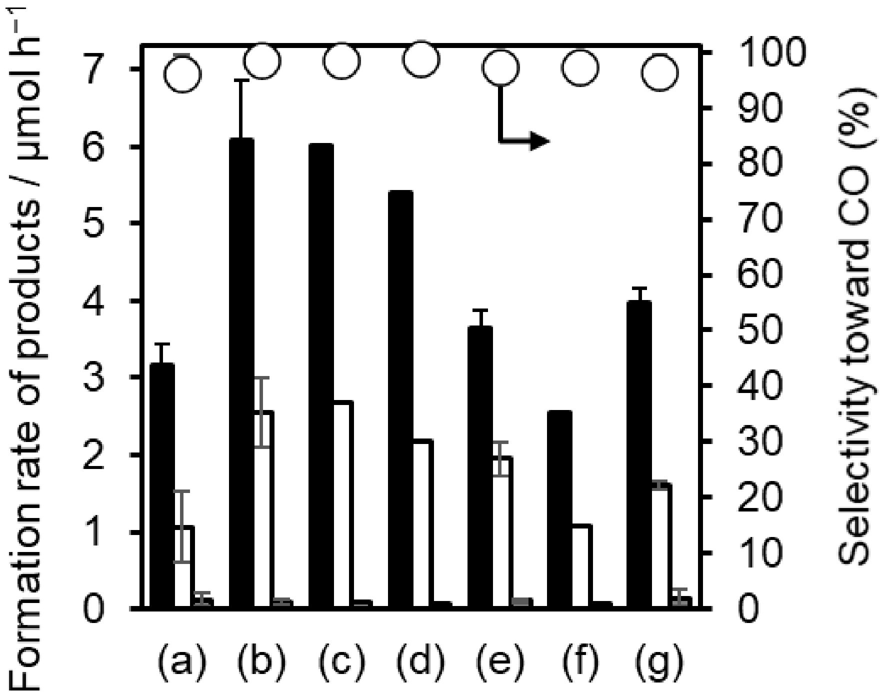

Figure 12. Formation rates of CO(black), O_2(white), and H_2(gray) and CO selectivity (closed circles) in the photocatalytic CO_2 reduction tests with various photocatalyst samples, (a) the Ag/CTO sample, (b) the Ag/MgO(3)/CTO_1023 sample, (c) the Ag/CaO(3)/CTO_1023 sample, (d) the Ag/SrO(3)/CTO_773 sample, (e) the Ag/SrO(3)/CTO_1023 sample, (f) the Ag/BaO(3)/CTO_773 sample, and (g) the Ag/BaO(3)/CTO_1023 sample. The values shown here were recorded after 8 h from the start of the photoirradiation. Amount of photocatalyst: 0.3 g, volume of reaction solution (H_2O): 350 mL, additive: 0.5 M $NaHCO_3$, CO_2 flow rate: 30 mL min^{-1}, and light source: 100 W high pressure Hg lamp with a quarts jacket.

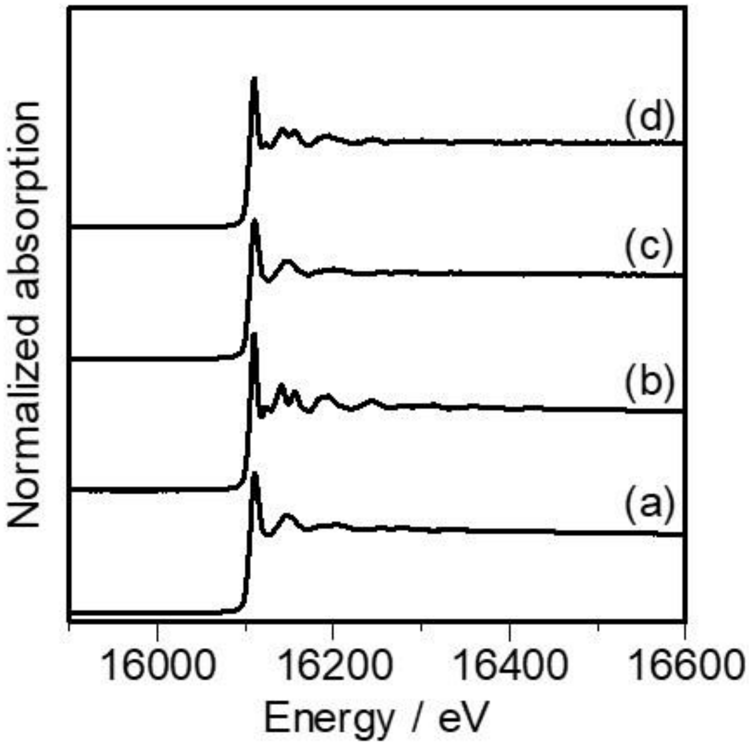

Figure 13. The Sr K-edge XANES for the samples, (a) $SrCO_3$, (b) $SrTiO_3$, (c) Ag/SrO(3)/CTO_773K, and (d) Ag/SrO(3)/CTO_1023 K. The photocatalyst samples were recovered after the photocatalytic reaction tests.

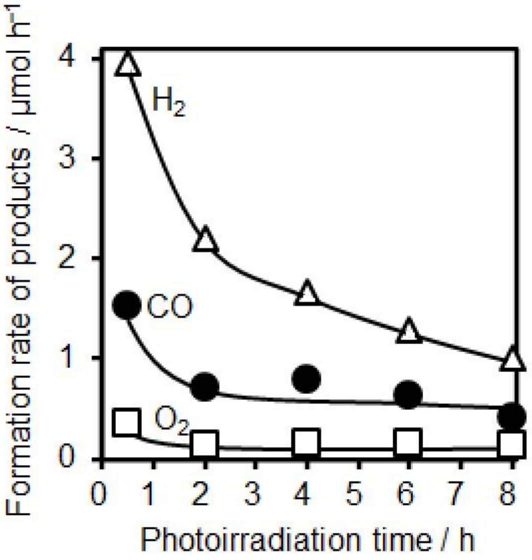

Figure 14. Time courses of the production rates of CO (circle), H_2 (triangle), and O_2 (square) in the photocatalytic reduction of CO_2 with water over the Ag(4.3)/$SrTiO_3$ sample.

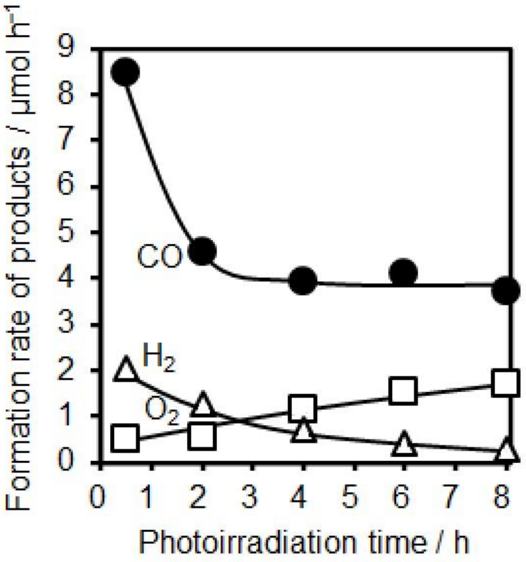

Figure 15. Time courses of the production rates of CO (circle), H_2 (triangle), and O_2 (square) in the photocatalytic reduction of CO_2 with water over the Ag(4.3)/$BaTi_4O_9$ sample.

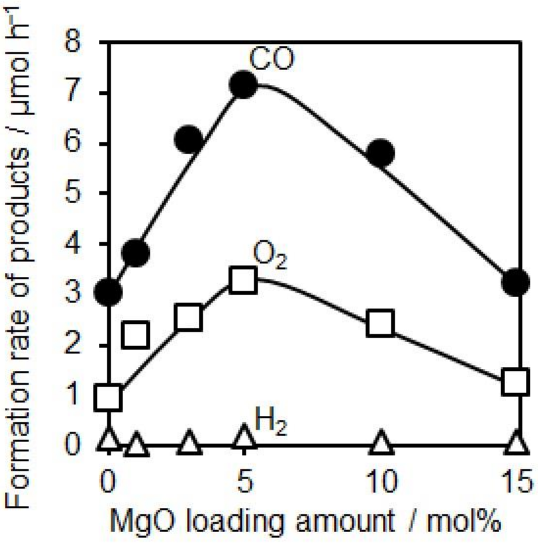

Figure 16. Formation rates of CO(black), O_2(white), and H_2(gray) and CO selectivity (closed circles) in the photocatalytic CO_2 reduction tests with the Ag/Mg(*x*)/CTO samples with various Mg loading. The calcination temperature in the step of MgO modification was 1023. The values shown here were recorded after 8 h from the start of the photoirradiation. Amount of photocatalyst: 0.3 g, volume of reaction solution (H_2O): 350 mL, additive: 0.5 M $NaHCO_3$, CO_2 flow rate: 30 mL min^{-1}, and light source: 100 W high pressure Hg lamp with a quarts jacket.

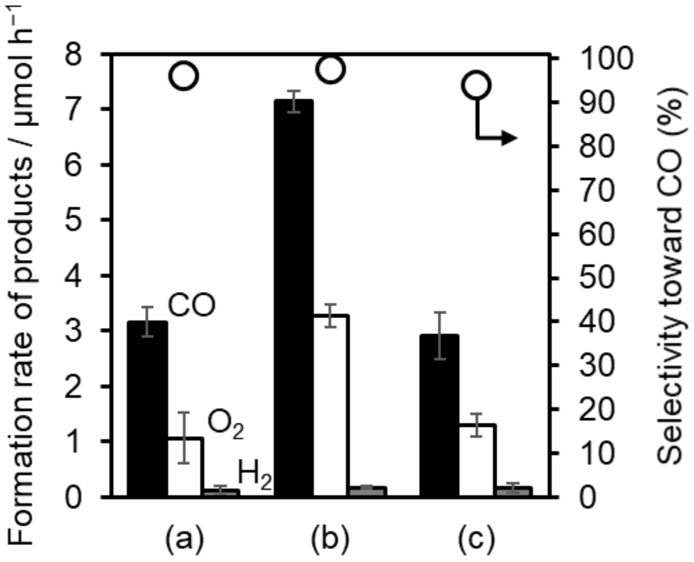

Figure 17. Formation rates of CO(black), O_2(white), and H_2(gray) and CO selectivity (closed circles) in the photocatalytic CO_2 reduction tests with (a) the Ag(4.3)/CTO sample, (b) the Ag(4.3)/MgO(5)/CTO sample, and (c) a physical mixture of the Ag(4.3)/CTO sample and 5 mol% of MgO. The values recorded after 8 h from the start of the photoirradiation were shown here. Amount of photocatalyst: 0.3 g, volume of reaction solution (H_2O): 350 mL, additive: 0.5 M $NaHCO_3$, CO_2 flow rate: 30 mL min^{-1}, and light source: 100 W high pressure Hg lamp with a quarts jacket. The error bars were calculated from three repeated measurements.

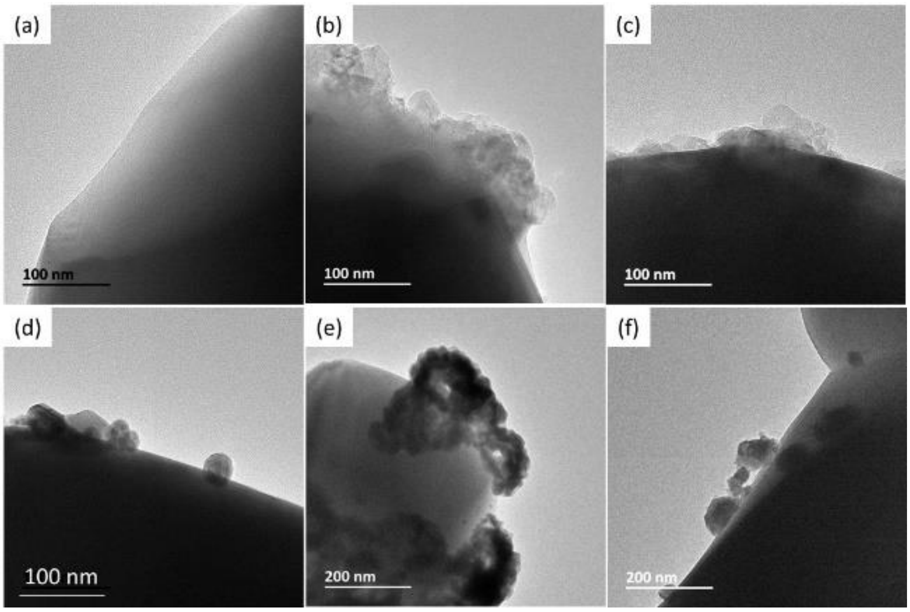

Figure 18. TEM images of the prepared samples, (a) bare CTO, (b) MgO(5)/CTO, (c) MgO(15)/CTO, (d) Ag/CTO (e) Ag/MgO(5)/CTO, and (f) Ag/MgO(15)/CTO after reaction.

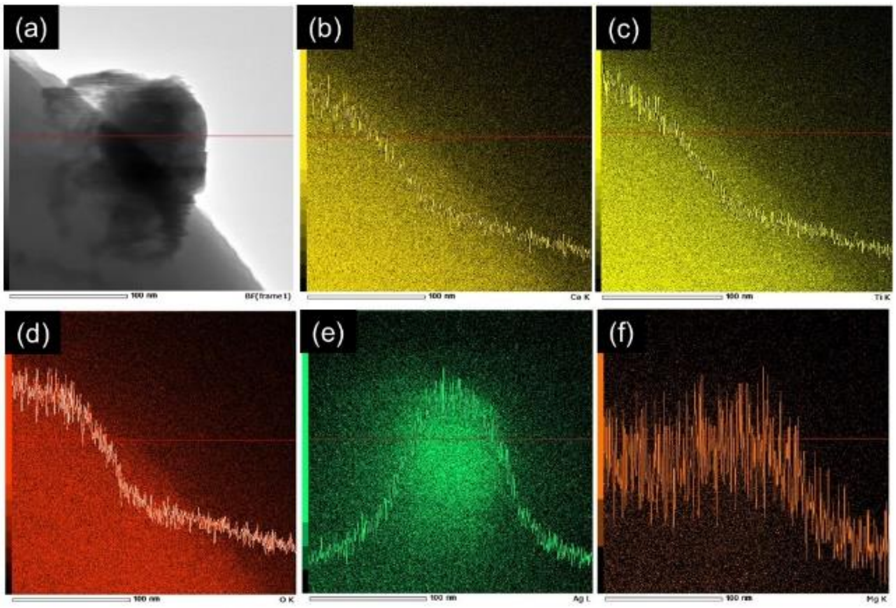

Figure 19. TEM images of the prepared samples, (a) bare CTO, (b) MgO(5)/CTO, (c) MgO(15)/CTO, (d) Ag/CTO (e) Ag/MgO(5)/CTO, and (f) Ag/MgO(15)/CTO after reaction.

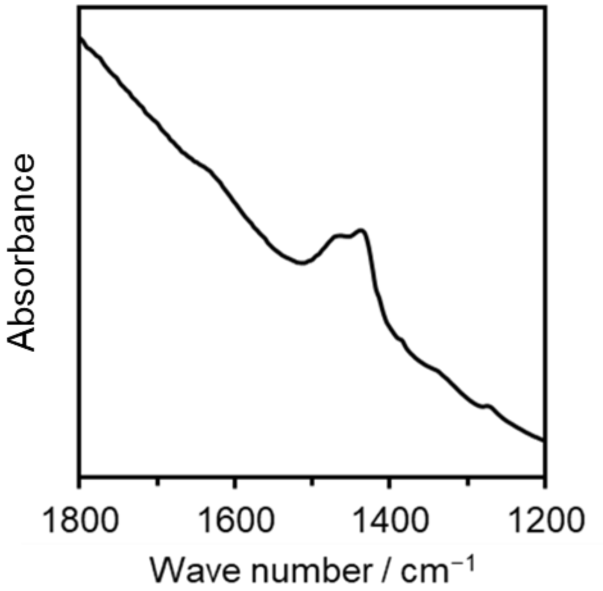

Figure 20. FT-IR spectrum of the MgO(5)/CTO sample.

Conclusions

In summary, the alkaline earth metal oxide and Ag co-modified $CaTiO_3$ photocatalysts were prepared and applied to the photocatalytic CO_2 reduction with water. Modification with alkaline earth metal oxides resulted in improvement of CO_2 conversion. Especially, MgO and Ag co-modified samples showed the highest CO formation rate (7 µmol h^{-1}) and the highest selectivity toward CO (S_{CO} = 98%). The activity was enhanced by 2 times compared with Ag loaded $CaTiO_3$ without MgO. By combination of STEM image with EDX mappings and line analysis, we found that Ag and Mg species formed an unique core–shell like structure on $CaTiO_3$ surface. This approach can also be applied to other photocatalysts for CO_2 reduction.formation of unique coreshell like structure.

Table 1. Results of photocatalytic reaction test for CO_2 reduction with water over the Ag/AO(*x*)/CTO_*y*K samples, (A=Mg, Ca, Sr, and Ba).

Entry	Cocatalyst[a]	loading (%)[b]	y / K[c]	Formation rate / μmol h^{-1}			S_{CO} (%)
				CO	O_2	H_2	
1	none	0	–	n.d.	0.26	0.027	0
2	Mg(5)	2.7	1023	n.d.	0.18	0.13	0
3	Ag	0	–	3.2	0.54	0.0082	98
	Ag-Mg (1)		1023	3.8	2.2	0.046	99
4	Ag-Mg (3)	0.28	1023	6.6	2.9	0.011	98
5	Ag-Mg (5)	0.067	1023	7.0	3.1	0.20	97
6	Ag-Mg (10)	1.1	1023	5.8	2.4	0.063	99
7	Ag-Mg (15)	0.24	1023	3.2	1.2	0.072	98
8	Ag-Ca(3)	–	1023	6.0	2.7	0.080	99
9	Ag-Sr(3)	1.8	773	5.4	2.2	0.070	99
10	Ag-Sr(3)	0.63	1023	3.6	1.9	0.10	97
11	Ag-Ba(3)	0.036	773	2.5	1.1	0.070	97
12	Ag-Ba(3)	0.34	1023	4.0	1.6	0.14	96

[a] value in parentheses is the loaded amount of the alkaline earth metal (*x*, atom%).…[b] loading amount of AO (atom%) remaining after the use for the reaction test, which was determined by XRF. [c] Calcination temperature to obtain the AO/CTO samples.

References

[1] D. G. Nocera, *Acc. Chem. Res.* **2017**, *50*, 616–619.

[2] L. Liu, H. Zhao, J. M. Andino, Y. Li, **2012**, DOI 10.1021/cs300273q.

[3] F. Jiao, J. Li, X. Pan, J. Xiao, H. Li, H. Ma, M. Wei, Y. Pan, Z. Zhou, M. Li, et al., *Science (80-.).* **2016**, *351*, 1065–1068.

[4] J. Schneider, H. Jia, J. T. Muckerman, E. Fujita, *Chem. Soc. Rev.* **2012**, *41*, 2036–2051.

[5] K. Iizuka, T. Wato, Y. Miseki, K. Saito, A. Kudo, *J. Am. Chem. Soc.* **2011**, *133*, 20863–20868.

[6] H. Nakanishi, K. Iizuka, T. Takayama, A. Iwase, A. Kudo, *ChemSusChem* **2017**, *10*, 112–118.

[7] T. Takayama, **2015**, *3*, DOI 10.1246/bcsj.20140350.

[8] T. Takayama, H. Nakanishi, M. Matsui, A. Iwase, A. Kudo, *"Journal Photochem. Photobiol. A Chem.* **2018**, *358*, 416–421.

[9] Z. Huang, K. Teramura, S. Hosokawa, T. Tanaka, *Appl. Catal. B Environ.* **2016**, *199*, 272–281.

[10] K. Teramura, Z. Wang, S. Hosokawa, Y. Sakata, T. Tanaka, *Chem. - A Eur. J.* **2014**, *20*, 9906–9909.

[11] R. Pang, K. Teramura, H. Asakura, S. Hosokawa, T. Tanaka, *Appl. Catal. B Environ.* **2017**, *218*, 770–778.

[12] Z. Wang, K. Teramura, S. Hosokawa, T. Tanaka, *Appl. Catal. B Environ.* **2015**, *163*, 241–247.

[13] A. Anzai, N. Fukuo, A. Yamamoto, H. Yoshida, *Catal. Commun.* **2017**, *100*, 134–138.

[14] X. Zhu, A. Anzai, A. Yamamoto, H. Yoshida, *Appl. Catal. B Environ.* **2019**, *243*, 47–56.

[15] X. Zhu, A. Yamamoto, S. Imai, A. Tanaka, H. Kominami, H. Yoshida, *Chem. Commun.* **2019**, *55*, 13514–13517.

[16] Y. Duan, D. C. Sorescu, *J. Chem. Phys.* **2010**, *133*, DOI 10.1063/1.3473043.

[17] K. Teramura, H. Tatsumi, Z. Wang, S. Hosokawa, T. Tanaka, *Bull. Chem. Soc. Jpn.* **2015**, *88*, 431–437.

[18] H. Tatsumi, K. Teramura, Z. Huang, Z. Wang, H. Asakura, S. Hosokawa, T. Tanaka, **2017**, DOI 10.1021/acs.langmuir.7b03191.

[19] S. Iguchi, Y. Hasegawa, K. Teramura, S. Kidera, S. Kikkawa, S. Hosokawa, H. Asakura, T. Tanaka, *Sustain. Energy Fuels* **2017**, *1*, 1740–1747.

[20] S. Xie, Y. Wang, Q. Zhang, W. Deng, Y. Wang, *ACS Catal.* **2014**, *4*, 3644–3653.

[21] U. Holzwarth, N. Gibson, *Nat. Nanotechnol.* **2011**, *6*, 534–534.

[22] J. Tauc, R. Grigorovici, A. Vancu, *Phys. Status Solidi* **1966**, *15*, 627–637.

[23] K. Teramura, K. Hori, Y. Terao, Z. Huang, S. Iguchi, Z. Wang, H. Asakura, S. Hosokawa, T. Tanaka, *J. Phys. Chem. C* **2017**, *121*, 8711–8721.

[24] D. C. Hurum, A. G. Agrios, K. A. Gray, T. Rajh, M. C. Thurnauer, *J. Phys. Chem. B* **2003**, *107*, 4545–4549.

[25] G. Zhang, H. Hattori, K. Tanabe, **1988**, *36*, 189–197.

Chapter 4

Photocatalytic reduction of carbon dioxide by water using calcium titanate with a different particle size

Abstract

The establishment of design guidelines for highly active photocatalysts for CO_2 photoreduction has great academic and industrial significance. Here, photocatalytic properties of $CaTiO_3$ with different specific surface areas, such as H_2 evolution, O_2 evolution, and CO_2 reduction with water, were compared. In the O_2 evolution reaction with $AgNO_3$ as sacrificial reagent, a sample with larger particle size showed higher formation rate. Whereas, in the H_2 evolution with methanol as a sacrificial reagent and CO_2 reduction with water, a sample with smaller particle size showed higher formation rate. We believe that this work could be beneficial to development of highly efficient photocatalysts for artificial photosynthesis. The effect of particle size on the CO_2 photoreduction activity of $CaTiO_3$ particles using water as an electron source was investigated using prepared commercial $CaTiO_3$ particles and large particles obtained by calcination.

Introduction

CO_2 conversion into fuels or chemical feedstock compounds could lead to reducing fossil fuel consumption and CO_2 emission.[1][2] Photocatalytic reduction of CO_2 is one of the most exciting photocatalytic reactions, as photon energy can be used to directly produce useful chemicals such as CO from CO_2.[3] Many semiconductor photocatalysts for photocatalytic reduction of CO_2 have widely been studied. We have developed Ag-loaded $CaTiO_3$ photocatalyst for the photocatalytic reduction of CO_2 with water. Ag-loaded $CaTiO_3$ photocatalyst can convert CO_2 into CO with excellent selectivity toward CO from CO_2 (94%) using water as an electron donor.[4] To develop the highly active $CaTiO_3$ photocatalysts for reduction of CO_2, the decisive factors determining the photocatalytic activity should be elucidated. Many reports have confirmed the significant effects of the particle size on the photocatalytic activity. Not limited to photocatalysts, catalysts in general, micronization increases the surface area of particles and increases the adsorption sites of reaction substrates. For example, when using a TiO_2 photocatalyst with a particle size of 12-150 nm, the smaller the particle size, the higher the activity when hydrogen is generated from water and alcohol. Adsorption of CO_2 on the catalyst surface is a demanding step in CO_2 photoreduction. The relationship between the particle size of semiconductor crystal and photocatalytic activity for reduction of CO_2 has not been clarified yet and only a few studies have dealt with this topic. Kočí et al. pure TiO_2 anatase particles with a crystallite diameters ranging from 4.5 to 29 nm tested in CO_2 photocatalytic reduction. Methane and methanol were the main reduction products. As the particle size decreased, higher yields of methanol and methane were obtained. The optimum particle size corresponding to the highest yields of both products was 14 nm.

Experimental

Catalyst preparation

Three kinds of $CaTiO_3$ samples were used in this study. CT–01 and CT–03 were commercially available (CT–01 (Sakai Chemical Industry Co., Ltd; 99.9%). CT–03(Sakai Chemical

Industry Co., Ltd; 99.9%)). CT–01_1423K was obtained by calcination of CT-01 at 1423 K for 2 h in air in an electric muffle furnace (Nitto Kagaku, NHK1-170). The loading of the Ag cocatalysts was performed by the impregnation method. 0.5 g of the $CaTiO_3$ sample was dispersed in 25 mL aqueous $AgNO_3$ solution (0.5 M) and stirred at 353 K in a water bath to dry up, followed by calcination at 723 K for 2h. $RhCl_3$ (Wako pure chemical; 99.9%) and $Cr(NO_3)_3$ (Wako pure chemical; 99.9%) mixed solution was used for loading $Rh_{0.7}Cr_{1.3}O_3$ cocatalyst,[9] They were calcined at 623 K for 2 h. The amount of the co-catalyst was 0.3 wt% as Rh in $Rh_{0.7}Cr_{1.3}O_3$.

Characterization

The crystal structure of the $CaTiO_3$ samples were determined by powder X-ray diffraction with a Lab X XRD-6000 (Shimazu). Morphologies of the samples were observed by scanning electron microscopy (SEM) with a JSM-890 (JEOL). The diffuse reflectance (DR) UV–visible spectrum of the prepared sample was recorded by a V-670 (JASCO) equipped with an integrating sphere. The band gap was estimated from the spectrum according to Tauc plot. The BET specific surface area was estimated from the amount of N_2 adsorption at 77 K measured using a Quantachrome Monosorb MS-21.

Photocatalytic activity test

The photocatalytic reduction of CO_2 reaction were carried out in a conventional inner irradiation photochemical reactor equipped with a 100 W high pressure Hg lamp through a quartz filtter equipped with a cooling water system. 0.3 g of the photocatalyst powder loaded with Ag-cocatalyst dispersed in 350 mL of aqueous $NaHCO_3$ solution in a continuous bubbling flow of gaseous CO_2 (99.999%). The suspention was purged with CO_2 for 1h to remove dissolved oxygen, followed by irradiation. CO_2 gas was bubbled into the water at a flow rate of 30 mL min^{-1}. Photocatalytic half reactions, the photoreduction of H^+ to H_2 in an aqueous methanol solution (10 vol %) and the photooxidation of H_2O to O_2 in an aqueous $AgNO_3$ solution (0.01 M), were also performed in the same manner. The evolved gas, that is, H_2, O_2, and CO, were analyzed by thermal conductivity detector (TCD) GC by using a GC-8A chromatograph (Shimadzu) equipped with an Shincarbon ST column (carrier gas: Ar).

Results and discussion

The properties of bare $CaTiO_3$ samples are summarized in Table 1. The measured BET specific surface area of the CT−01, CT-03, CT−01(1423), were 15.7, 7.7, 1.8 $m^2\ g^{-1}$, respectively. The surface area of the sample was high in the order of CT-01 > CT-03 > CT-01(1423). Figure 1 shows the XRD patterns of the samples. All diffraction lines can be assigned to the orthorhombic perovskite structure without any impurity phases. The order in the intensities of the diffraction peaks was CT-01 < CT-03 < CT-01(1423). The order in the full width at half maximum (FWHM) of the (1 2 1) peak was also CT-01 < CT-03 < CT-01(1423). Therefore the order in the crystallinity of the sample was CT-01 < CT-03 < CT-01(1423).

Table 1. The properties of bare $CaTiO_3$ samples

Catalyst	calcination	Surface area / $m^2\ g^{-1}$	Particle size / nm	Particle size SEM / nm	Band gap / eV
CT-01	uncalcined	15.7	95	100	3.43
CT-03	uncalcined	7.7	193	300	3.44
CT-01(1423)	1423 K	1.8	825		3.52

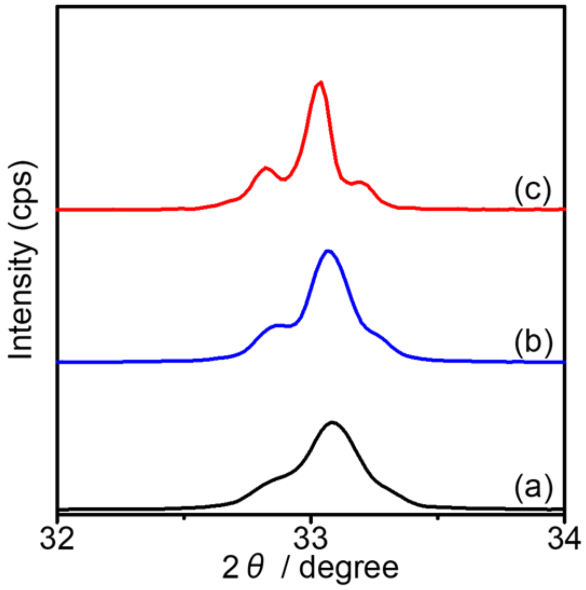

Figure 1. XRD patterns and FWHM and the intensity of the (101) plane of the samples. CT−01 (a), CT−03 (b), and CT−01(1423) (c).

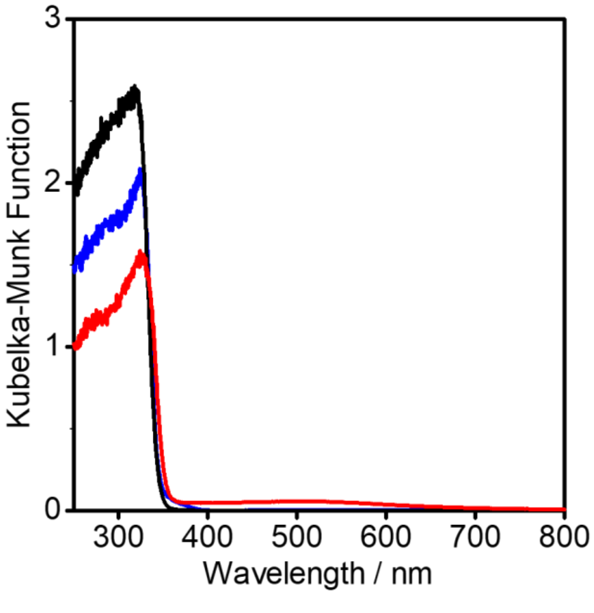

Figure 2. Diffuse reflectance UV–Vis spectra of the $CaTiO_3$ samples. CT−01 (black), CT−03 (blue), and CT−01(1423) (c).

Figure 3 shows the results of the photocatalytic reduction of CO_2 in aqueous $NaHCO_3$ solution over 0.5 wt% Ag-cocatalyst loaded CTO photocatalysts (CT-01, CT-03, CT-01(1423)). All samples produced CO and O_2 as major products with tiny amount of H_2 as a by-product. CO_2 and H_2O into CO and O_2 occurred according to

$$CO_2 + 2H^+ + 2e^- \rightleftarrows CO + H_2O \ (E^0_{CO2/CO} = -0.11 \text{ V}) \tag{1}$$

$$H_2O \rightleftarrows 1/2\ O_2 + 2H^+ + 2e^- \ (E^0_{O2/H2O} = 1.23 \text{ V}) \tag{2}$$

$$CO_2 \rightleftarrows CO + 1/2\ O_2 \ (\mathit{\Delta} G^0 = 2.68 \text{ eV}) \tag{3}$$

CT−01 with a surface area of 15.7 m^2 g^{-1}, which is the highest surface area among the samples, showed the highest CO formation rate (3.4 µmol h^{-1}) among tested samples. The photocatalytic activity decreased as the surface area decreased from 15.7 to 1.8 m^2 g^{-1}. CT-01(1423) showed much lower photocatalytic activity than CT-01 and CT-03. Selectivity toward CO was almost the same between CT-01 and CT-03, while CT-01(1423) showed lower selectivity toward CO (88%) than CT-01 and CT-03. The opposite trend was found between the photocatalytic activity for reduction of CO_2 and the crystallinity of the samples.

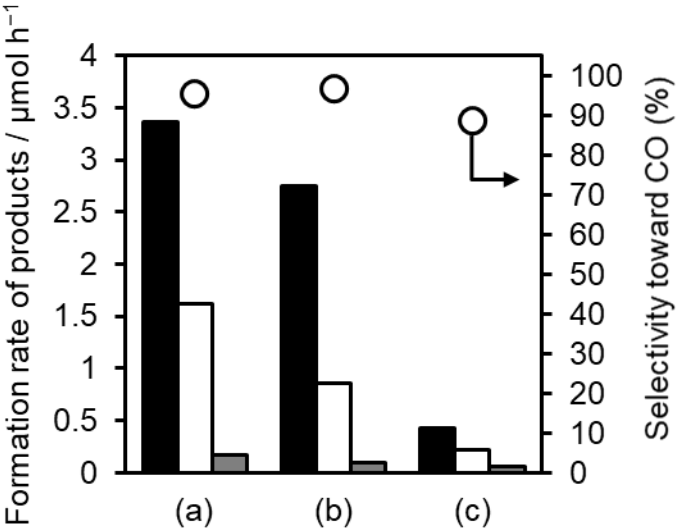

Figure 3. formation rate of CO (black bars), O_2 (white bars), and H_2 (gray bars), as well as selectivity toward CO evolution (open circles) for various photocatalysts: Ag(1)/CT−01 (a), Ag(1)/CT−03 (a), and Ag(1)/CT−01_1423 (c). specific surface area of the samples was 15.7, 7.7, and 1.8 m^2 g^{-1}, respectively. Amount of photocatalyst: 0.3 g, volume of reaction solution (H_2O): 350 mL, additive: 0.5 M $NaHCO_3$, CO_2 flow rate: 30 mL min^{-1}, and light source: 100 W high pressure Hg lamp with a quarts jacket.

To delve into the reactivity of the three CTO samples with different surface area, we carried out a separate activity test for water oxidation from aqueous silver nitrate solution, in which Ag^+ ions work as the electron scavenger. Figure 5 shows the time course of O_2 evolution over each CTO sample. CT-03 exhibits the highest activity with the fastest O_2 evolution rate followed by samples CT-01 and CT-01(1423). This observed trend of O_2 evolution activities of the CTO samples (CT-01(1423) < CT-01 < CT-03) is different from their tendency in the reduction of CO_2 (CT-01(1423) < CT-03 < CT-01). This means that the high photocatalytic activity of CT-01 is not due to the promotion of the O_2 evolution process.

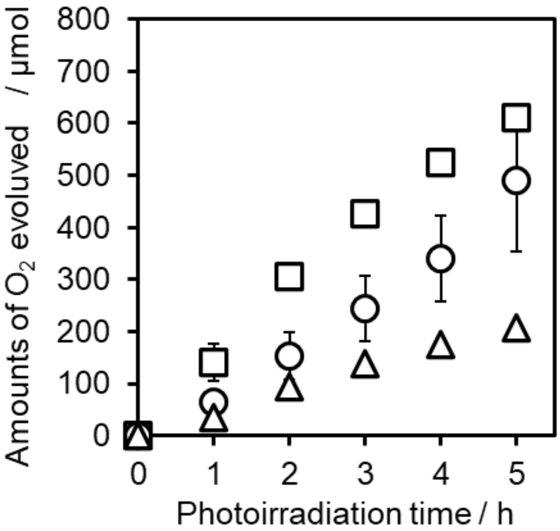

Figure 4. Photocatalytic oxygen evolution over CT−01 (open circle), CT−03 (open square), and CT−01(1423) (open triangle). Specific surface area of the samples was 15.7, 7.7, and 1.8 m^2 g^{-1}, respectively. Amount of photocatalyst: 0.3 g, volume of reaction solution (H_2O): 350 mL, Ar flow rate: 30 mL min^{-1}, and light source: 100 W high pressure Hg lamp with a quarts jacket.

Conclusions

In this study, photocatalytic properties of $CaTiO_3$ particles, such as photocatalytic reduction of CO_2 to CO with water in terms of $CaTiO_3$ particle size. Three $CaTiO_3$ samples with different specific surface areas were used. The specific surface areas were 15.7, 7.7, and 1.8 m^2 g^{-1}, respectively. Ag-cocatalyst was loaded on each samples, and the photocatalytic activity for reduction of CO_2 was evaluated. The samples with a large specific surface area tended to show high CO formation rate. to investigate the reason of the high photocatalytic activity of CT-01, photocatalytic oxygen evolution reaction was also carried out. The trend of O_2 evolution activities of the CTO samples is different from their tendency in the reduction of CO_2. This indicates that the high photocatalytic activity of CT-01 is not due to the promotion of the O_2 evolution process. The improvement of CO_2 adsorption could be one reason for improvement of CO formation from CO_2.

References

[1] H. M. Jhong, S. Ma, P. J. A. Kenis, *Curr. Opin. Chem. Eng.* **n.d.**, *2*, 191–199.

[2] M. Aresta, A. Dibenedetto, A. Angelini, **2014**, DOI 10.1021/cr4002758.

[3] S. N. Habisreutinger, L. Schmidt-mende, J. K. Stolarczyk, **2013**, 7372–7408.

[4] A. Anzai, N. Fukuo, A. Yamamoto, H. Yoshida, *Catal. Commun.* **2017**, *100*, 134–138.

[5] C. Colbeau-Justin, M. Kunst, D. Huguenin, *J. Mater. Sci.* **2003**, *38*, 2429–2437.

[6] F. Amano, E. Ishinaga, A. Yamakata, *J. Phys. Chem. C* **2013**, *117*, 22584–22590.

[7] S. P. Adhikari, A. Lachgar, *J. Phys. Conf. Ser.* **2016**, *758*, DOI 10.1088/1742-6596/758/1/012017.

[8] B. R. Müller, S. Majoni, R. Memming, D. Meissner, *J. Phys. Chem. B* **1997**, *101*, 2501–2507.

[9] K. Shimura, K. Maeda, H. Yoshida, *J. Phys. Chem. C* **2011**, *115*, 9041–9047.

Introduction of Part II

Hydrogen is an important chemical raw material in many chemical industrial processes such as ammonia synthesis, methanol synthesis, basic synthesis and other organic synthesis or hydroprocessing of oil. [1] In recent years, the importance of hydrogen as a clean energy for fuel cells has increased.[2] Unlike the hydrocarbon fuels used today, hydrogen produces only water during oxidation.

Currently, most of hydrogen is produced by steam reforming of methane (SRM) [3]. The process consists of multiple catalytic reactions and the entire chemical equation can be shown as Eq.1 [4].

$$CH_4 + 2\ H_2O \rightarrow 4\ H_2 + CO_2 \qquad \Delta G^{\ominus}_{298K} = 113.5\ \mathrm{kJ\ mol^{-1}} \qquad (1)$$

High yield is achieved at high reaction temperature (1123−1173 K) due to the highly endergonic property of the reaction requires high reaction temperature, even in the presence of practical catalysts [4]. To improve the energy efficiency, high pressure (30−40 bar) are also used.[5] In this way, normally, it does not proceed unless it is under severe conditions, but when a photocatalyst is used, the reaction could proceeds even at room temperature and normal pressure but the yield is low [6–11].

It was found that the reaction of Eq.1 proceeds photocatalytically near room temperature. We discovered platinum-loaded semiconductor photocatalysts, such as Pt/TiO_2 and $Pt/NaTaO_3$:La, can continuously promote photocatalytic steam reforming of methane (PSRM) around room temperature, and developed several kinds of metal loaded photocatalyst such as $Pt/CaTiO_3$ [12,13], Pt/Ga_2O_3 [14–16], and $Rh/K_2Ti_6O_{13}$ [17,18]. Among these studies, it is demonstrated that the photocatalytic activity can be improved by doping suitable amount of a certain metal cation to the semiconductor, e.g., La^{3+} to $NaTaO_3$ [19,20] and Mg^{2+} or Zn^{2+} to Ga_2O_3 [14,15]. Recently, it was found that fine and regularly shaped crystals of photocatalyst such as $NaTaO_3$ [21] and $Na_2Ti_6O_{13}$ [22] prepared by a flux method exhibits higher activity in PSRM than untailored particles prepared by a solid state reaction method. Table 1 summarizes the photocatalysts which showed the photocatalytic activity for PSRM.

Loading the cocatalyst on the photocatalyst surface is necessary for PSRM to proceed. The effect of cocatalyst on $K_2Ti_6O_{13}$ photocatalyst for PSRM was investigated.[18] Rh, Pt, Ru, Pd and Au was loaded as a cocatalysts. The cocatalysts (0.03 wt %) were loaded by an impregnation method and photodeposition method. When the cocatalysts were loaded by an impregnation method, Pt cocatalyst was the best. While Rh cocatalyst was the best when the cocatalysts were loaded by a photodeposition method. Ru, Pd and Au cocatalyst on $K_2Ti_6O_{13}$ didn't enhance the photocatalytic activity. The sample with Rh cocatalyst loaded by a photodeposition method showed the highest H_2 production rate (about 90 μmol h^{-1}). Rh and Pt cocatalyst were good candidate for PSRM, although the activity depended on the loading method. The reaction mechanism for PSRM over Pt/TiO_2 was proposed (Figure 1)[8].

This value was higher than the quantum yield of water splitting in this reaction condition employing a $NiO/NaTaO_3$:La photocatalyst [39], which is one of the best photocatalysts for water splitting. This showed that the present PSRM could produce hydrogen more efficiently than the water splitting systems. When the reaction was carried out using the $Pt/NaTaO_3$:La photocatalyst and the present reaction setup under the optimum reaction condition (CH_4: 10 %, H_2O: 1 %, light intensity at 254 ± 10 nm: 116 mW cm^{-2}), the hydrogen production rate was 4.5 μmol min^{-1} (6.6 mL h^{-1}) and the conversion of methane and water reached to 0.6 and 11 %, respectively. However, the efficiency of this system is still far from the practical use. The development of more active photocatalyst and also the improvement of photoreactor would be necessary.

PSRM reaction was performed over $NiO/NaTaO_3$:La. Even when methane coexisted, only H_2 and O_2 were obtained as products, and the PSRM reaction did not proceed.

Therefore, even if the PSRM reaction is carried out using a photocatalyst that promotes water decomposition with high efficiency, PSRM does not always proceed. Therefore, it is necessary to study the catalyst design guidelines specific to this reaction.

In the present study, we examined a flux method and La^{3+}-doping to improve the photocatalytic activity of Pt/$CaTiO_3$ photocatalyst. We synthesized several doped and non-doped $CaTiO_3$ photocatalysts by a flux method with various conditions and a conventional solid state reaction method, characterized them in several methods, and evaluated them in PSRM.

Outline of Part II

Part II focused on developing highly active $CaTiO_3$-based photocatalysts for photocatalytic steam reforming of methane (PSRM). In Chapter 5, the flux method was applied to prepare $CaTiO_3$ photocatalysts for PSRM. Moreover, the effect of La^{3+} doping on the structure and photocatalytic activity. In chapter 6, the solid state reaction method was applied to prepare the $CaTiO_3$:La photocatalysts. The structure and its photocatalytic activity were investigated.

Table 1. Summary of photocatalysts for the photocatalytic steam reforming of methane under similar experimental condition.

Photocatalyst	S_{BET} / $m^2\ g^{-1}$	H_2 production rate / μmol h^{-1}	Light source	Ref.
$Pt/CaTiO_3$	1.7	34.8	60	[13]
$Pt/NaTaO_3$:La	2.0	72	300 W Xe (14 mW cm^{-2})	[21]
$Rh/Na_2Ti_6O_{13}$	0.93	58	14	[22]
$Rh/K_2Ti_6O_{13}$	2.3	90	14	[18]
$Pt/CaTiO_3$:La	1.9	19	25	[23]
$Ag/SrTiO_3$	45.1	2.18	–	[24]
Pt/TiO_2	54	10	–	[25]
Pd/TiO_2	54	3	–	[26]

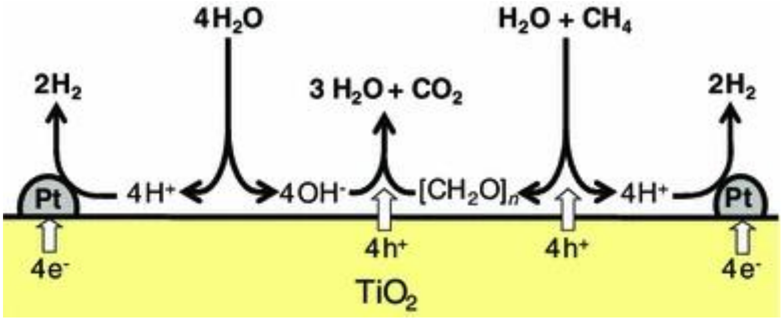

Figure 1. Proposed mechanism for PSRM.[8]

Reference

[1] J. Ancheyta, M. S. Rana, E. Furimsky, *Catal. Today* **2005**, *109*, 3–15.

[2] M. S. Dresselhaus, I. L. Thomas, *Nature* **2001**, *414*, 332–337.

[3] M. De Falco, L. Di Paola, L. Marrelli, **2007**, *32*, 2902–2913.

[4] L. Barelli, G. Bidini, F. Gallorini, S. Servili, *Energy* **2008**, *33*, 554–570.

[5] A. Iulianelli, G. Manzolini, M. De Falco, S. Campanari, T. Longo, S. Liguori, A. Basile, *Int. J. Hydrogen Energy* **2010**, *35*, 11514–11524.

[6] L. Yuliati, H. Yoshida, *Chem. Soc. Rev.* **2008**, *37*, 1592–1602.

[7] K. Shimura, H. Yoshida, *Energy Environ. Sci.* **2011**, *4*, 2467–2481.

[8] K. Shimura, H. Yoshida, *Catal. Surv. from Asia* **2014**, *18*, 24–33.

[9] H. Song, X. Meng, Z. J. Wang, Z. Wang, H. Chen, Y. Weng, F. Ichihara, M. Oshikiri, T. Kako, J. Ye, *ACS Catal.* **2018**, *8*, 7556–7565.

[10] A. M. Pennington, R. A. Yang, D. T. Munoz, F. E. Celik, *Int. J. Hydrogen Energy* **2018**, *43*, 15176–15190.

[11] B. Han, W. Wei, M. Li, K. Sun, Y. H. Hu, *Chem. Commun.* **2019**, in press.

[12] K. Shimura, H. Miyanaga, H. Yoshida, *Stud. Surf. Sci. Catal.* **2010**, *175*, 85–92.

[13] K. Shimura, H. Yoshida, *Energy Environ. Sci.* **2010**, *3*, 615.

[14] K. Shimura, T. Yoshida, H. Yoshida, *J. Phys. Chem. C* **2010**, *114*, 11466–11474.

[15] K. Shimura, H. Yoshida, *Phys. Chem. Chem. Phys.* **2012**, *14*, 2678–2684.

[16] K. Shimura, K. Maeda, H. Yoshida, *J. Phys. Chem. C* **2011**, *115*, 9041–9047.

[17] K. Shimura, H. Kawai, T. Yoshida, H. Yoshida, *Chem. Commun.* **2011**, *47*, 8958–8960.

[18] K. Shimura, H. Kawai, T. Yoshida, H. Yoshida, *ACS Catal.* **2012**, *2*, 2126–2134.

[19] H. Yoshida, S. Kato, K. Hirao, J.-I. Nishimoto, T. Hattori, *Chem. Lett.* **2007**, *36*, 430–431.

[20] K. Shimura, S. Kato, T. Yoshida, H. Itoh, T. Hattori, H. Yoshida, *J. Phys. Chem. C* **2010**, *114*, 3493–3503.

[21] A. Yamamoto, S. Mizuba, Y. Saeki, H. Yoshida, *Appl. Catal. A Gen.* **2016**, *521*, 125–132.

[22] H. Yoshida, S. Mizuba, A. Yamamoto, *Catal. Today* **2019**, *334*, 30–36.

[23] A. Anzai, K. Fujiwara, A. Yamamoto, H. Yoshida, *Catal. Today* **2020**, *352*, 1–9.

[24] A. Ag, B. Tan, Y. Ye, Z. Huang, L. Ye, M. Ma, Y. Zhou, *Chinese Chem. Lett.* **2020**, *31*, 1530–1534.

[25] L. Yu, Y. Shao, D. Li, *"Applied Catal. B, Environ.* **2017**, *204*, 216–223.

[26] L. Yu, D. Li, *Catal. Sci. Technol.* **2017**, *7*, 635–640.

Chapter 5

Platinum-loaded calcium titanate photocatalysts prepared by a flux method for photocatalytic steam reforming of methane

Abstract

Calcium titanate ($CaTiO_3$) samples were prepared by a flux method with various parameters such as the selection of the flux, presence or absence of the flux, and solute concentration in the molten mixture with the flux. These conditions much influenced the structural and physical properties like morphology, particle size, specific surface area, and photoabsorption bands. The photocatalytic activity of the samples loaded with Pt-cocatalyst ($Pt/CaTiO_3$) were evaluated for the photocatalytic steam reforming of methane around room temperature. It was found that the sample prepared by the flux method realized 3.3 times higher photocatalytic activity than that by a conventional solid state reaction method. Further, La-doping to the $CaTiO_3$ photocatalyst ($Pt/CaTiO_3$:La) was examined. It was revealed that La cation was successfully doped at the Ca site in the $CaTiO_3$ lattice. It is observed that small amount of La-doping anomalously enhanced the crystal growth although it lowered the photocatalytic activity. In contrast, the sample with a moderate amount of La-doping such as 1 mol% exhibited 1.6 times higher photocatalytic activity than the non-doped sample.

Introduction

Hydrogen has been used as an important chemical intermediate, a reductant, a fuel and so on, and recently it has attracted much attention as a clean energy for our daily life since it exhausts just water when we use it, which is environment-friendly. Currently, most of hydrogen is produced through an industrial process from natural gas, i.e., steam reforming of methane (SRM)[1]. The process consists of multiple catalytic reactions and the entire chemical equation can be shown as Eq.1[2].

$$CH_4 + 2\ H_2O \rightarrow 4\ H_2 + CO_2 \qquad \Delta G^{\ominus}_{298K} = 113.5\ \mathrm{kJ\ mol^{-1}} \qquad (1)$$

The highly endergonic property of the reaction requires high reaction temperature, typically more than 1073 K, even in the presence of practical catalysts[2]. The high temperature operation causes several problems such as the large energy consumption, the unfavorable carbon formation, and the necessity of expensive reactor[3]. Thus, lowering the operation temperature has been highly desired in SRM. In order to decrease the reaction temperature and utilize sustainable solar energy, heterogeneous photocatalysis has been proposed for SRM as one of possible methods since photocatalysis can take place even at a lower temperature under photoirradiation[4–9].

We discovered platinum-loaded semiconductor photocatalysts, such as Pt/TiO_2 and Pt/$NaTaO_3$:La, can continuously promote photocatalytic steam reforming of methane (PSRM) around room temperature[10–12], and developed several kinds of metal loaded photocatalyst such as Pt/$CaTiO_3$[13,14], Pt/Ga_2O_3[15–17], and Rh/$K_2Ti_6O_{13}$[18,19]. Among these studies, it is demonstrated that the photocatalytic activity can be improved by doping suitable amount of a certain metal cation to the semiconductor, e.g., La^{3+} to $NaTaO_3$[10,12] and Mg^{2+} or Zn^{2+} to Ga_2O_3[15,16]. Recently, it was found that fine and regularly shaped crystals of photocatalyst such as $NaTaO_3$[20] and $Na_2Ti_6O_{13}$[21] prepared by a flux method exhibits higher activity in PSRM than untailored particles prepared by a conventional solid state reaction method. In the present study, we examined a flux method and La^{3+}-doping to improve the photocatalytic activity of Pt/$CaTiO_3$ photocatalyst. We synthesized several doped and non-doped $CaTiO_3$ photocatalysts by a flux method with various conditions and a conventional solid state reaction method, characterized them in several methods, and evaluated them in PSRM.

Experimental

Catalyst preparation

A series of La-doped $CaTiO_3$ compounds (denoted as CTO:La hereafter) were synthesized by a flux method and a solid state reaction method. The starting materials, $CaCO_3$ (Rare Metallic, 99.9%), TiO_2 (rutile, Kojundo, 99.9%), and La_2O_3 (Kishida, 99.99%) were mixed with a flux, such as NaCl (Kishida, 99.5%), KCl (Kishida, 99.5%), and $CaCl_2$ (Kishida, 95.0%): The molar ratio of $CaCO_3$, TiO_2, and La_2O_3 was $(100-x) : 100 : x/2$, where x showed the aimed doping amount of La ($x = 0, 0.5, 1, 2, 3$ and 5 mol%), and various concentration (y) of the solute in the molten flux mixture ($y = 5, 10, 30, 50, 70$, and 90 mol%; typically 50 mol%) were examined, where y was defined as: y [mol%] = 100 × (amount of CTO:La [mol]) / (amount of CTO:La [mol] + amount of a flux [mol]). The mixture of the starting materials and the flux in an aluminum crucible covered by a lid was heated at a rate of 200 K h^{-1} to 1373 K in an electric furnace, held at this temperature for 10 h, and then cooled down to 973 K at a cooling rate of 100 K h^{-1}, followed by natural cooling to room temperature in the furnace. The obtained product was dispersed in hot ion-exchanged water (500 mL, 353 K) and filtrated with suction to remove the flux. The washing procedure was repeated three times, and then dried at 323 K overnight. These samples are referred to as CTO(*flux*, y) for non-doped samples like CTO(NaCl, 50), and CTO:La(x, *flux*, y) for La-doped samples, like CTO:La(0.5, KCl, 50).

Another sample was prepared by a solid state reaction (SS) method without using the flux, corresponding to y=100, without La doping. The starting mixture of $CaCO_3$ and TiO_2 was ground well, followed by calcination in the same manner. The sample is referred to as CTO(SS).

Platinum co-catalyst was loaded onto the prepared CTO and CTO:La samples by an impregnation method. The sample was soaked in an aqueous solution of H_2PtCl_6 (Wako, 99.9%), evaporated at 331 K to dryness in a rotary evaporator, and then calcined at 673 K for 2 h. The samples are referred to as Pt(z)/CTO:La(x, F, y), where z= indicates the loading amount of Pt ($z = 0, 0.03, 0.05, 0.1, 0.15$ and 0.2 wt%; typically 0.05 wt%).

Characterization

X-ray diffraction (XRD) measurement was carried out at room temperature with a Shimadzu Lab X XRD-6000 using Cu Kα radiation (40 kV, 30 mA). The angle was corrected according to a diffraction of Si powder mixed with each sample. The crystallite size was determined by Scherrer equation using the full width at half maximum (FWHM) of the diffraction line at 2θ=33.1° in the XRD patterns of $CaTiO_3$ only when the average crystallite size over the limit of the application of Scherrer equation such as 100-200 nm[22].

Images of scanning electron microscopy (SEM) were taken by a JEOL JSM-890. Diffuse reflectance (DR) UV-visible spectrum was recorded on a JASCO V-670 equipped with an integrating sphere covered with a $BaSO_4$ reference. The band gap was estimated from the spectrum according to Tauc plot. The BET specific surface area was estimated from the amount of N_2 adsorption at 77 K measured using a Quantachrome Monosorb MS-21.

X-ray absorption fine structure (XAFS) at La K-edge were recorded using a Si(311) monochromator in a transmission mode at NW-10A[23] of Photon Factory, Institute of Material Structure Science, High Energy Accelerator Research Organization (KEK-PF), Tsukuba, Japan. X-ray photoelectron spectroscopy (XPS) measurements were acquired using an X-ray photoelectron spectrometer (ESCA 3400, Shimadzu Corp.).

Photocatalytic activity tests

Photocatalytic reaction tests for the PSRM were carried out with a fixed-bed flow reactor as described in our previous studies[20,21]. The catalyst powder was pressed under 20 MPa for 1 min and ground into granules of 300–600 μm. The catalyst granules (0.7–0.8 g) were put into a quartz reactor (ca. $50 \times 20 \times 1$ mm^3), where the irradiation area was regulated to be 6.0 cm^2[21]. The reaction gas mixture composed of 25% CH_4 and 0.75% H_2O with an argon carrier was introduced at a flow rate of 15 mL min^{-1} at atmospheric pressure under light shielding condition for 30 min, and then the catalyst cell was irradiated from a 300 W xenon lamp without using any optical filter, where the light intensity was 25 mW cm^{-2} measured in the range of 254±10 nm. The temperature was measured to be around 323 K. The outlet gas was analyzed by online gas chromatography with a thermal conductivity detector at an interval of ca. 30 min. Since the sensitivity for CO_2 in the argon carrier was low, the experimental error for the values of CO_2 production rate was relatively large.

Results and discussion

Non-doped CTO samples prepared by a flux method with various fluxes.

The effects of a flux method and the kind of flux were studied before an examination of the doping effect. First, several $CaTiO_3$ samples were prepared by a flux method using various fluxes with the same solute concentration of 50%, and by a SS method. Figure 1 shows the XRD patterns of these samples. From the diffraction patterns in the wide range (Figure 1A), the crystal structure of these samples can be assigned to the orthorhombic perovskite $CaTiO_3$. In Figure 1B, the diffraction line at 69.5° of these samples are shown. For the CTO(NaCl, 50) sample prepared by using a NaCl flux, a slight shift to the low angle side was observed (Figure 1Ba). The ionic radius of Na^+ ions (1.39 Å when the coordination number (CN) is 12) contained in the flux is larger than that of Ca^{2+} ions (1.34 Å, CN=12), suggesting that Na^+ ions partially substituted for Ca^{2+} ions at the A-site of the perovskite structure. The CTO(KCl, 50) sample prepared using a KCl flux exhibited no shift (Figure 1Bb), indicating that K^+ ions (1.64 Å, CN=12) were not substituted for Ca^{2+}. In addition, the width of the diffraction line was slightly larger than that of the CTO(SS) sample prepared by the SS method. This means that the sample prepared using the KCl flux consisted of smaller crystallites compared to the sample prepared by the SS method, which is consistent with the SEM image as mentioned later (Figure 2). For the CTO($CaCl_2$, 50) sample prepared using a $CaCl_2$ flux, the diffraction line was slightly shifted to the higher angle (Figure 1Bc). This shift to higher angle was observed only when the $CaCl_2$ flux was used. Since the ionic radius of Al^{3+} ion (0.54 Å, CN=6) is smaller than that of Ti^{4+} ion (0.605 Å, CN=6), it is suggested that Al^{3+} ions from the alumina crucible partially substituted for Ti^{4+} ions at the B-site of the perovskite structure[24]. This would be due to high solubility of Al_2O_3 in the $CaCl_2$ flux, since Al_2O_3 can be dissolved in a molten $CaCl_2$, which can be applied to electrochemical aluminum metal production[25], but not in molten NaCl and KCl fluxes[26].

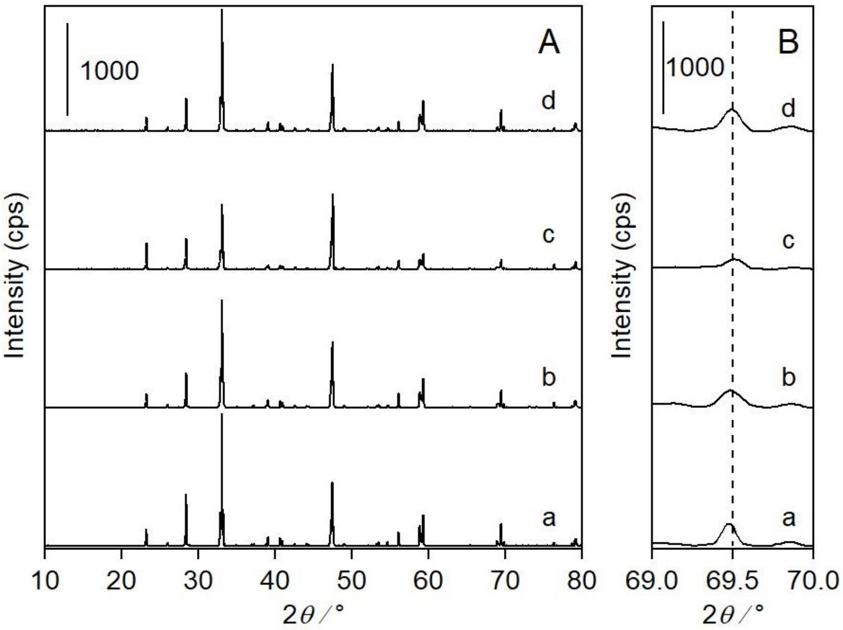

Figure 1. XRD patterns of the CTO(*flux*, 50) samples, (a) CTO(NaCl, 50), (b) CTO(KCl, 50), and (c) CTO($CaCl_2$, 50), and (d) the CTO(SS) sample. The angle was corrected according to a diffraction of Si powder mixed with each sample.

SEM images of these CTO samples are shown in Figure 2. The particles of the sample prepared by the SS method exhibited irregular shape of ca. 0.54 µm on an average size. The samples prepared by the flux method consisted of particles with rather characteristic shapes, which would be regulated by the employed molten salts. The CTO(NaCl, 50) and CTO(KCl, 50) samples showed polyhedral particles, where some facets were found on the surface and the average sizes were ca. 0.43 and 0.60 µm, respectively. The $CaCl_2$ flux gave well-regulated cubic or rectangular crystals of larger size like ca. 9 µm, which is obviously larger than the particles of other samples, which is consistent with the smaller BET specific surface area (Table 1). In general, a flux can contribute to fabricate well-defined crystals covered with facets. In this method, since supersaturation with decreasing temperature or evaporation of flux would be major driving forces for crystallization, the solubility of the materials would be an important factor. It is known that the presence of common anion or cation in the flux often increase the solubility of substrate[27,28]. Thus, the solubility of the Ca^{2+} cation from the start material in the $CaCl_2$ flux is considered to be higher than that in the other fluxes [25,26]. As a result, the $CaCl_2$ flux would enhance the crystal growth of $CaTiO_3$.

Table 1 Physical and optical properties of the $CaTiO_3$:La samples prepared by the flux method and the photocatalytic property of the Pt(0.05)/$CaTiO_3$:La samples in the photocatalytic steam reforming of methane.

Entry	Flux reagent	Solute concentration[a] (mol%)	La content (mol%)	Crystallite size (XRD)[b] / nm	Particle size (SEM)[c] / µm	S_{BET}[d] / m^2g^{-1}	H_2 production rate[e] / µmol h^{-1}
1	NaCl	50	0	–[f]	0.43	1.16	1.2
2	KCl	50	0	–	0.60	2.30	12
3	$CaCl_2$	50	0	–	9.0	0.35	1.2
4	(SS method)	100	0	–	0.54	1.58	3.6
5	KCl	10	0	–	0.37	2.54	1.2
6	KCl	30	0	–	0.38	2.75	1.2
8	KCl	70	0	–	0.4	2.22	5.4
9	KCl	90	0	–	0.47	2.11	7.8
10	KCl	50	0.1	–	1.1	1.37	4.2
11	KCl	50	0.5	–	1.4	0.92	2.4
12	KCl	50	0.7	–	1.1	1.41	6.6
13	KCl	50	1	–	0.45	1.85	19
14	KCl	50	3	36.2	0.21	4.40	14
15	KCl	50	5	30.5	0.2	4.73	6.0

[a] Solute concentration in the molten mixture. See the text for the calculation. [b] Average crystallite size of $CaTiO_3$ calculated from a line width at 2θ=33.1° in the XRD patterns. [c] Average particle size of $CaTiO_3$ estimated from the SEM images. [d] Specific surface area obtained from the BET method. [e] The hydrogen production rate was evaluated at 3 h later from the start of photoirradiation. [f] Average crystallite size over the limit of the application of Scherrer equation such as 100–200 nm [22].

In the DR UV-visible spectra (Figure 3), the CTO(NaCl, 50), CTO(KCl, 50), and CTO(SS) samples exhibited the absorption edge around 350 nm in wavelength and the estimated band gap was 3.5 eV. The CTO(SS) sample showed additionally a small shoulder near the absorption edge at 350–400 nm in wavelength. Although no impurity phase was observed in the XRD pattern (Figure 1), this shoulder would be assigned to amorphous-like TiO_2, although the other possibilities such as crystal defects could not be excluded. This small absorption has been observed for $CaTiO_3$ samples prepared by solid state reaction methods in our previous studies[13,29,30]. The CTO($CaCl_2$, 50) sample exhibited a red-shifted threshold at 360 nm, corresponding to 3.4 eV, and also the similar band around absorption edge as well as a broad absorption band in the visible light region of 400–800 nm. The latter wide absorption band would derive from defects such as color centers[31] or Al^{3+} impurity from alumina crucible as discussed above[24]. The substitution of Al^{3+} for Ti^{4+} at the B-site would form residual amorphous-like TiO_2 species showing the former band around absorption edge.

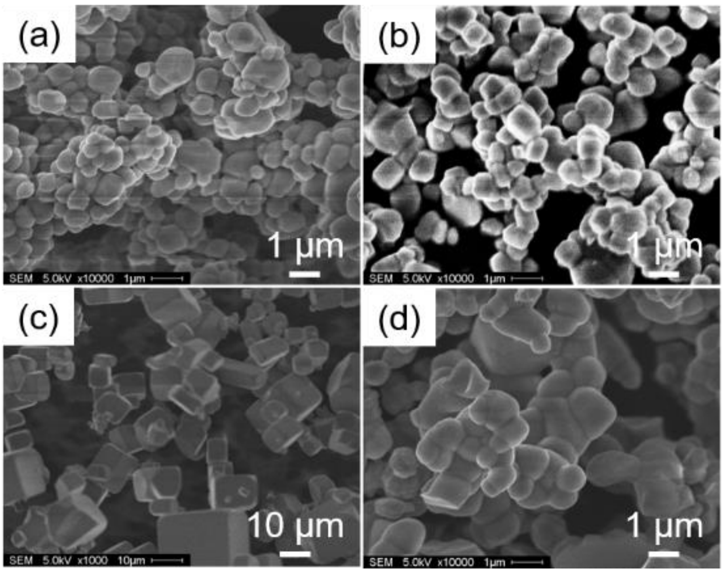

Figure 2. SEM images of the CTO(*flux*, 50) samples, (a) CTO(NaCl, 50), (b) CTO(KCl, 50), and (c) CTO($CaCl_2$, 50), and (d) the CTO(SS) sample.

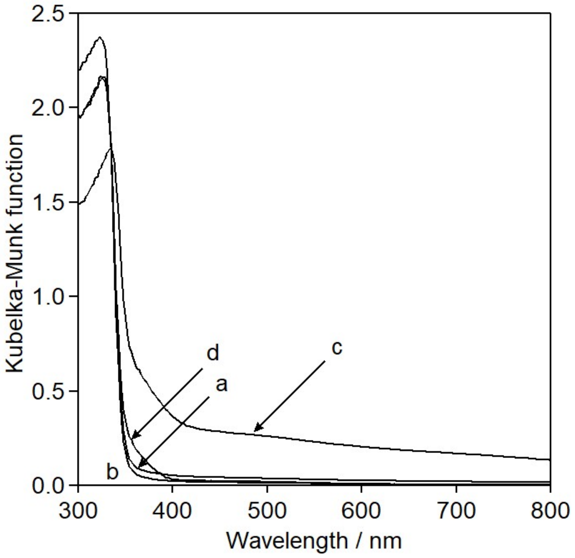

Figure 3. DR UV-visible spectra of the CTO(*flux*, 50) samples, (a) CTO(NaCl, 50), (b) CTO(KCl, 50), and (c) CTO($CaCl_2$, 50), and (d) the CTO(SS) sample.

The photocatalytic reaction tests were carried out for these samples, on which 0.05 wt% of Pt cocatalyst was deposited before the reaction test. Figure 4 shows a time course of the production rate of H_2 and CO_2 as well as these ratio (H_2/CO_2) in the photocatalytic reaction test with the Pt(0.05)/CTO(KCl, 50) sample as a representative. Without photoirradiation, no products were observed. Upon photoirradiation, although the production rates of H_2 and CO_2 initially varied with time, both of them became constant after 2 h, and the formation ratio also became stable around 4. These results suggest that the PSRM proceeded as expected according to the Eq. 1.

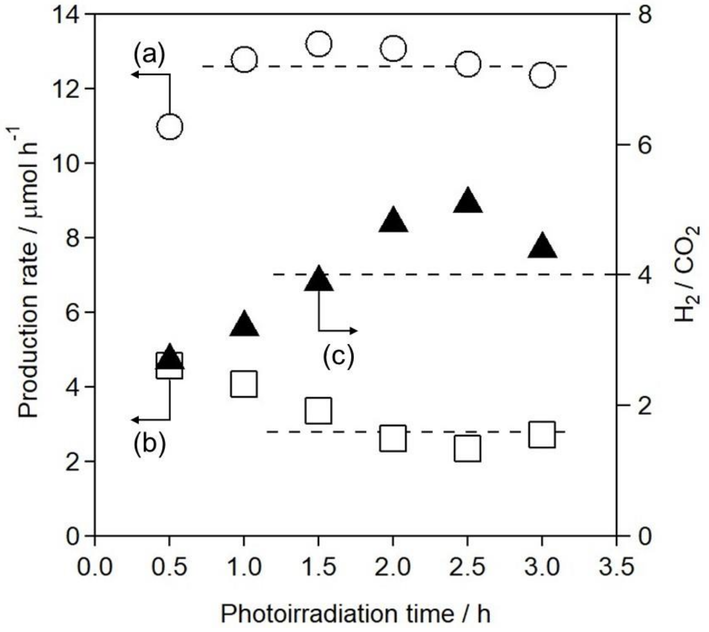

Figure 4. Time course of the production rates of (a) H_2 and (b) CO_2 (left), and (c) the ratio of H_2/CO_2 (right) in the photocatalytic reaction test with Pt(0.05)/CTO(KCl, 50) sample.

Figure 5 shows the H_2 production rates in the PSRM with the Pt(0.05)/CTO catalysts. The Pt(0.05)/CTO(KCl, 50) sample prepared by the flux method with a KCl flux exhibited the highest production rate among them, which was 3.3 times higher than the Pt(0.05)/CTO(SS) sample prepared by the conventional SS method. The Pt(0.05)/CTO(NaCl, 50) and Pt(0.05)/CTO($CaCl_2$, 50) samples exhibited lower production rates than the Pt(0.05)/CTO(SS) sample.

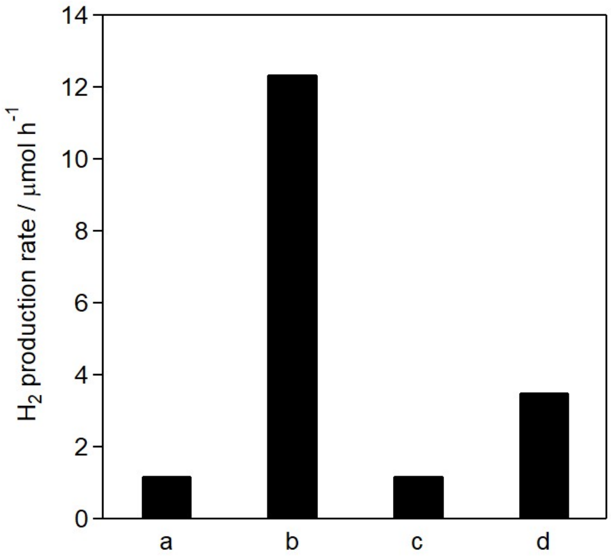

Figure 5. Hydrogen production rate in PSRM with the Pt(0.05)/CTO(*flux*, 50) samples, (a) Pt(0.05)/CTO(NaCl, 50), (b) Pt(0.05)/CTO(KCl, 50), and (c) Pt(0.05)/CTO($CaCl_2$, 50), and (d) the Pt(0.05)/CTO(SS) sample.

The H_2 production rate with these photocatalysts are listed in Table 1 entries 1–4, in which particle size determined from SEM images and specific surface area of these samples are also listed. Although no clear relationship was found between particle size and H_2 production rate, the sample with larger specific surface area tended to show higher photocatalytic activity among them. However, as discussed later, this trend cannot be always found, indicating there are some structural factors controlling the photocatalytic activity and the most important factor cannot be determined easily. The results of characterization revealed that the Pt(0.05)/CTO(KCl, 50) sample had fine polyhedral crystals with less impurities substituted and a larger specific surface area. It was proposed that less impurities and the larger specific surface area would contribute to the improvement of the activity.

As a conclusion of this section, the sample prepared with a KCl flux can exhibit the highest photocatalytic performance in PSRM. Thus, we focused further investigation on the samples prepared with the KCl flux.

Non-doped CTO samples prepared with various solute concentrations.

In the XRD patterns of the CTO(KCl, *y*) samples prepared using a KCl flux with different solute concentration (*y* mol%) and the CTO(SS) sample (Figure 6), all the samples presented clear diffraction lines assignable to $CaTiO_3$ crystal without any impurity phase and any shift. SEM images revealed that the CTO(KCl, *y*) samples consisted of polyhedral particles of 0.4–0.6 µm in size (Figure 7 and Table 1 entries, 2 and 5–9). It was found that a moderate concentration of the solutes such as 50% gave the largest particle size such as 0.6 µm determined by the SEM images. Figure 8 shows DR UV-visible spectra. All the samples had an absorption edge around 350 nm. The CTO(KCl, 10) sample showed less absorption at 350–400 nm than others. The sample with larger solute concentration exhibited the broad absorption band in 400–800 nm, suggesting that the CTO(KCl, *y*) samples prepared using a larger amount of KCl flux tends to have less defects. Since a flux acts as a solvent for crystallization of the aimed material[27,28], small amount of flux (90% of solute) would not enough for the complete crystallization. A moderate amount of flux would provide a suitable concentrations of the starting materials and enough space to achieve a homogenous dispersion of the formed particles, which would enhance the crystal growth to give larger size of well-crystallized particles covered with well-defined facets. The moderate amount of flux would be 50% to fabricate the fine $CaTiO_3$ crystals in the present conditions.

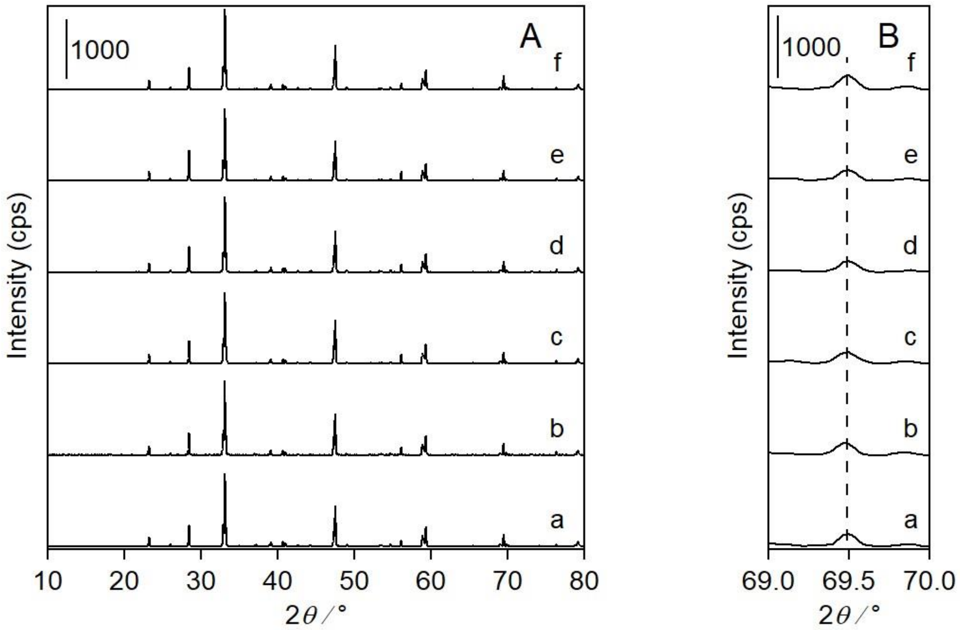

Figure 6. XRD patterns of the CTO(KCl, *y*) samples, (a) CTO(KCl, 10), (b) CTO(KCl, 30), (c) CTO(KCl, 50), (d) CTO(KCl, 70), and (e) CTO(KCl, 90), and (f) the CTO(SS) sample. The angle was corrected according to a diffraction of Si powder mixed with each sample.

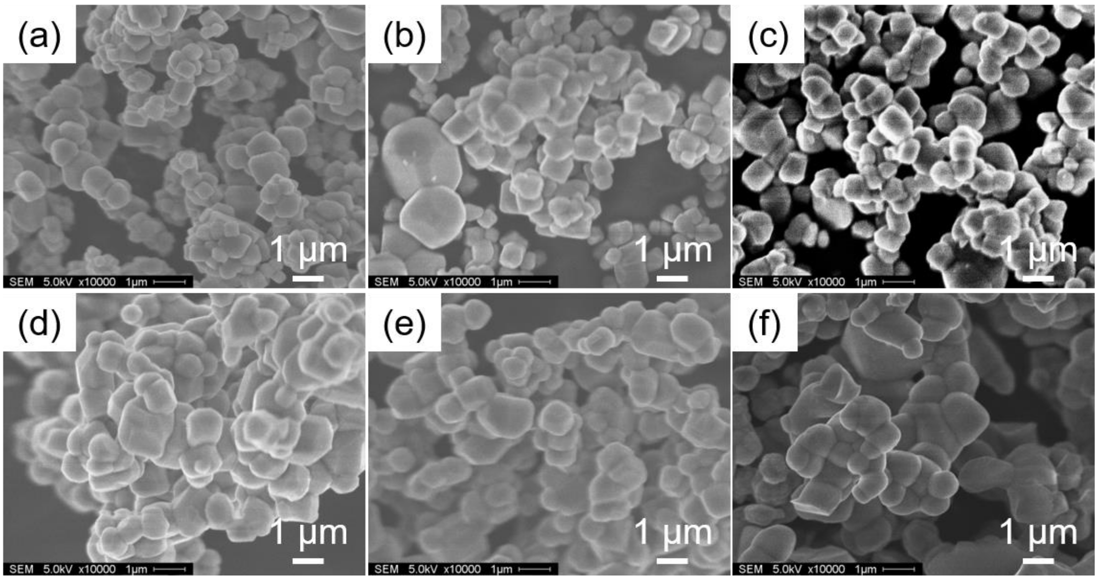

Figure 7. SEM images of the CTO(KCl, *y*) samples, (a) CTO(KCl, 10), (b) CTO(KCl, 30), (c) CTO(KCl, 50), (d) CTO(KCl, 70), and (e) CTO(KCl, 90), and (f) the CTO(SS) sample.

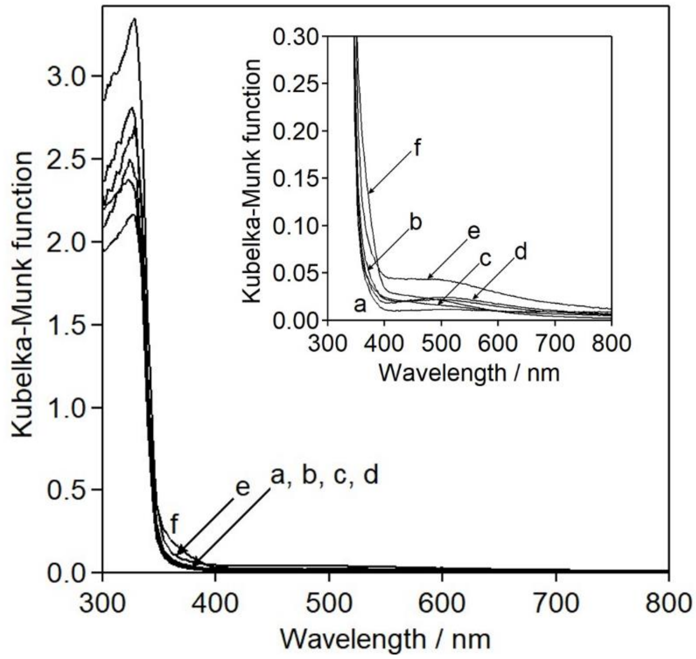

Figure 8. UV-vis spectra of the CTO(KCl, *y*) samples, (a) CTO(KCl, 10), (b) CTO(KCl, 30), (c) CTO(KCl, 50), (d) CTO(KCl, 70), and (e) CTO(KCl, 90), and (f) the CTO(SS) sample.

Figure 9A shows the hydrogen production rates in the PSRM with the Pt(0.05)/CTO(KCl, *y*) photocatalysts using the KCl flux with different solute concentration (*y* mol%). The H_2 production rate increased with increasing the solute concentration up to 50 mol%. The sample prepared with a solute concentration of 50 mol% in a molten mixture gave the highest production rate such as 12 μmol h^{-1} among them. However, higher solute concentrations than 50 mol% decreased the photocatalytic activity. As mentioned above, the CTO(KCl, 50) samples had large size of well-crystallized polyhedral particles with less defects, which would contribute to the highest activity among these samples. This consists with the previous studies of $NaTaO_3$[20] and $Na_2Ti_6O_{13}$[21] photocatalysts prepared via a flux method for PSRM, where the photocatalyst prepared with a moderate solute concentration gave the highest activity.

Figure 9B shows the hydrogen production rates with the Pt(*x*)/CTO(KCl, 50) photocatalysts of various Pt loading amount (*x* wt%). The Pt(0.05)/CTO(KCl, 50) sample exhibited the highest production rate among them. The samples with Pt loading amount lower and higher than 0.05 wt% exhibited lower photocatalytic activity, which is possibly caused by some reasons, such as an aggregation of the Pt species[32], an increase of recombination sites[33], shielding light reaching photocatalyst[34], and varying the Pt fermi level[32].

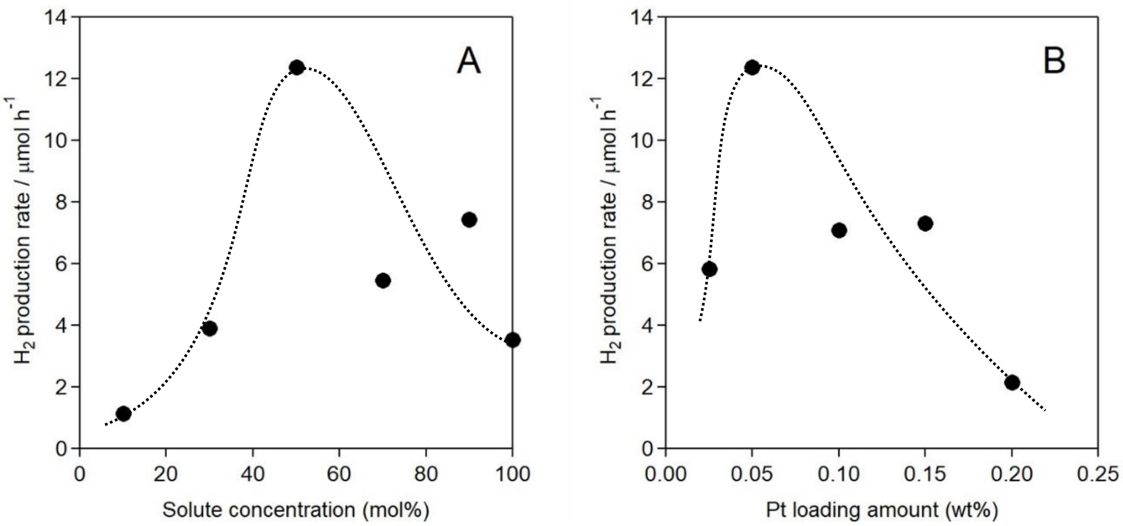

Figure 9. Hydrogen production rate in PSRM with (A) the Pt(0.05)/CTO(KCl, *y*) samples prepared by a flux method with various solute concentration (*y* mol%) in a KCl flux, and (B) the Pt(*x*)/CTO(KCl, 50) samples of various Pt loading amount (*x* wt%).

So far we have investigated some photocatalyst systems for PSRM, such as $NaTaO_3$:La[20], $Na_2Ti_6O_{13}$[21], and $CaTiO_3$ (This study), prepared by a flux method. In any cases, the samples prepared by a flux method exhibited higher activity than the samples prepared by a SS method (Table 2). The Pt/$NaTaO_3$:La photocatalyst prepared using a NaCl flux exhibited 1.6 times higher activity than the sample prepared by a SS method (Table S1 entries 2 and 3). The Rh/$Na_2Ti_6O_{13}$ photocatalyst prepared using a NaCl flux showed only 1.1 times higher activity than the sample prepared by a SS method (Table S1, entries 4 and 5). In the current Pt/$CaTiO_3$ photocatalyst prepared using a KCl flux showed 3.3 times higher activity than the sample prepared by a SS method. The flux method can be proposed as a superior method than the conventional solid state reaction method to provide an active photocatalyst for PSRM. The current $CaTiO_3$ photocatalyst was most improved by the flux method among the three photocatalyst systems mentioned above.

In conclusion of this section, the Pt(0.05)/CTO(KCl, 50) sample exhibited the highest activity, which would originate from the well-crystalized, large polyhedral $CaTiO_3$ crystals with less defects and less impurity, loaded with a moderate amount of Pt cocatalyst. Thus, we moved on the investigation of La doping effect on the photocatalyst.

Table 2. Results of photocatalytic reaction tests for the photocatalytic steam reforming of methane.

Entry	photocatalyst	flux	S_{BET} / m^2 g^{-1}	Cocatalyst (wt%)	H_2 production rate[a] / µmol h^{-1}	Light intensity[b] / mW cm^{-2}	ref
1	$NaTaO_3$	NaCl	0.9	Pt (0.03)	1.2	14	[20]
2	$NaTaO_3$:La	NaCl	2.0	Pt (0.03)	72	14	[20]
3	$NaTaO_3$:La	(SS method)	2.1	Pt (0.03)	45	14	[20]
4	$Na_2Ti_6O_{13}$	NaCl	0.93	Rh (0.05)	58	14	[21]
5	$Na_2Ti_6O_{13}$	(SS method)	0.75	Rh (0.05)	51	14	[21]
6	$CaTiO_3$	KCl	2.3	Pt (0.05)	12	25	[c]
7	$CaTiO_3$:La	KCl	1.9	Pt (0.05)	19	25	[c]
8	$CaTiO_3$	(SS method)	1.6	Pt (0.05)	3.6	25	[c]

The photocatalyst powder was filled in the cell to occupy each required area; 7.0 cm^2 for entries 1–5, and 6.0 cm^2 for entries 6–8. [a] H_2 production rate was monitored at 4 h (entries 1–3), 5 h (entries 4 and 5), and 3 h (entries 6–8) later from the start of photoirradiation. [b] Light source was a 300 W xenon lamp without using any optical filter, where the light intensity was measured in the range of 254 ± 10 nm. [c] This study.

La-doped CTO samples prepared by a KCl flux

La-doped samples were prepared by using a KCl flux with various La doping amount. Figure 10A shows the XRD patterns of the CTO:La(*x*, KCl, 50) samples with various La doping amount. The entire patterns were assignable to the $CaTiO_3$ perovskite structure except for details. In Figure 10B focuses a diffraction line at 69.5°. With increasing La doping amount from 0.5 to 5 mol%, the diffraction line shifted to lower angle. This suggests that La^{3+} (1.36 Å, CN=12) was doped into the $CaTiO_3$ lattice to substitute for Ca^{2+} (1.34 Å, CN=12) at the A-site in the perovskite ABO_3

structure by using the flux method. Since the ionic radius of the six-coordinated La^{3+} ion (1.032 Å, CN=6) is much larger than that of Ti^{4+} ion (0.605 A, CN=6) and the observed shift of the diffraction line was not so large, it is considered that La^{3+} could not substitute for Ti^{4+}.

When the La content was 0.5 mol% (Figure 10b), the line intensities were higher and the widths were lower than those of non-doped sample, indicating the crystal growth with less strain was enhanced on the CTO:La(0.5, KCl, 50) sample. The CTO:La(1, KCl, 50) sample exhibited almost the same intensity and width as those of the non-doped CTO(KCl, 50) sample (Figure 10c), suggesting that the substituted La are present without much influence on the crystal growth of $CaTiO_3$. With increasing La doping amount more than 1 mol%, the diffraction lines became weeker and broader, especially the line at 69.5° almost disappeared when 5 mol% La was doped, suggesting that the crystal structure were much varied. The substitution by La^{3+} cation having the slightly larger ionic radius and the higher valence than those of Ca^{2+} would distort the crystal structure, generate many crystal defects, and thus make the diffraction line broad and ambiguous.

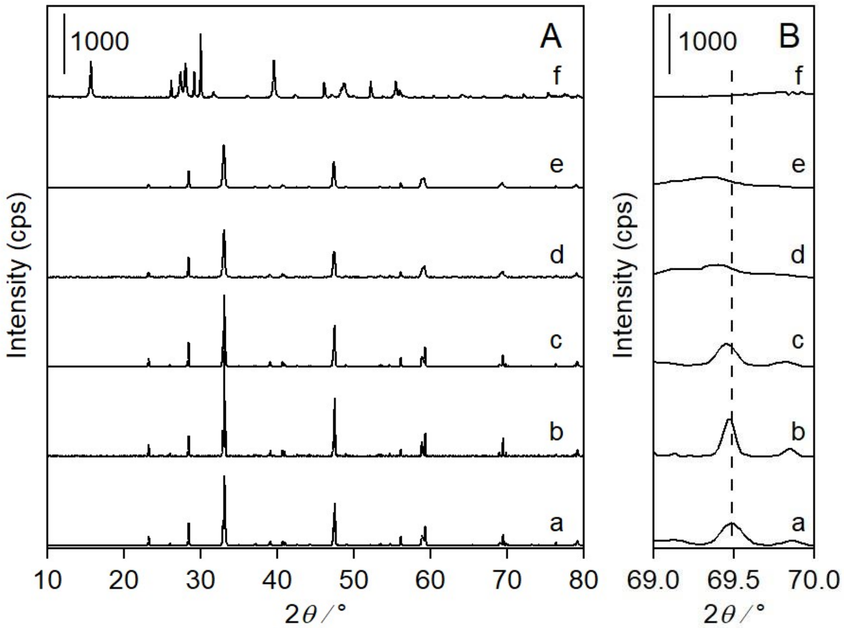

Figure 10. XRD patterns of the CTO:La(x, KCl, 50) samples in the range of (A) 10°–80° and (B) 69°–70°, where La doping amount x was (a) 0, (b) 0.5, (c) 1, (d) 3, and (e) 5 mol %, and (f) La_2O_3 as a reference.

Figure 11 shows their SEM images. The polyhedral morphology was not so changed by La doping. However, the particle size was drastically changed by La doping as listed in Table 1, entries 10–15 and plotted in Figure 12. The particle size drastically increased by the La doping when the amount of La was less than 1 mol% (Figure 11b and Table 1, entries 10–12). The maximum particle size was 1.4 µm on an average for the CTO:La(0.5, KCl, 50) sample (Table 1 entry 11), which was 2.3 times larger than that of the non-doped CTO(KCl, 50) sample (Table 1, entry 2). Similar observations of this characteristic crystal growth have been reported, e.g., for $SrTiO_3$ doped with Y^{3+}, La^{3+}, Nd^{3+}, Ho^{3+}, Nb^{5+}, and Sb^{5+}[35–37], which is well-known as an anomaly of grain growth of donor-doped perovskite materials, so-called “donor anomaly”[36], the mechanism of which has been thermodynamically explained[38]. Except for the samples with low La doping amount less than 1 mol%, the particle size tends to decrease with the increase of the doping amount in the range of 1–5 mol% (Figure 12). This means that small amount of La cations enhanced the anomalous crystal growth of $CaTiO_3$ in the molten flux, while larger amount of La suppressed it.

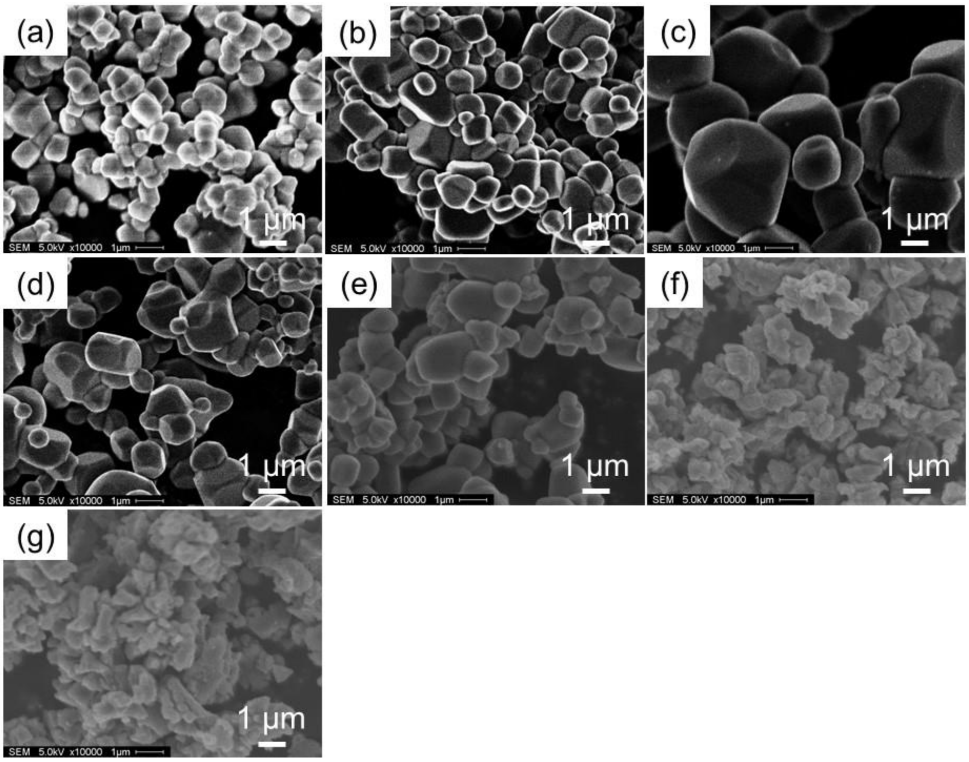

Figure 11. SEM images of the CTO:La(*x*, KCl, 50) samples with different La doping amount *x*; (a) 0, (b) 0.1, (c) 0.5, (d) 0.7, (e) 1, (f) 3, and (g) 5 mol%.

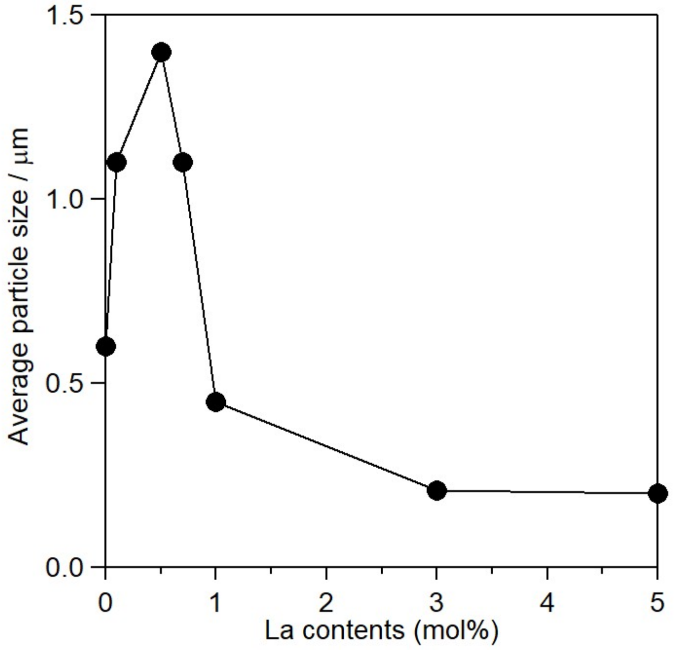

Figure 12. The average particle size determined from SEM images of the CTO:La(*x*, KCl, 50) samples with different La doping amount (*x* mol%).

Figure 13 shows the DR UV-visible spectra of the CTO:La(*x*, KCl, 50) samples with various La doping amount (0–5 mol%). All the samples exhibited the same threshold at 350 nm in wavelength, corresponding to the bandgap of 3.5 eV. The non-doped sample exhibited a band at 350–400 nm and a very small and broad band centered at 500 nm (Figure 13a). The both bands were suppressed by doping 0.5 mol% La, suggesting that La doping suppresses the formation of defects in $CaTiO_3$ crystals. Further doping of La more than 1 mol% increased the band at 350–400 nm without showing another broad band at 500 nm.

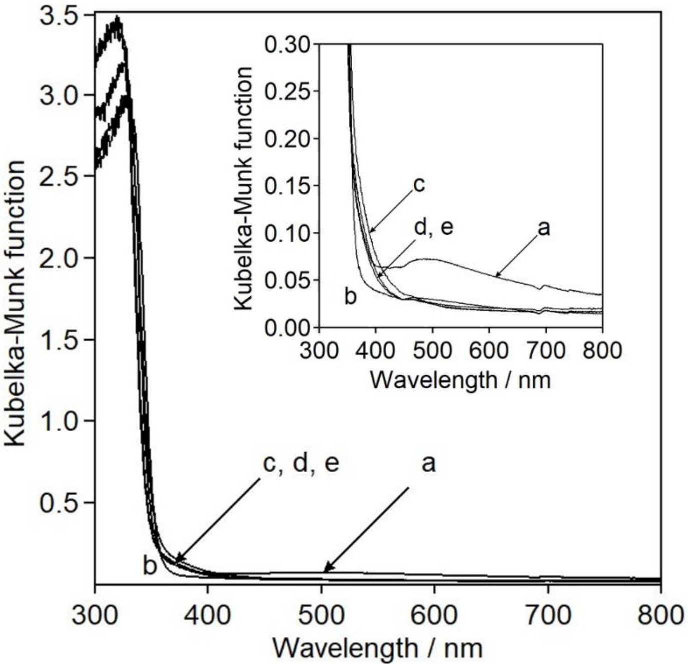

Figure 13. DR UV-visible spectra of the CTO:La(*x*, KCl, 50) samples with different La doping amount *x*; (a) 0, (b) 0.5, (c) 1, (d) 3, and (e) 5 mol%.

To elucidate the state of the doped La ions, XAFS spectra were measured and analyzed. XANES spectra of the CTO:La(*x*, KCl, 50) samples are resemble to that of La_2O_3 (Figure 14A), because of the less characteristic feature of La K-edge XANES at high energy of incident X-ray such as 39 keV and unchangeable valence of La^{3+} cation. The EXAFS oscillations of the all CTO:La samples (Figure 14B, a–d), were clearly different from that of La_2O_3 (Figure 14B, e), indicating the local structure of major La^{3+} ions in the CTO:La(*x*, KCl, 50) samples, with x=0.5, 1, 3, and 5 mol %, are quite different from that in the trigonal structure of La_2O_3. In the Fourier Transformed EXAFS of the CTO:La(*x*, KCl, 50) samples (Figure 14C, a–d), the first and the second neighboring atoms were clearly observed around at 1.9 and 2.9 Å, respectively, which were clearly different from and closer than that of La_2O_3 (Figure 14C, e) and similar to the reported one for a $NaTaO_3$:La(La 0.5 mol%) photocatalyst [12]. It is clear that the local structure of La^{3+} cation in each CTO:La sample with doping amount of 0.5–5 mol% was similar to each other and different from that in La_2O_3 crystal, supporting that La^{3+} cation substituted for the Ca^{2+} cation in the $CaTiO_3$ structure. Thus, the absorbing La^{3+} ions are located at the A-site in ABO_3 perovskite structure and are coordinated with twelve O^{2-} anions and surrounded by eight Ti^{4+} cations at the B-site, which would correspond to the peaks at 1.9 and 2.9 Å, respectively. It was also confirmed that the average local structure of La was not varied so much with the La contents in these samples.

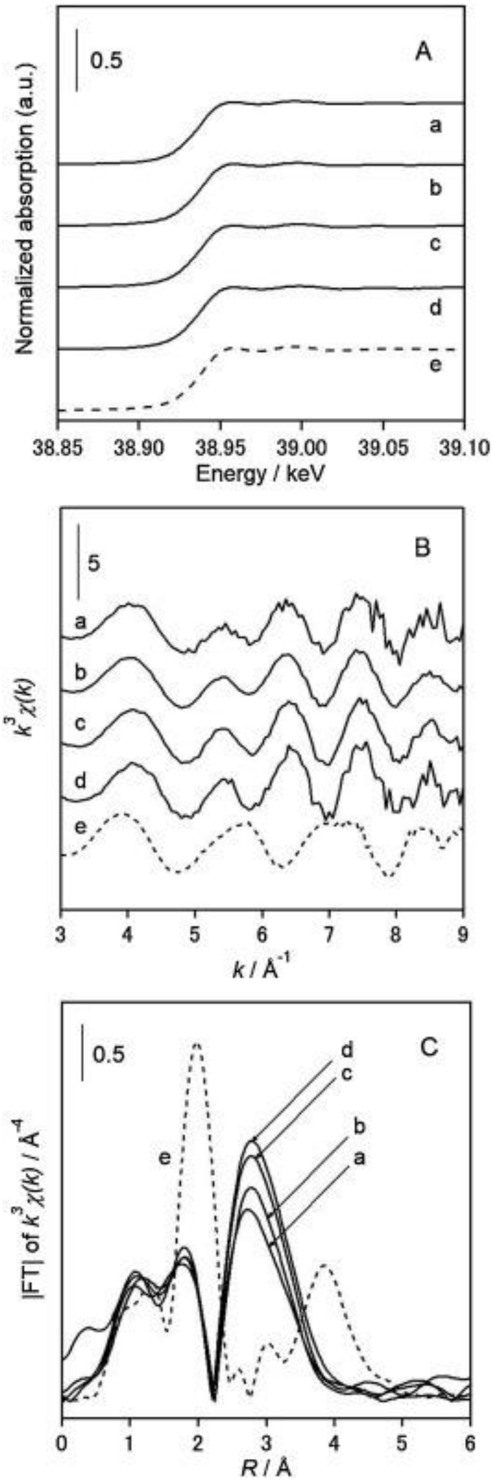

Figure 14. (A) La K-edge XANES spectra, (B) EXAFS oscillations, and (C) Fourier transforms of the EXAFS oscillation for the CTO(*x*, KCl, 50) samples, where La doping amount *x* was (a) 0.5, (b) 1, (c) 3, and (d) 5 mol%, and (e) those for La_2O_3 as a reference.

Figure 15 shows XPS spectra of La 3d bands for the CTO:La(*x*, KCl, 50) samples and La_2O_3. The $3d_{5/2}$ and $3d_{3/2}$ bands observed at 835 and 852 eV, respectively, were accompanied with each satellite band at higher binding energy side, which are assigned to charge-transfer satellite bands from neighboring oxygen to the La [39]. The shapes of $3d_{5/2}$ and $3d_{3/2}$ bands of the CTO:La(0.5, KCl, 50) sample (Figure 15a) were quite different from those of La_2O_3 (Figure 15d), *i.e.*, the satellite bands were relatively larger than those of La_2O_3. This means that La^{3+} ions in the $CaTiO_3$ structure had a unique electronic state that is different from those in the bulk oxide of La_2O_3 because of larger interaction with surrounding oxygen anions. As shown in the Fourier transformed EXAFS (Figure 15C), the distances between La^{3+} cation and neighboring oxygen anions in the $CaTiO_3$ lattice, are shorter than those in La_2O_3, which is consistent with the relatively larger satellite bands. Thus, it is suggested that the La^{3+} cation substituted for Ca^{2+} cation would provide larger interaction with oxygen anions. In contrast, a similar band shape to that of La_2O_3 was found for the CTO:La(5, KCl, 50) sample (Figure 15c), meaning the La^{3+} ions in the highly La-doped sample are rather similar electronic state with that in the bulk La_2O_3. As mentioned above, the EXAFS analysis (Figure 15C) clarified that the La^{3+} cation in the samples substituted Ca^{2+} cation in the $CaTiO_3$ structure. The ambiguous X-ray diffraction line (Figure 10Be) means that the perovskite structure of $CaTiO_3$ was much influenced by the 5 mol% La doping. These facts propose that the large amount of La^{3+} cations was substituted for Ca^{2+} cations in the $CaTiO_3$ crystal and they have the similar electronic state of La^{3+} cations to that of La_2O_3. The CTO:La(1, KCl, 50) sample exhibited similar band shape to the low doping sample but also showed slightly similar character to the high doping sample.

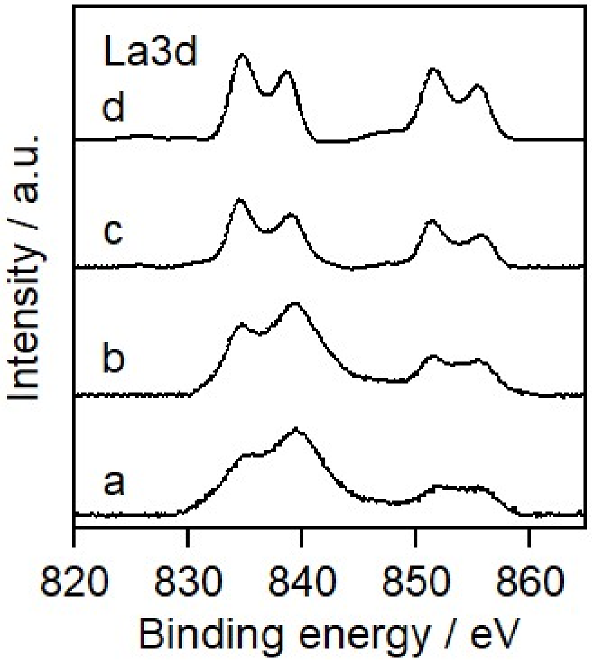

Figure 15. La 3d bands XPS spectra of the CTO(x, KCl, 50) samples with La doping amount x; (a) 0.5, (b) 1, and (c) 5 mol%, and (d) that of La_2O_3 as a reference.

Finally, the photocatalytic activity test in PSRM were carried out for the Pt-loaded La-doped $CaTiO_3$ photocatalysts with various lanthanum doping amounts (Table 1, entries 10–15). Figure 16 depicts the hydrogen production rate over the Pt(0.05)/CTO:La(x, KCl, 50) samples and non-doped Pt(0.05)/CTO(KCl, 50) sample. Among them, the Pt(0.05)/CTO:La(1, KCl, 50) sample exhibited the highest H_2 production rate such as 19 μmol h^{-1}, which was 1.6 times larger than non-doped Pt(0.05)/CTO:La(KCl, 50) sample and the best performance in the present study. The low amount of La-doping less than 1 mol% drastically decreased the photocatalytic activity such as one fifth of that with the non-doped sample. For the higher amount of La-doping more than 1 mol%, the photocatalytic activity decreased with an increase of La-doping amount.

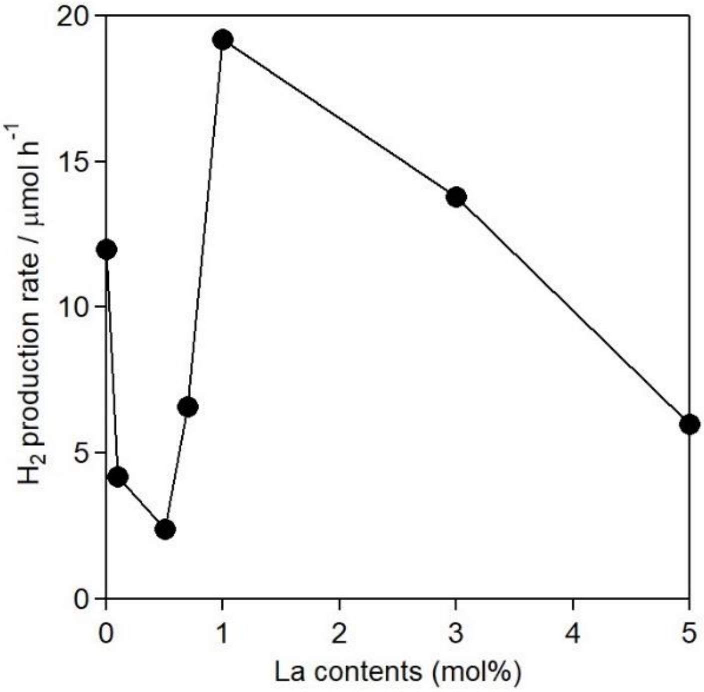

Figure 16. Hydrogen production rate in PSRM with the Pt(0.05)/CTO:La(*x*, KCl, 50) samples prepared by a flux method with various La contents (*x* mol%).

The photocatalytic activity should be related to the structural properties. At least, it was clarified that the defects showing the absorption bands in visible light region decrease the photocatalytic activity. However, other structural properties could not simply explain the photocatalytic activity. The large size of the particles with a low specific surface area according to anomalous crystal growth by small amount of La doping less than 1 mol% exhibited low activity (Table 1 entries 10–12). The variation of the specific surface area could not quantitatively explain the variation of the photocatalytic activity. In the photocatalyst crystal, only the photogenerated electrons and holes reaching the surface without recombination can take part in the photocatalytic reaction, and thus the crystal edges providing both the reductive and oxidative reaction fields would decrease the recombination to increase the photocatalytic activity[40]. Thus, a large crystal having less edges would show less activity. The higher amount of La-doping more than 1 mol% decreased the crystal size and the photocatalytic activity with an increase of La-doping amount (Table 1, entries 13–15). As one possibility, since these samples would be of low crystallinity judging from the ambiguous x-ray diffraction lines, these samples might have many crystal defects that cannot be detected by DR

UV-vis spectra and these defects would act as the recombination sites for the photoexcited electrons and holes.

Conclusions

In the present study, the fine polyhedral $CaTiO_3$ (CTO) crystals were synthesized by a flux method and a conventional solid state reaction (SS) method for an application to the photocatalytic steam reforming of methane (PSRM). The type of fluxes and the solute concentration in the molten mixture much affected the structure of the CTO crystals, such as crystal shape, crystal size, crystallinity, specific surface area, and amount of defects. The Pt-loaded sample prepared using a KCl flux showed 3.3 times higher H_2 production rate than the sample prepared by the conventional SS method.

Furthermore, the lanthanum doped CTO photocatalysts (CTO:La) were prepared by the flux method using a KCl flux. La cation was successfully doped at the Ca site in the $CaTiO_3$ lattice. The addition of La in small amount induced the crystal growth of the CTO, but larger amount of La suppressed the growth. The sample with a moderate amount of La, Pt(0.05)/CTO:La(1, KCl, 50), exhibited the highest H_2 formation rate in the present study, which was 1.6 times higher than the non-doped sample prepared by the flux method, Pt(0.05)/CTO(KCl, 50), and 5.3 times higher than non-doped sample prepared by the solid state reaction method, Pt(0.05)/CTO(SS).

References

[1] D. Das, T. N. Veziroglu, *Int. J. Hydrogen Energy* **2001**, *26*, 13–28.

[2] L. Barelli, G. Bidini, F. Gallorini, S. Servili, *Energy* **2008**, *33*, 554–570.

[3] J. Tong, Y. Matsumura, *Appl. Catal. A Gen.* **2005**, *286*, 226–231.

[4] L. Yuliati, H. Yoshida, *Chem. Soc. Rev.* **2008**, *37*, 1592–1602.

[5] K. Shimura, H. Yoshida, *Energy Environ. Sci.* **2011**, *4*, 2467–2481.

[6] K. Shimura, H. Yoshida, *Catal. Surv. from Asia* **2014**, *18*, 24–33.

[7] H. Song, X. Meng, Z. J. Wang, Z. Wang, H. Chen, Y. Weng, F. Ichihara, M. Oshikiri, T. Kako, J. Ye, *ACS Catal.* **2018**, *8*, 7556–7565.

[8] A. M. Pennington, R. A. Yang, D. T. Munoz, F. E. Celik, *Int. J. Hydrogen Energy* **2018**, *43*, 15176–15190.

[9] B. Han, W. Wei, M. Li, K. Sun, Y. H. Hu, *Chem. Commun.* **2019**, in press.

[10] H. Yoshida, S. Kato, K. Hirao, J.-I. Nishimoto, T. Hattori, *Chem. Lett.* **2007**, *36*, 430–431.

[11] H. Yoshida, K. Hirao, J.-I. Nishimoto, K. Shimura, S. Kato, H. Itoh, T. Hattori, *J. Phys. Chem. C* **2008**, *112*, 5542–5551.

[12] K. Shimura, S. Kato, T. Yoshida, H. Itoh, T. Hattori, H. Yoshida, *J. Phys. Chem. C* **2010**, *114*, 3493–3503.

[13] K. Shimura, H. Miyanaga, H. Yoshida, *Stud. Surf. Sci. Catal.* **2010**, *175*, 85–92.

[14] K. Shimura, H. Yoshida, *Energy Environ. Sci.* **2010**, *3*, 615.

[15] K. Shimura, T. Yoshida, H. Yoshida, *J. Phys. Chem. C* **2010**, *114*, 11466–11474.

[16] K. Shimura, H. Yoshida, *Phys. Chem. Chem. Phys.* **2012**, *14*, 2678–2684.

[17] K. Shimura, K. Maeda, H. Yoshida, *J. Phys. Chem. C* **2011**, *115*, 9041–9047.

[18] K. Shimura, H. Kawai, T. Yoshida, H. Yoshida, *Chem. Commun.* **2011**, *47*, 8958–8960.

[19] K. Shimura, H. Kawai, T. Yoshida, H. Yoshida, *ACS Catal.* **2012**, *2*, 2126–2134.

[20] A. Yamamoto, S. Mizuba, Y. Saeki, H. Yoshida, *Appl. Catal. A Gen.* **2016**, *521*, 125–132.

[21] H. Yoshida, S. Mizuba, A. Yamamoto, *Catal. Today* **2019**, *334*, 30–36.

[22] U. Holzwarth, N. Gibson, *Nat. Nanotechnol.* **2011**, *6*, 534–534.

[23] M. Nomura, Y. Koike, M. Sato, A. Koyama, Y. Inada, K. Asakura, *AIP Conf. Proc.* **2007**, *882*, 896–898.

[24] Y. Ham, T. Hisatomi, Y. Goto, Y. Moriya, Y. Sakata, A. Yamakata, J. Kubota, K. Domen, *J. Mater. Chem. A* **2016**, *4*, 3027–3033.

[25] H. Kadowaki, Y. Katasho, K. Yasuda, T. Nohira, *J. Electrochem. Soc.* **2018**, *165*, D83–D89.

[26] Y. Xiao, K. Tang, in *Proc. VIII Int. Conf. Molten Slags, Fluxes Salts*, **2009**, pp. 1393–1401.

[27] D. E. Bugaris, H. C. Zur Loye, *Angew. Chemie - Int. Ed.* **2012**, *51*, 3780–3811.

[28] K. H. Yoon, Y. S. Cho, D. H. Kang, *J. Mater. Sci.* **1998**, *33*, 2977–2984.

[29] H. Yoshida, R. Yamada, T. Yoshida, *ChemSusChem* **2019**, *12*, 1958–1965.

[30] H. Yoshida, L. Zhang, M. Sato, T. Morikawa, T. Kajino, T. Sekito, S. Matsumoto, H. Hirata, *Catal. Today* **2015**, *251*, 132–139.

[31] K. Lehovec, G. A. Shirn, *J. Appl. Phys.* **1962**, *33*, 2036–2044.

[32] H. Yuzawa, T. Mori, H. Itoh, H. Yoshida, *J. Phys. Chem. C* **2012**, *116*, 4126–4136.

[33] K. Wang, Z. Wei, B. Ohtani, E. Kowalska, *Catal. Today* **2018**, *303*, 327–333.

[34] N. Bao, L. Shen, T. Takata, K. Domen, *Chem. Mater.* **2008**, *20*, 110–117.

[35] I. Burn, S. Neirman, *J. Mater. Sci.* **1982**, *17*, 3510–3524.

[36] C. Peng, Y. Chiang, *J. Mater. Res.* **1990**, *5*, 1237–1245.

[37] S. Hui, A. Petric, *J. Eur. Ceram. Soc.* **2002**, *22*, 1673–1681.

[38] M. Drofenik, *J. Am. Ceram. Soc.* **1993**, *76*, 123–128.

[39] G. Crecelius, G. K. Wertheim, D. N. E. Buchanan, *Phys. Rev. B* **1978**, *18*, 6519–6524.

[40] H. Kato, K. Asakura, A. Kudo, *J. Am. Chem. Soc.* **2003**, *125*, 3082–3089.

Chapter 6

Platinum-loaded lanthanum-doped calcium titanate photocatalysts prepared by a solid state reaction method for photocatalytic steam reforming of methane

Abstract

Hydrogen production from methane steam reforming process at low temperature is desired. The photocatalytic steam reforming of methane is attractive in that it proceeds at room temperature and ambient pressure. At present, the efficiency of this process is remarkably low, and it is necessary to increase the photocatalytic activity of the photocatalysts. La doped $CaTiO_3$ samples prepared by a solid state reaction method with various La contents were investigated. As the La content was increased, the added La was not completely substituted into the $CaTiO_3$ but partially deposited as La_2O_3, and that the added lanthanum was abundant on the calcium titanate surface. The Pt/$CaTiO_3$:La sample with doping amount of 5 mol% showed 15 times higher photocatalytic activity than Pt/$CaTiO_3$ sample. It was shown that the hydrogen production rate increased with the increase in the surface La concentration.

Introduction

Hydrogen is essential to chemical industry, such as ammonia synthesis[1], methanol synthesis[2], olefin synthesis[3], and so on. In addition, hydrogen have been expected to be a new fuel to replace fossil fuels in recent years. Currently, most of hydrogen is produced through catalytic steam reforming of methane (SRM) from natural gas. [4]. The process consists of multiple catalytic reactions and the entire chemical equation can be writen as Eq.1 [5].

$$CH_4 + 2\ H_2O \rightarrow 4\ H_2 + CO_2 \qquad \Delta G^{\ominus}_{298K} = 113.5\ \text{kJ mol}^{-1} \qquad (1)$$

The highly endergonic property of the reaction requires high reaction temperature, typically more than 973 K, even in the presence of practical catalysts.[5] Therefore, low temperature process has been highly desired in SRM. We discovered Pt/$CaTiO_3$ photocatalyst exhibits photocatalytic activity for photocatalytic steam reforming of methane.[6][7] Furthermore, La^{3+} doping to Ca^{2+} ion in A-site of $CaTiO_3$ improves photocatalytic activity.[6] The selection of preparation method is important for developing a highly active photocatalyst. Differences in preparation lead to different photocatalytic activities. When prepared by the solid state reaction method, the spatial distribution of the dopant in the crystal may differ from the surface to the bulk. The concentration distribution of the dopant in the particles can affect the photocatalytic activity.[8]

In this study, the La doped CTO samples prepared by a solid state reaction method with different La dopant amount were investigated, characteraized, and evaluated for photocatalytic steam reforming of methane.

Experimental

Catalyst preparation

A series of La-doped $CaTiO_3$ compounds (denoted as CTO:La hereafter) were synthesized by a solid state reaction (SS) method. The starting materials, $CaCO_3$ (Rare Metallic, 99.9%), TiO_2 (rutile, Kojundo, 99.9%), and La_2O_3 (Kishida, 99.99%) were mixed well using an alumina mortar and pestle: The molar ratio of $CaCO_3$, TiO_2, and La_2O_3 was $(100-x) : 100 : x/2$, where x showed the aimed doping amount of La ($x = 0$, 0.5, 1, 2, 3, 5, and 10 mol%) were examined. The mixture of the starting materials in an aluminum crucible covered by a lid was heated at a rate of 200 K h^{-1} to 1373 K in an electric furnace, held at this temperature for 10 h, and then cooled down to 973 K at a cooling rate of 100 K h^{-1}, followed by natural cooling to room temperature in the furnace. These samples are referred to as CTO:La (SS, x).

Platinum co-catalyst was loaded onto the prepared CTO and CTO:La samples by an impregnation method. The sample was soaked in an aqueous solution of H_2PtCl_6 (Wako, 99.9%), evaporated at 331 K to dryness in a rotary evaporator, and then calcined at 673 K for 2 h. The samples are referred to as Pt/CTO:La(SS, x). The loading amount of Pt was 0.05 wt%.

Characterization

X-ray diffraction (XRD) measurement was carried out at room temperature with a Shimadzu Lab X XRD-6000 using Cu Kα radiation (40 kV, 30 mA). The angle was corrected according to a diffraction of Si powder mixed with each sample. The crystallite size was determined by Scherrer equation using the full width at half maximum (FWHM) of the diffraction line at $2\theta=33.1°$ in the XRD patterns of $CaTiO_3$ only when the average crystallite size over the limit of the application of Scherrer equation such as 100-200 nm [9]. Raman spectra of solid samples were measured on a LabRam HR800 (Horiba Ltd.) spectrometer. which has a Ar^+ ion laser light source (Kimmon, IK4401R-D) with a wavelength of excitation (excitation wavelength: 488 nm). Images of scanning electron microscopy (SEM) were taken by a JEOL JSM-890. Diffuse reflectance (DR) UV-visible spectrum was recorded on a JASCO V-670 equipped with an integrating sphere covered with a $BaSO_4$ reference. The band gap was estimated from the spectrum according to Tauc plot. The BET specific surface area was estimated from the amount of N_2 adsorption at 77 K measured using a Quantachrome Monosorb MS-21. X-ray absorption fine structure (XAFS) at La K-edge were recorded using a Si(311) monochromator in a transmission mode at NW-10A [10] of Photon Factory, Institute of Material Structure Science, High Energy Accelerator Research Organization (KEK-PF), Tsukuba, Japan. X-ray photoelectron spectroscopy (XPS) measurements were acquired using an X-ray photoelectron spectrometer (ESCA 3400, Shimadzu Corp.).

Photocatalytic activity tests

Photocatalytic reaction tests for the PSRM were carried out with a fixed-bed flow reactor as described in our previous studies [11,12]. The catalyst powder was pressed under 20 MPa for 1 min and ground into granules of 300–600 μm. The catalyst granules (0.7–0.8 g) were put into a quartz reactor (ca. $50 \times 20 \times 1$ mm^3), where the irradiation area was regulated to be 6.0 cm^2 [12]. The reaction gas mixture composed of 25% CH_4 and 0.75% H_2O with an argon carrier was introduced at a flow rate of 15 mL min^{-1} at atmospheric pressure under light shielding condition for 30 min, and then the catalyst cell was irradiated from a 300 W xenon lamp without using any optical filter, where the light intensity was 25 mW cm^{-2} measured in the range of 254 ± 10 nm. The temperature was measured to be around 323 K. The outlet gas was analyzed by online gas chromatography with a thermal conductivity detector at an interval of ca. 30 min. Since the sensitivity for CO_2 in the argon carrier was low, the experimental error for the values of CO_2 production rate was relatively large.

Results and discussion

Figure 1 shows the XRD pattern of $CaTiO_3$:La prepared by the solid state reaction method. All diffraction lines in the pattern correspond to orthorhombic $CaTiO_3$ with a doping ratio of 0.5 to 3 mol%, and it is considered that single-phase $CaTiO_3$: La was obtained. In the sample prepared at a doping amount of 5 to 10 mol%, unreacted La_2O_3 and TiO_2 peaks were confirmed in addition to $CaTiO_3$. a diffraction pattern consistent with the diffraction pattern of $La_2Ti_2O_7$ was obtained. It was also confirmed that the peak shifts to the low angle side with increasing the La doping ratio increases. This indicates that La^{3+} ion substituted for Ca^{2+} ion in A-site. The diffraction line of La_2O_3 was observed at 15.6° in the 10 mol% doped sample. The diffraction line of TiO_2 with rutile phase was observed at 26.4° in the 10 mol% sample. The diffraction line of $La_2Ti_2O_7$ was observed at 29.9° in the 10 mol% sample.

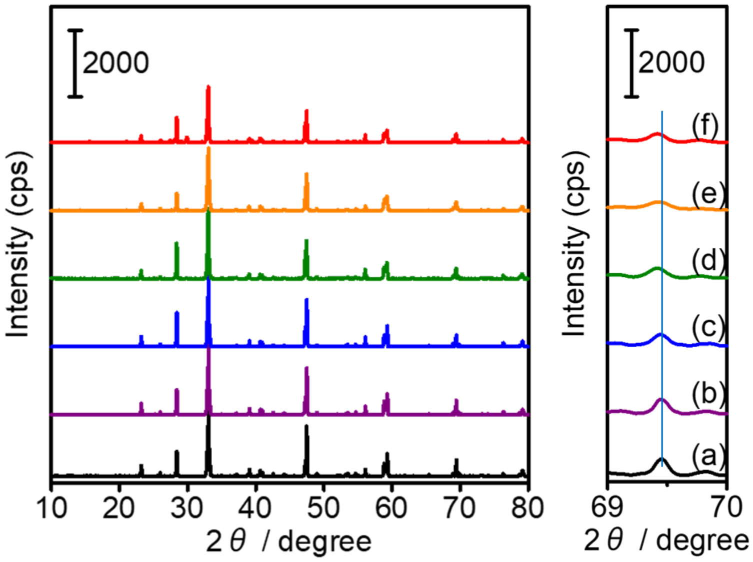

Figure 1. XRD patterns of (a) the $CaTiO_3$(SS), (b) the $CaTiO_3$(SS, 0.5), (c) the $CaTiO_3$(SS, 1), (d) the $CaTiO_3$(SS, 3), (e) the $CaTiO_3$(SS, 5), (f) the $CaTiO_3$(SS, 10). All samples were mixed with pure Si powder (Kojundo) before measurement. Diffraction angle was calibrated by Si with silicon (111) plane at 28.4°.

Figure 2 shows Raman spectra of $CaTiO_3$:La samples. All sample showed Raman mode assignable to $CaTiO_3$-based materials. Another mode at around 800 cm^{-1} appeared in La doped samples. The intensity increased with increasing doping amount. The band can be assigned to A_{1g} mode of octahedral oxygen breathing mode. This mode was not given by occupation of single species in B-site. in the XRD patterns, it can be concluded that La^{3+} ions were doped into Ca^{2+} site in A-site. It is suggested that this mode would appear by introduction of Ti vacancy followed by

$$2La_2O_3 = 4La_{Ca}^{\bullet} + V_{Ti}'''' + 6O_O \quad (2)$$

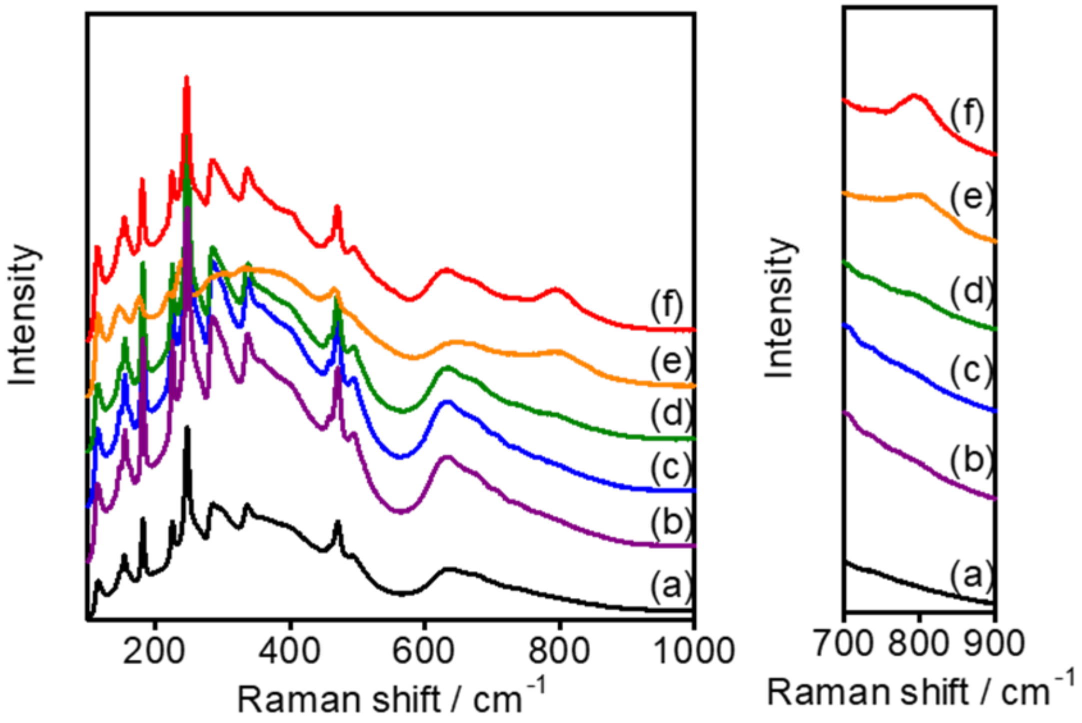

Figure 2. Raman spectra of (a) the $CaTiO_3$(SS), (b) the $CaTiO_3$(SS, 0.5), (c) the $CaTiO_3$(SS, 1), (d) the $CaTiO_3$(SS, 3), (e) the $CaTiO_3$(SS, 5), (f) the $CaTiO_3$(SS, 10).

Figure 3 shows SEM images of CTO:La prepared by the solid state method at various La doping rates. The roundish particles were observed. The particle size of CTO:La samples tended to decrease with increasing La content.

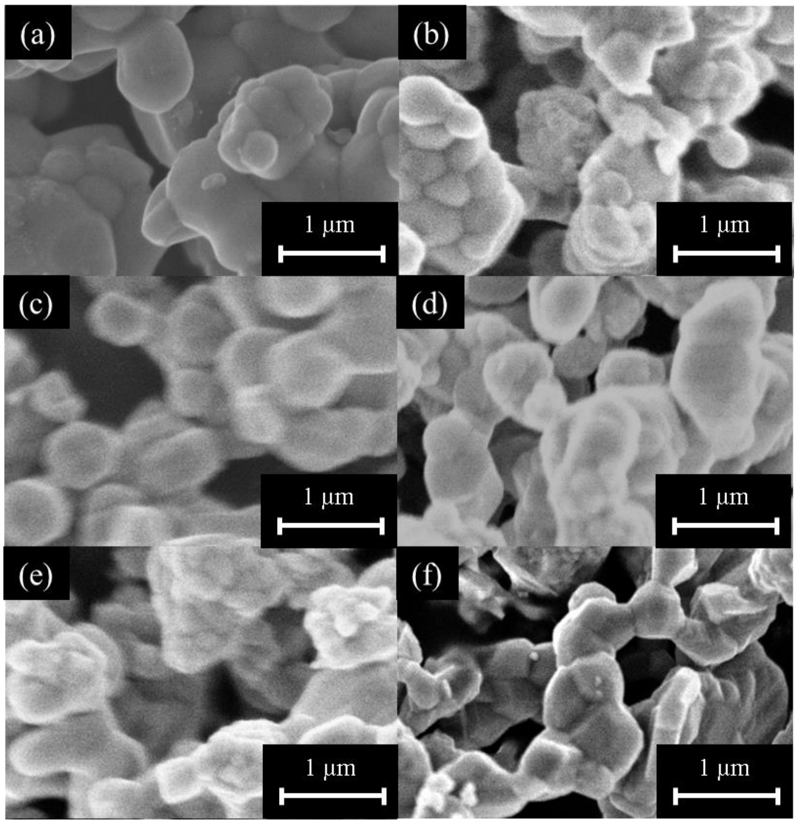

Figure 3. SEM images of (a) the $CaTiO_3$(SS), (b) the $CaTiO_3$(SS, 0.5), (c) the $CaTiO_3$(SS, 1), (d) the $CaTiO_3$(SS, 3), (e) the $CaTiO_3$(SS, 5), (f) the $CaTiO_3$(SS, 10).

Figure 4 shows the diffuse reflectance UV-vis spectra of samples. It was found that the absorption at 370–700 nm was significantly suppressed in the sample doped with La as compared with the non-doped sample. This indicates that oxygen vacancies decreased by La doping.

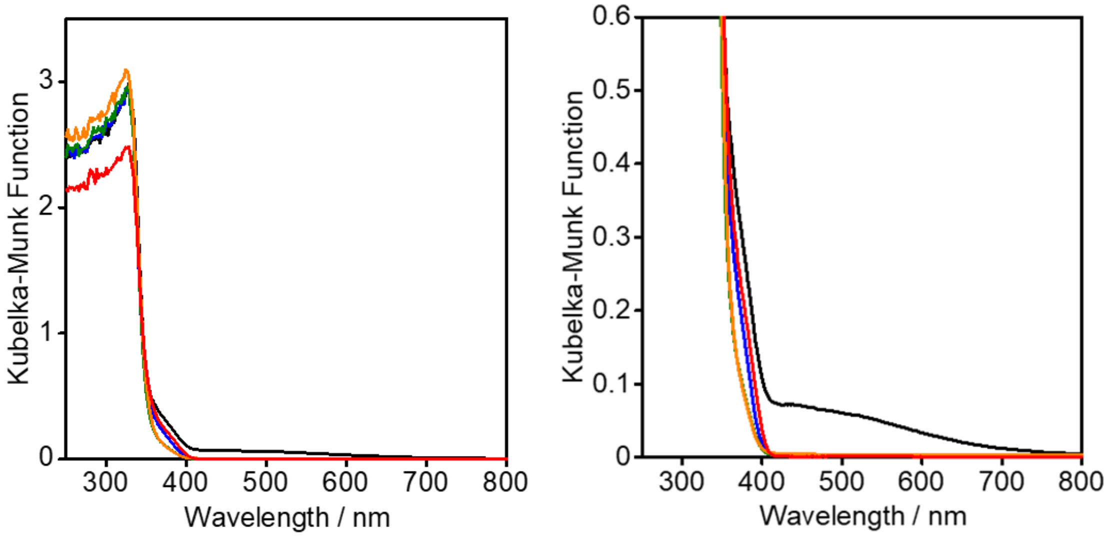

Figure 4. Diffuse reflectance UV-vis spectra of the $CaTiO_3$(SS) (black line), the $CaTiO_3$(SS, 0.5) (purple line), the $CaTiO_3$(SS, 1) (blue line), the $CaTiO_3$(SS, 3) (green line), the $CaTiO_3$(SS, 5) (orange line), the $CaTiO_3$(SS, 10) (red line).

In addition, the presence of titanium vacancies was further confirmed by XPS. The Ti 2p3/2 XPS peak of non-doped sample is located at 457.7 eV, whereas the peak of La doped samples was slightly shifted to higher binding energy. This result would occur because the neighboring O and Ti atoms of V_{Ti} get less electrons compared with those on non-doped sample.[13]

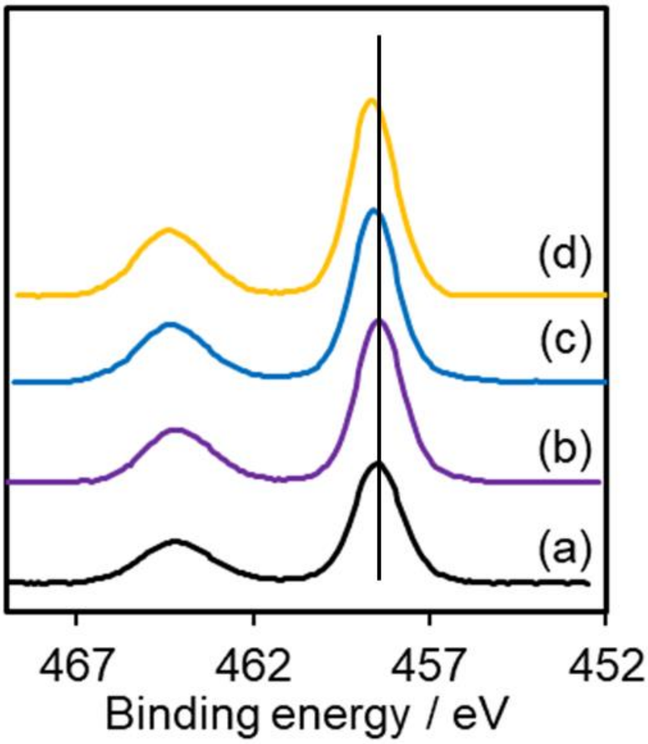

Figure 5. Ti2p XPS spectra of (a) the $CaTiO_3$(SS), (b) the $CaTiO_3$(SS, 0.5), (c) the $CaTiO_3$(SS, 1), and (d) the $CaTiO_3$(SS, 5).

Table 1 shows the atomic composition ratio of $CaTiO_3$ calculated from XPS measurement, and the ratio of La atom to Ca atom on the sample surface calculated from it is plotted against La dope ratio in Figure 6.

Table 1. The surface atomic concentration of the $CaTiO_3$:La samples measured by XPS.

	Ca (mol%)	Ti(mol%)	O(mol%)	La(mol%)
$CaTiO_3$(SS)	10.25	9.93	79.82	0.00
$CaTiO_3$:La(SS, 0.5)	14.10	13.07	72.08	0.76
$CaTiO_3$:La(SS, 1)	17.41	14.15	64.96	3.48
$CaTiO_3$:La(SS, 5)	15.14	12.55	62.37	9.94

Figure 6 shows relationship between La dopant amount and the surface La to Ti atomic ratio calculated by XPS of the samples. the surface La to Ti ratio increased linearly with increasing La dopant amount. The La doped $CaTiO_3$ samples prepared by a solid state reaction method had La rich surface.

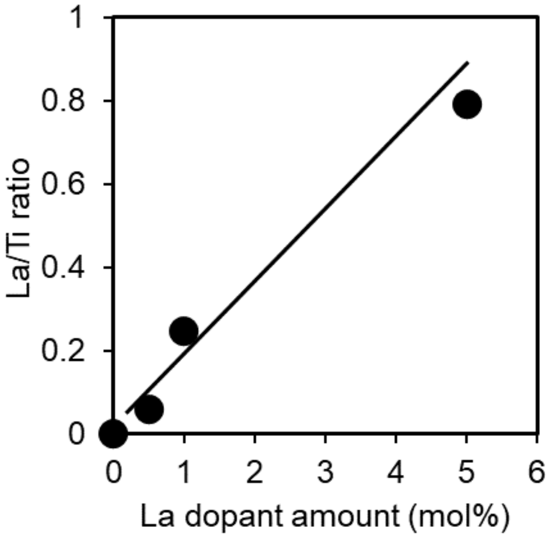

Figure 6. Surface La / Ti atomic ratio calculated by XPS of the samples with various La contents prepared by the solid state reaction method.

Figure 7 shows a time course of the production rates of H_2 and CO_2 as well as these ratio (H_2/CO_2) in the photocatalytic reaction test with the Pt(0.05)/CTO:La(5) sample as a representative. Without photoirradiation, no products were observed. Under photoirradiation, although the production rates of H_2 and CO_2 initially varied with time, both of them became constant after 1.5 h, and the formation ratio also became stable around 4. These results suggest that the PSRM proceeded as expected according to the Eq. 1.

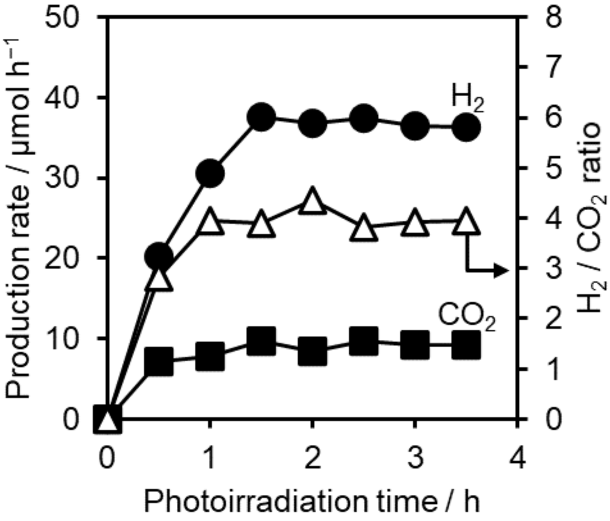

Figure 7. Time course of the production rates of H_2 (black circle) and CO_2 (white square), and the ratio of H_2/CO_2 (white triangle) in the photocatalytic reaction test with the Pt(0.05)/CTO:La(5) sample.

The photocatalytic activity test in the PSRM were carried out for the Pt-loaded La-doped $CaTiO_3$ photocatalysts with various lanthanum doping amounts (Table 1). Figure 8 depicts the hydrogen production rate over the Pt(0.05)/CTO:La(*x*) samples and non-doped Pt(0.05)/CTO sample. Among them, the Pt(0.05)/CTO:La(5) sample exhibited the highest H_2 production rate such as 37 μmol h^{-1}, which was 15 times larger than the non-doped Pt(0.05)/CTO sample and the best performance in the present study.

The low amount of La-doping less than 1 mol% decreased the photocatalytic activity such as half of that with the non-doped sample. For the higher amount of La-doping more than 1 mol%, the photocatalytic activity increased with increasing La dopant amount from 1 mol% to 5 mol%. More than 5 mol% La doping led to decrease in the photocatalytic activity.

Table 2 Physical and optical properties of the $CaTiO_3$:La samples prepared by a solid state reaction method and the photocatalytic property of the Pt(0.05)/$CaTiO_3$:La samples in the photocatalytic steam reforming of methane.

Entry	T [a] / K	Introduced amount of La [c] (mol%)	Crystallite size (XRD) [d] / nm	Particle size (SEM) [e] / nm	S_{BET} [f] / $m^2\ g^{-1}$	Loading amount of Pt (wt%)	H_2 production rate [g] / µmol h^{-1}
1	1373	0	-[h]	0.54	1.58	0.05	3.6
2	1373	0.5	-	0.73	1.77	0.05	1.2
3	1373	1	-	0.64	1.79	0.05	12
4	1373	3	85.11	0.58	1.79	0.05	26
5	1373	5	45.27	0.27	2.14	0.05	37
6	1373	10	80.28	-	6.7	0.05	20

[a] Solute concentration in the molten mixture. See the text for the calculation. [b] Average crystallite size of $CaTiO_3$ calculated from a line width at $2\theta=33.1°$ in the XRD patterns. [c] Average particle size of $CaTiO_3$ estimated from the SEM images. [d] Specific surface area obtained from the BET method. [e] The hydrogen production rate was evaluated at 3 h later from the start of photoirradiation. [f] Average crystallite size over the limit of the application of Scherrer equation such as 100–200 nm [9].

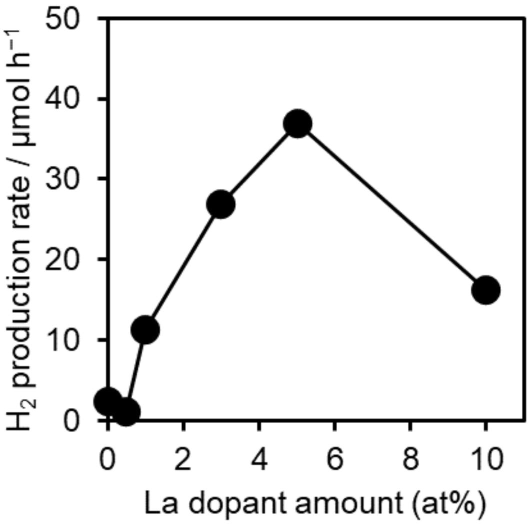

Figure 8. Hydrogen production rate in PSRM with the Pt(0.05)/CTO:La(*x*) samples prepared by the solid state reaction method with various La contents (*x* mol %).

Figure 9 shows the relationship between the hydrogen production rate and the ratio of La atoms to Ca atoms on the surface calculated from XPS. In the sample doped with La, it was confirmed that the sample with higher concentration of La atom on the surface tended to show higher activity. It is considered that La_2O_3 deposited on the particle surface activated methane and contributed to the improvement of photocatalytic activity.

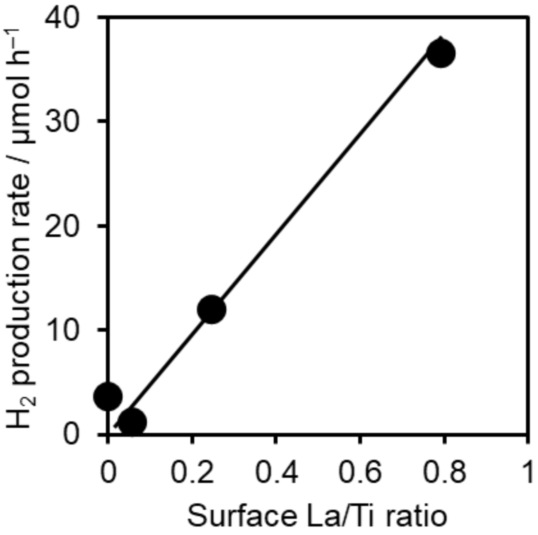

Figure 9. Correlation between surface La / Ti atomic ratio measured by XPS and hydrogen production rate in the photocatalytic steam reforming of methane over the La doped samples and the non-doped sample.

The electronic status of Pt species on the CTO and CTO:La was surveyed by XPS. The Pt 4f peaks of Pt/CTO:La are negatively shifted by about 0.2 eV compared with those of Pt/CTO. This means that probably electron transfer from CTO:La to Pt occur Pt on CTO:La had slightly negative charge that on bare CTO. The increase of electron density on Pt surely improves the electrocatalytic hydrogen evolution reaction HER (HER, $H^+ + 2e^- = H_2$) activities.[14] Subsequently, Pt/CTO:La should have better photocatalytic activity than Pt/CTO.

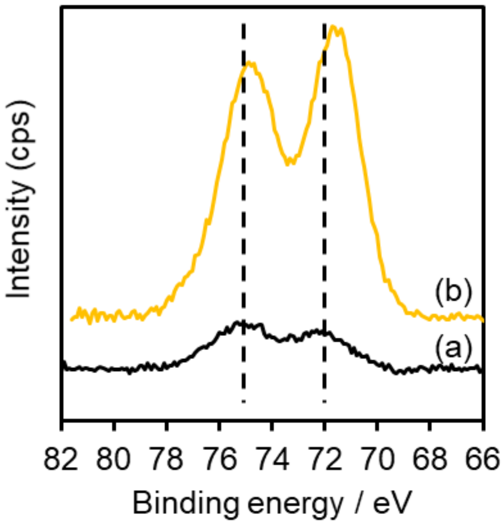

Figure 10. Pt4f XPS spectra of Pt/CTO (a), and Pt/CTO:La(5).

Conclusions

The La-doped $CaTiO_3$ photocatalyst was developed for the photocatalytic steam reforming of methane under mild conditions. A series of the sample was prepared by a solid state reaction method. The obtained sample consisted of an irregular roundish shape particles. The crystal had the La-rich surface. La_2O_3 was deposited on the CTO:La for the samples doped with more than 5 mol% of La. The Pt-loaded $CaTiO_3$ doped with 5mol% of La showed the best performance and 36 µmol h^{-1} of H_2 was evolved. The H_2 production rate was enhanced by 15 times than non-doped one. Electronic state of Pt-cocatalyst loaded on the sample was slightly negative than that on non-doped one. The high surface La concentration of CTO:La, deposited La_2O_3 species on CTO:La, and the different electronic states of Pt cocatalyst would synergistically contributed to the enhancement of the photocatalytic activity.

Reference

[1] J. W. Erisman, M. A. Sutton, J. Galloway, Z. Klimont, W. Winiwarter, *Nat. Geosci.* **2008**, *1*, 636–639.

[2] M. Behrens, F. Studt, I. Kasatkin, S. Kühl, M. Hävecker, F. Abild-pedersen, S. Zander, F. Girgsdies, P. Kurr, B. Kniep, et al., *Science (80-.).* **2012**, *336*, 893–898.

[3] H. M. Torres Galvis, K. P. De Jong, *ACS Catal.* **2013**, *3*, 2130–2149.

[4] D. Das, T. N. Veziroglu, *Int. J. Hydrogen Energy* **2001**, *26*, 13–28.

[5] L. Barelli, G. Bidini, F. Gallorini, S. Servili, *Energy* **2008**, *33*, 554–570.

[6] A. Anzai, K. Fujiwara, A. Yamamoto, H. Yoshida, *Catal. Today* **2020**, *352*, 1–9.

[7] K. Shimura, H. Miyanaga, H. Yoshida, *Stud. Surf. Sci. Catal.* **2010**, *175*, 85–92.

[8] H. Onishi, *ChemSusChem* **2019**, *12*, 1825–1834.

[9] U. Holzwarth, N. Gibson, *Nat. Nanotechnol.* **2011**, *6*, 534–534.

[10] M. Nomura, Y. Koike, M. Sato, A. Koyama, Y. Inada, K. Asakura, *AIP Conf. Proc.* **2007**, *882*, 896–898.

[11] A. Yamamoto, S. Mizuba, Y. Saeki, H. Yoshida, *Appl. Catal. A Gen.* **2016**, *521*, 125–132.

[12] H. Yoshida, S. Mizuba, A. Yamamoto, *Catal. Today* **2019**, *334*, 30–36.

[13] A. Fu, X. Chen, L. Tong, D. Wang, L. Liu, J. Ye, *ACS Appl. Mater. Interfaces* **2019**, *11*, 24154–24163.

[14] S. Bai, C. Wang, M. Deng, M. Gong, Y. Bai, J. Jiang, Y. Xiong, **2014**, *201406468*, 12120–12124.

Summary

In the study described in this dissertation, the $CaTiO_3$-based photocatalysts that can be used for the photocatalytic reduction of CO_2 with water and the photocatalytic steam reforming of methane were investigated.

In Chapter 1, the Ag-loaded $CaTiO_3$ photocatalyst was reexamined by optimizing the Ag loading amount and using a inner irradiation photochemical flow reactor for the photocatalytic reduction of CO_2 with water. The results showed that the Ag-loaded $CaTiO_3$ photocatalyst successfully promoted the photocatalytic reduction of CO_2 with water with a very high CO selectivity (94%), and suppressed H_2 production by water splitting, which is a competitive reaction. It was shown that the low reaction temperature and CO_2 bubbling into aqueous solutions to obtain a high concentration of dissolved CO_2 in the aqueous solution was very effective in achieving a high photocatalytic activity.

In Chapter 2, the preparation conditions of the $CaTiO_3$ photocatalyst for the photocatalytic reduction of CO_2 with water over Ag-loaded $CaTiO_3$ are discussed. We found that the $CaTiO_3$ microcrystals with polyhedral shapes prepared by a flux method using NaCl flux exhibited the highest photocatalytic activity. For the sample prepared by a flux method using NaCl, a shift of the diffraction line to a higher angle was observed in the powder X-ray diffraction pattern and a new A_{1g} mode was observed in the Raman spectrum. Characteristic absorption bands related to oxygen vacancies were observed in the diffuse reflectance UV–Vis spectra. It was suggested that the Al^{3+} ions from the alumina crucible partially substituted Ti^{4+} ions at B sites in $CaTiO_3$ with the formation of oxygen vacancies, which would contribute to the development of the $CaTiO_3$ photocatalysts.

In Chapter 3, alkaline earth metal oxides were loaded to the $CaTiO_3$ prepared by a solid state reaction method. Ag cocatalyst was loaded to the alkaline earth metal oxides modified samples by photodeposition under the reaction conditions. The modification by the alkaline earth metal oxides enhanced the photocatalytic activity for the photocatalytic reduction of CO_2 with water. The sample modified with MgO exhibited more than 2 times higher photocatalytic activity than the non-modified sample. TEM-EDX observation of the sample modified with MgO, which showed the highest photocatalytic activity, revealed that the silver nanoparticles dispersed on the calcium titanate were covered by a thin layer of magnesium species.

In Chapter 4, the effect of the particle size of $CaTiO_3$ on the photocatalytic activity for the reduction of CO_2 with water was investigated to three samples: the sample with a particle size of 100 nm, 300 nm, and 800 nm. The results showed that the sample with a particle size of 100 nm, which had the highest specific surface area, gave the highest CO production rate. The CO production rate decreased as the specific surface area decreased. The samples with a large specific surface area tended to show high CO production rate.

In Chapter 5, Pt-loaded calcium titanate ($Pt/CaTiO_3$) photocatalysts prepared by a flux method with various parameters, such as the selection of the flux, presence or absence of the flux, and solute concentration in the molten mixture with the flux, were investigated. The photocatalytic performance of the samples was evaluated by the photocatalytic steam reforming of methane at mild temperature (c.a. 323 K) under ambient pressure. The highest photocatalytic activity was obtained when the sample was prepared by a flux method at 1373 K for 10 hours using KCl at a ratio of 50% as a flux, and 0.05 wt% of Pt cocatalyst was loaded to the sample. The sample prepared by the flux method using KCl as a flux showed 3.3 times higher photocatalytic activity than that by a solid state reaction method. In order to further increase the activity, La was doped into the Ca^{2+} site in $CaTiO_3$. A small amount of La, such as about 0.5 mol% induced crystal growth. On the other hand, further amount of La suppressed crystal growth by increasing the amount of La. The addition of La increased the photocatalytic activity, and the sample doped with a moderate amount of La, such as about 1 mol% showed the highest photocatalytic activity. Although many of the structural properties, such as crystal morphology, grain size, and specific surface area, could not simply explain the increase in photocatalytic activity, it was shown that oxygen vacancies, which gave an absorption band in the visible light region at least, decreased the photocatalytic activity.

In Chapter 6, La doped $CaTiO_3$ photocatalysts prepared by a solid state reaction method with different La contents were investigated for the photocatalytic steam reforming of methane. With increasing La content, the added La was not completely doped into the $CaTiO_3$, but partially deposited as La_2O_3. Furthermore, it was found that the added La was abundantly present on the $CaTiO_3$ surface. The addition of La increased the hydrogen production rate. The sample doped with 5 mol% of La showed the highest photocatalytic activity, 15 times higher photocatalytic activity than the sample without La, and 2 times higher activity than the La-doped $CaTiO_3$ prepared by the flux method, which was optimized in Chapter 5. It was proposed that the high surface La concentration of the La-doped $CaTiO_3$ and the La_2O_3 deposited on the surface of $CaTiO_3$ would contribute to the high photocatalytic activity.

In summary, the $CaTiO_3$-based photocatalysts exhibited good performance for the photocatalytic reduction of CO_2 with water and photocatalytic steam reforming of methane under mild condition. The reasonable explanation of the relationship between the structure and photocatalytic activity was given. These findings are believed to contribute to the development of highly active $CaTiO_3$-based photocatalysts for endergonic reaction in the future.

Appendix

Ag loaded $BaTi_4O_9$ photocatalyst for highly selective photocatalytic CO_2 reduction with water

Abstract

The photocatalytic reduction of CO_2 with water to high-valuable chemicals has been getting attention as an artificial photosynthetic system to convert CO_2 into energy. Here we reported Ag cocatalyst loaded $BaTi_4O_9$ photocatalyst (Ag/$BaTi_4O_9$) as one of the most selective photocatalysts for reduction of CO_2 to CO by water. The Ag/$BaTi_4O_9$ showed an excellent selectivity towards CO (>98%).

Introduction

Photocatalytic reduction of CO_2 to valuable chemicals over semiconductor photocatalyst have been studied one of the artificial photosynthesis technologies.[1][2] Photocatalytic reduction of CO_2 is expected to solve both energy and environmental problems simultaneously. CO_2 is the most oxidaized carbon compound. We need to reduce it to convert useful chemicals. Photocatalytic reduction of CO_2 requires a reducing agent. H_2O is an ideal electron source for CO_2 reduction in photocatalysis because H_2O is nontoxic, earth-abundant, and stable. However, when the photocatalytic reduction of CO_2 is carried with H_2O, the photogenetated electrons tend to reduce H^+ instead of CO_2 and then to form H_2 preferentially because of thermodynamic requirement. Therefore, in order to realize the efficient photocatalytic reduction of CO_2 using H_2O as an electron donor, it is necessary to design a catalyst that can reduce CO_2 selectively despite coexistence of H^+ in water.

Iizuka et al. reported that Ag nanoparticles loaded on $BaLa_4Ti_4O_{15}$ photocatalyst acted as an efficient cocatalyst in the photocatalytic reduction of CO_2 to CO using H_2O as an electron source. Afterwards, many kinds of Ag-loaded semiconductor photocatalysts for photocatalytic reduction of CO_2 to CO with water as an electron donor have been reported.[3][4][5][6][7][8][9][10][11][12][13][14][15][16][17][18][19][20]

We have also reported some type of Ag-loaded photocatalysts, namely Ag/$CaTiO_3$,[21][22] Ag/$Na_2Ti_6O_{13}$,[23] Ag-Mn/$K_2Ti_6O_{13}$.[24][25] These titanate semiconductor materials have a band gap of about 3.5−3.6 eV and a distortion with a TiO_6 octahedra in common. These should be one of important factors to achieve CO_2 reduction in water with high CO selectivity. Barium tetratitanate, $BaTi_4O_9$ (BTO), is a semiconductor with band gap of 3.57 eV,[26] which is similar to the titanate as mentioned above. $BaTi_4O_9$ is a photocatalyst with a pentagonal prism tunnel structure.[27] $BaTi_4O_9$ has two kinds of TiO_6 octahedra, both of which are so heavily distorted that they have dipole moments.[28] The local internal fields due to the dipole moment are considered to be advantageous for boosting electron-hole separation upon photoexcitation.[29] Moreover, Inoue et al. proposed that concave sites on the BTO surface derived from the tunnel structure help stabilize the cocatalyst nanoparticles.[27] Therefore, it is expected that the unique surface structure would help to prevent Ag cocatalyst nanoparticles from aggregating and growing into larger particles on BTO to some extent. These characters would be suitable for CO_2 reduction. In this study, we focused on Ag cocatalyst loaded BTO as a photocatalyst for the conversion of CO_2 in aqueous solution for the first time. Effect of Ag loading method on the photocatalytic activity was also discussed.

Experimental

Preparation of photocatalysts

$BaTi_4O_9$ photocatalyst was synthesized by a conventional solid-state reaction method. The starting materials, $BaCO_3$ (FUJIFILM Wako Pure Chemical, 99.9%) and TiO_2 (rutile, Kojundo, 99.9%), were mixed in an alumina mortar in the presence of ethanol. The mixture with the Ba/Ti ratio = 1/4 was heated in an aluminum crucible covered by a lid at a rate of 10 K min^{-1} to 1273 K in an electric muffle furnace, and held at this temperature for 10 h, followed by natural cooling to room temperature in the furnace.

Loading Ag cocatalyst

The fabricated photocatalysts were modified with *x* wt% of a Ag cocatalyst by a impregnation (IMP) method, a photodeposition (PD) method, or a chemical reduction (CR) method.

In the IMP method, the synthesized $BaTi_4O_9$ sample (0.5 g) was dispersed into 40 mL of an aqueous solution including a required amount of $AgNO_3$ (Nacalai tesque, 99.8%). The suspension was magnetically stirred and dried up at 353 K, followed by calcination in an electric muffle furnace at 723 K for 2 h in an air atmosphere.

The Ag loading by the PD method was carried out in an inner-irradiation photochemical reactor, where 0.5 g of sample was dispersed in 350 mL of ion-exchanged water and an aqueous solution of $AgNO_3$ (0.5 mol L^{-1}, 93.6 μL) was added to the suspension. After Ar gas was bubbled into the suspension at a flow rate of 30 mL min^{-1} for 1.0 h, the suspension was irradiated using a 100 W high-pressure Hg lamp with a quartz jacket connected to a water-cooling system with the bubbling flow of Ar. Subsequently, the obtained powder was filtrated with suction filtration, and dried at ambient temperature in air.

In the CR method, an aqueous $AgNO_3$ solution (0.5 mol L^{-1}, 93.6 μL) was added to 50 mL of an aqueous suspension containing 0.5 g of the photocatalyst. After addition of an equimolar amount of an aqueous $NaPH_2O_2$ solution (0.5 mol L^{-1}, 93.6 μL) with respect to Ag^+ to the suspension, the mixture was stirred at 333 K for 1 h. The obtained powder was rinsed by 1 L of ion-exchanged water, filtered by a suction filtration, and dried at ambient temperature in air.

The Ag-loaded $BaTi_4O_9$ samples are referred to as Ag/$BaTi_4O_9$_IMP, Ag/$BaTi_4O_9$_PD, and Ag/$BaTi_4O_9$_CR. The typical loading amount of Ag was 1.0 wt%. The obtained samples loaded with *x* mol% of Ag co-catalyst are referred to as Ag(*x*)/$BaTi_4O_9$, e.g., Ag(1)/$BaTi_4O_9$.

Characterization of photocatalysts

X-ray diffraction (XRD) measurement was carried out at room temperature with a Shimadzu Lab X XRD-6000 using Cu Kα radiation (40 kV, 30 mA). The crystallite size of Ag nanoparticle was determined by Scherrer equation using the full width at half maximum (FWHM) of the diffraction line at 2θ=38.1° in the XRD patterns of Ag. Images of scanning electron microscopy (SEM) was taken by a JEOL JSM-890. Diffuse reflectance (DR) UV-visible spectrum was recorded on a JASCO V-670 equipped with an integrating sphere covered with a $BaSO_4$ reference. The band gap was estimated from the spectrum according to Tauc plot.[15] The BET specific surface area was estimated from the amount of N_2 adsorption at 77 K, which was measured using a Quantachrome Monosorb MS-21.

Photocatalytic reaction tests

The reaction tests for photocatalytic reduction of CO_2 with water were carried out in the inner-irradiation photochemical reactor mentioned above, as described in our previous study.[8] The photocatalyst powder of 0.3 g was dispersed in 350 mL of an aqueous $NaHCO_3$ solution (0.5 mol L^{-1}), where bicarbonate ions (HCO_3^-) worked as a buffer (pH=ca. 9) to enrich molecular CO_2 in the solution.[16] The photocatalyst was suspended with magnetically stirring in a bubbling flow of gaseous CO_2 at a flow rate of 30 mL min^{-1} for 2 h in the dark, and then the lamp was switched on to start the photocatalytic reaction. The gaseous products were sampled by a six-way valve and analyzed by an online gas chromatograph with a thermal conductivity detector (Shimadzu, GC-8A, Shincarbon ST, Ar carrier). The CO selectivity, S_{CO} (%), can be calculated as follows (eq. 1), where the production rate of CO, H_2 and O_2 are referred to as R_{CO}, R_{H2} and R_{O2}, respectively. The ratio of the consumed electron and hole for products formation, $R(e^-/h^+)$, can be calculated as follows (eq. 2).

$$S_{CO}\ (\%) = R_{CO} / (R_{CO} + R_{H2}) \times 100 \quad (1)$$

$$R(e^-/h^+) = (R_{CO} + R_{H2}) / 2\ R_{O2} \quad (2)$$

Results and Discussion

$BaTi_4O_9$ photocatalyst was prepared by a conventional solid state reaction at 1273 K for 20 h. Figure 1 shows the XRD patterns of the pristine $BaTi_4O_9$ sample. The obtained sample was identified to have a single phase with a space group *Pmmn* structure (Fig. 1A).[18] Figure 2 shows the diffuse reflectancce UV-Vis spectrum of the pristine $BaTi_4O_9$ sample. The $BaTi_4O_9$ samples an adsorption band at wavelengths shorter than 350 nm, which corresponds to a bandgap of 3.54 eV (Figure. 2). Figure 3 shows SEM image of the pristine $BaTi_4O_9$ sample. The sample consisted of roundish irregular shaped particles with c.a. 500 nm in diameter. The specific BET surface area (S_{BET}) was 3.63 $m^2\ g^{-1}$. The average particle diameter (D) estimated from the BET surface area and the density (ρ= 4.18 g/cm^3)[19] using an equation $D=6/(S_{BET}\times\rho)$ for spherical-shaped particles was 395 nm, which was almost consistent with the obsrvation in SEM images. Figure 4 shows time courses of the production rates in the photocatalytic reduction of CO_2 with water over the $BaTi_4O_9$ sample. Only H_2 and O_2 were evolved, that is, overall water spllitting reaction occured although CO_2 reduction did not occur despite under CO_2 flow. This result was supported the fact overall water splitting over $BaTi_4O_9$ has been investigated so far. [13][20][21][22][23][12][24]

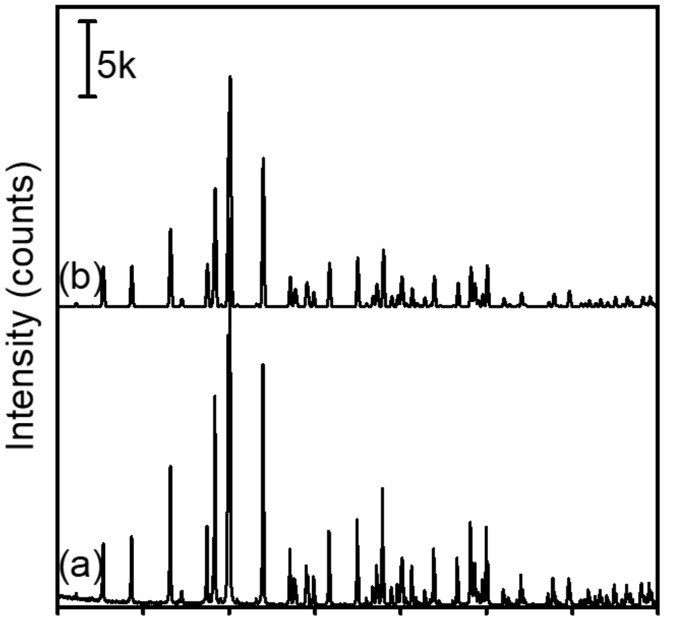

Figure 1. XRD patterns (upper left) of (a) the $BaTi_4O_9$ sample prepared by solid state method, (b) ICSD collCode#31783[18] as a reference of $BaTi_4O_9$.

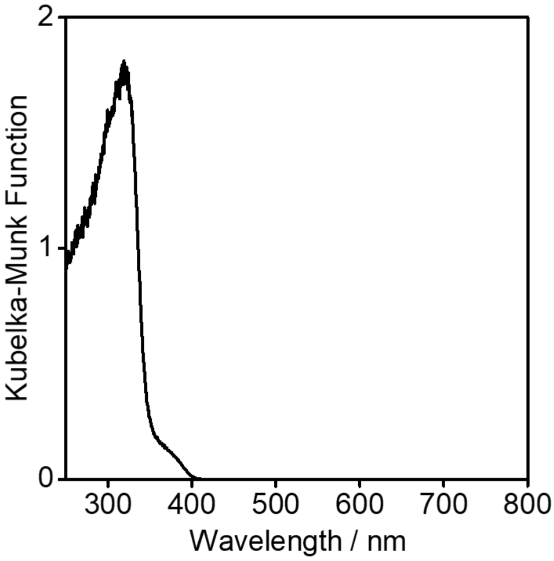

Figure 2. Diffuse reflectance UV-Vis spectrum of the $BaTi_4O_9$ sample.

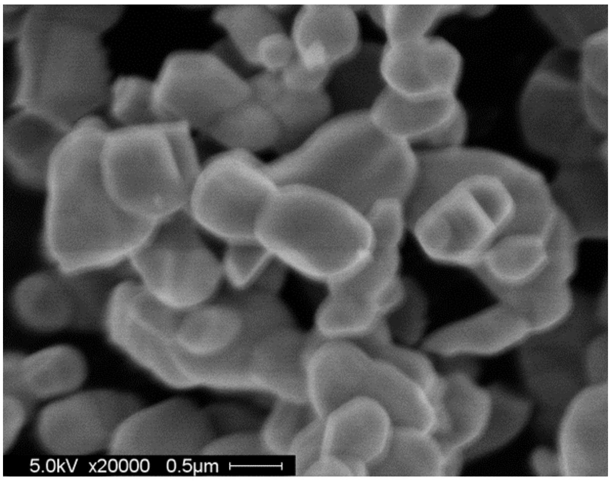

Figure 3. SEM image of the $BaTi_4O_9$ sample.

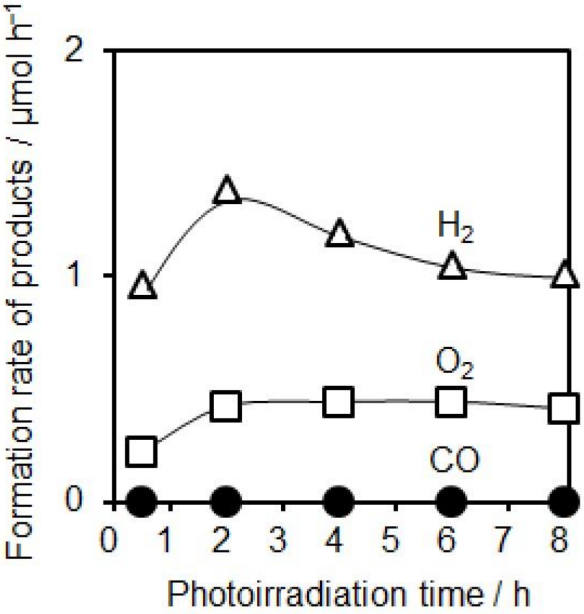

Figure 4. Time courses of the production rates of CO (circle), H_2 (triangle), and O_2 (square) in the photocatalytic reduction of CO_2 with water over the $BaTi_4O_9$ sample.

The fabricated photocatalysts were modified with x wt% of a Ag cocatalyst was loaded on the $BaTi_4O_9$ sample by three methods, a photodeposition (PD) method, a impregnation (IMP) method, or a chemical reduction (CR) method. Figure 5 shows the time course of the production rates in the photocatalytic reaction test for CO_2 reduction in aqueous $NaHCO_3$ solution with the Ag(1wt%)/$BaTi_4O_9$_IMP sample. The photocatalytic reaction test was carried out using a conventional inner irradiation photochemical reactor equipped with a 100 W high pressure mercury lamp. As the reduction products CO and H_2 were evolved, where CO was the predominant product and H_2 was a very minor product. The stoichiometric evolution of O_2 was also observed as an oxidative product. The CO fomation rate gradually decreased with time and close to steady state after 8 h photoirradiation. The formation rates of CO, H_2, and O_2 at 8 hours after the start of the photoirradiation were 6.0, 2.6, and 0.084 µmol h^{-1}, respectively. The selectivity of CO in the reduction product was $S_{CO}(\%)=98\%$.

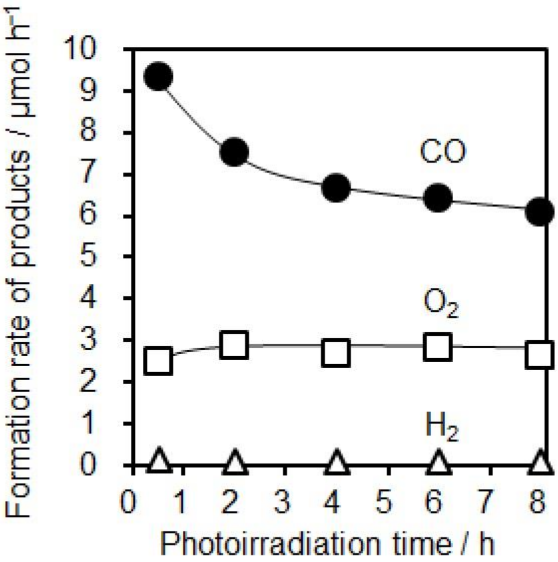

Figure 5. Time courses of the production rates of CO (circle), H_2 (triangle), and O_2 (square) in the photocatalytic reduction of CO_2 with water over the Ag(1 wt%)/$BaTi_4O_9$_IMP sample. 0.3 g of catalyst. Reactions were performed in 0.5 M $NaHCO_3$ aqueous solution (350 mL) with illumination from a high-pressure mercury lamp (100 W).

The ratio of consumed electrons and holes was almost unity, $R(e^-/h^+)=1.1$. This suggests that the photocatalytic CO_2 reduction into CO and O_2 proceeded using water as a reducing agent following eq. 5, which is obtained from eq. 3 and eq. 4.

$$CO_2 + 2\,H^+ + 2\,e^- \rightarrow CO + H_2O \tag{3}$$

$$H_2O + 2\,h^+ \rightarrow 1/2\,O_2 + 2\,H^+ \tag{4}$$

$$CO_2 \rightarrow CO + 1/2\,O_2 \tag{5}$$

Figure 6 shows the production rates measured at 8 h later from the start of the reaction test with the $BaTi_4O_9$ photocatalyst samples on which the Ag cocatalyst was loaded by the different methods, photodeposition (PD) method, chemical reduction (CR) method, and an impregnation (IMP) method. All samples modified Ag cocatalyst generated CO with an excellent selectivity beyond 98% regardless of the loading method. The IMP method was the most effective loading method to give a high CO formation rate.

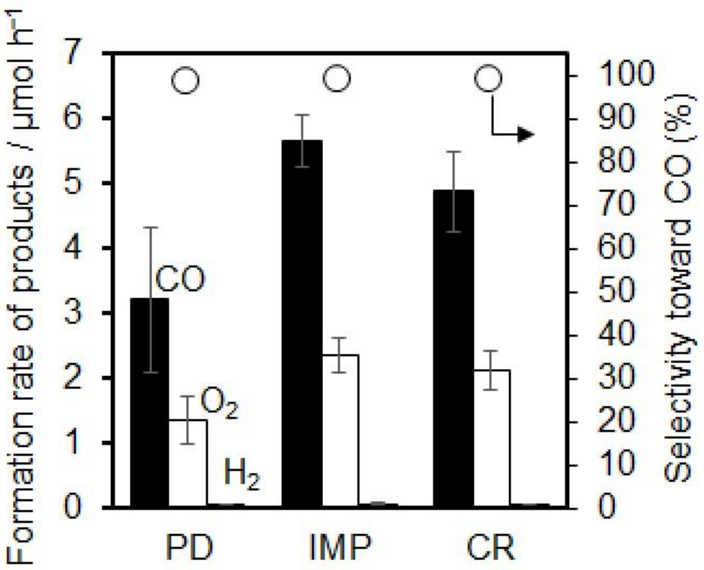

Figure 6. Formation rates of CO (black), O_2 (white), H_2 (gray), and selectivity toward CO evolution (circle) for the photocatalytic reduction of CO_2 in aqueous $NaHCO_3$ solution using $BaTi_4O_9$ photocatalyst modified with Ag cocatalyst via photodeposition method (PD), impregnation method (IMP), and the chemical reduction (CR) method. 0.3 g of catalyst. Ag loading amounts were 1 wt%. Reactions were performed in 0.5 M $NaHCO_3$ aqueous solution (350 mL) with illumination from a high-pressure mercury lamp (100 W).

Figure 7 shows the formation rates of products during photocatalytic CO_2 reduction in aqueous $NaHCO_3$ solution with the Ag(*x*)/$BaTi_4O_9$_IMP photocatalysts of various Ag loading amount (*x* wt%). With the pristine Ag(0 wt%)/$BaTi_4O_9$_IMP sample, only the photocatalytic overall water splitting reaction proceeded and no CO_2 reduction reaction as mentioned above. On the other hand, the CO_2 reduction reaction predominantly proceeded at any loading amounts of the Ag cocatalyst on the $BaTi_4O_9$ photocatalyst. The CO formation rate was improved with increasing the Ag loading amout until 0.2 wt%. The optimum amount of the Ag cocatalyst for the CO_2 reduction was in the range of 0.2–1 wt%, and the photocatalytic activity reached to 5.7 µmol h^{-1} for CO, and 2.4 µmol/h for O_2 evolution, respectively on the Ag(1 wt%)/$BaTi_4O_9$ photocatalyst. The photocatalytic activity gradually decreased with increasing the amount of Ag more than 1 wt%. (Results in the photocatalytic reaction tests with other photocatalysts are listed in Table 1)

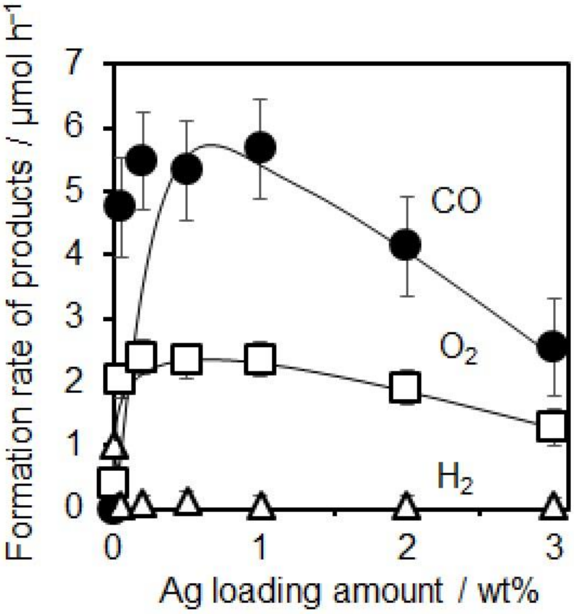

Figure 7. Formation rates of CO (circle), H_2 (triangle), and O_2 (square) after 8 h photoirradiation over various Ag(*x*)/$BaTi_4O_9$_IMP photocatalysts with different loading amount of Ag cocatalyst. 0.3 g of catalyst. Reactions were performed in 0.5 M $NaHCO_3$ aqueous solution (350 mL) with illumination from a high-pressure mercury lamp (100 W).

Table 1. Results in the photocatalytic reaction tests with various $BaTi_4O_9$ photocatalyst samples Effect of loading amount and loading method of Ag cocatalyst on the photocatalytic activity for CO_2 reduction over.[a]

	Formation rate of products / μmol h^{-1}			
Sample	CO[b]	O_2[c]	H_2	Selectivity towards CO (%)
$BaTi_4O_9$	n.d.	0.41	1.0	0
Ag(1)/$BaTi_4O_9$_PD[b]	3.2	1.4	0.052	98
Ag(0.05)/$BaTi_4O_9$_IMP[c]	4.7	2.0	0.064	99
Ag(0.2)/$BaTi_4O_9$_IMP[c]	5.5	2.4	0.080	99
Ag(0. 5)/$BaTi_4O_9$_IMP[c]	5.3	2.3	0.13	98
Ag(1)/$BaTi_4O_9$_IMP[c]	5.7	2.4	0.068	99
Ag(2)/$BaTi_4O_9$_IMP[c]	4.1	1.9	0.071	98
Ag(3)/$BaTi_4O_9$_IMP[c]	2.5	1.3	0.055	98
Ag(1)/$BaTi_4O_9$_CR[d]	4.9	2.1	0.053	99
Ag(2)/$BaTi_4O_9$_CR[d]	4.6	2.0	0.048	99
Ag(3)/$BaTi_4O_9$_CR[d]	5.5	2.2	0.046	99

[a] Catalyst 0.3 g, 350 mL of 0.5 M aqueous $NaHCO_3$ solution, CO_2 flow system (30 mL min^{-1}), a 100 W high-pressure mercury lamp, an inner irradiation quartz cell. [b] photoirradiated under Ar atmosphere. [c] calcined at 723 K for 2 h. [d] $NaPH_2O_2$ as a reducing reagent.

Figure 8 shows the SEM images of Ag cocatalyst-loaded $BaTi_4O_9$ photocatalysts. $BaTi_4O_9$ had a irregular round shape with a size of several hundred nanometers, as mentioned above. Ag cocatalysts deposited by the PD method were nanoparticles (NPs) with the size of 60 nm, which were observed similarly even after the photocatalytic reaction test. Aggregated Ag NPs were observed for Ag cocatalysts deposited by the IMP method. The observed size of the Ag NPs loaded by an IMP method before reaction was c.a. 100 nm, while Ag NPs with the size of 20−60 nm were dispersed after the photocatalytic reaction tests. Ag NPs were particularly concentrated in some areas, and in other areas the number of Ag were small. This suggested that the $BaTi_4O_9$ particle crystal was surrounded by hole-transferred site and electron-transferred site. Ag on the hole-transferred, where many holes available, were oxidized by photogenerated holes and dissolved into the solution and photodeposited again on the electron-transferred site during the photocatalytic reaction by the photogenerated electrons. The Ag cocatalysts on the sample prepared by the CR method were not observed in the SEM images before reaction, while fine Ag NPs with the size less than 20 nm were observed after the photocatalytic reaction tests. As well as IMP method, Ag NPs were particularly concentrated in some areas. Figure 9 and 10 shows the XRD patterns of Ag cocatalyst-loaded $BaTi_4O_9$ photocatalysts before and after reaction, respectively. The average crystallite size of Ag deposited by PD method, which was calculated from the Ag(111) diffraction line at 38.1° was 32 nm before reaction. The size after reaction was almost the same (31 nm). The size of Ag deposited by IMP method was 62 nm. The size of Ag deposited by IMP method decreased 51 nm after reaction. The diffraction line due to Ag(111) was not observed for Ag deposited by CR method both before and after reaction. This means that Ag deposited by CR method were highly dispersively loaded on the photocatalyst. These tendency were almost consistent with the obsrvation in SEM images. Figure 11 and 12 shows diffuse reflectance UV-Vis spectra of Ag cocatalyst-loaded $BaTi_4O_9$ photocatalysts before and after reaction, respectively. All samples had bands due to band transition in the UV range (250−400 nm) and localized surface plasmon resonance of Ag NPs. Ag deposited by PD method had a spectral peak centered at 500 nm with a shoulder band centered at 383 nm. Ag deposited by IMP method had a spectral peak centered at 582 nm. Ag deposited by CR method had a spectral peak centered at 516 nm with a shoulder band centered at 383 nm. After reaction the spectral peak shifted to around 470 nm. All samples after reaction showed similar spectra. this means that the state of Ag after the reaction is similar. This would be the reason for almost the same CO selectivity in every samples(98%<).

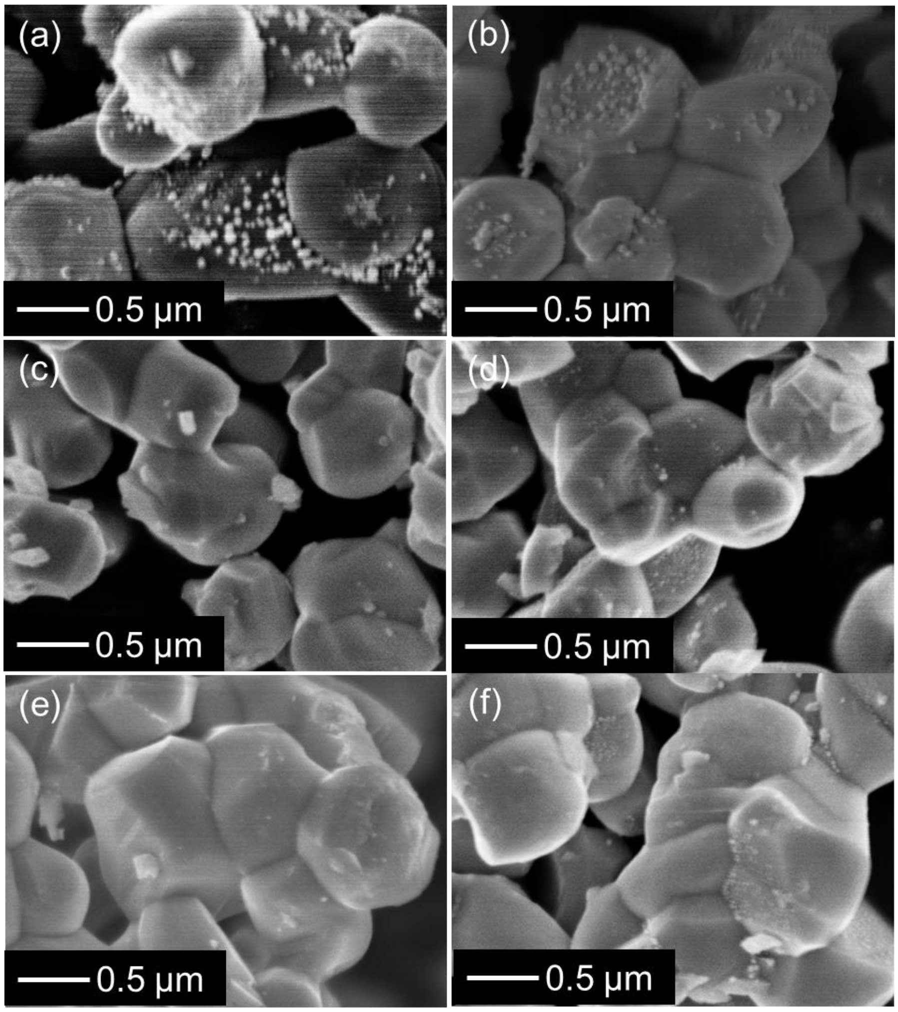

Figure 8. SEM images of the Ag(1 wt%)/$BaTi_4O_9$ samples prepared by the PD method (a) as prepared and (b) after the photocatalytic reaction test for 8 h, the IMP method (c) as prepared and (d) after the photocatalytic reaction test for 8 h, and the CR method (e) as prepared and (f) after the photocatalytic reaction test for 8 h.

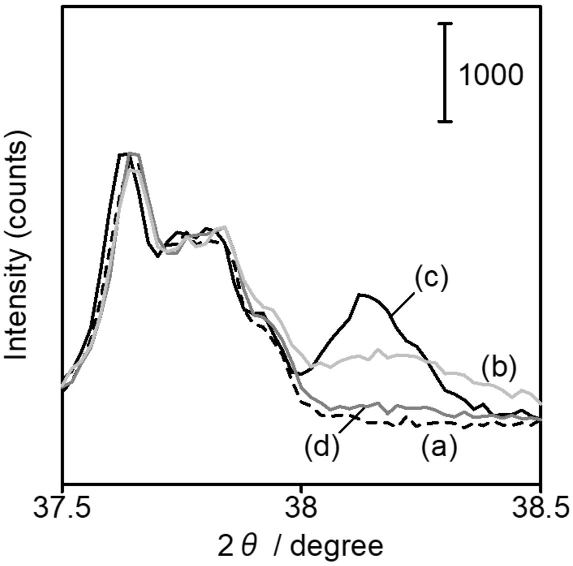

Figure 9. XRD patterns of (a) the pristine $BaTi_4O_9$ sample, (b) the Ag(1 wt%)/$BaTi_4O_9$_PD sample, (c) the Ag(1 wt%)/$BaTi_4O_9$_IMP sample, and (d) the Ag(1 wt%)/$BaTi_4O_9$_CR sample, before photocatalytic CO_2 reduction reaction.

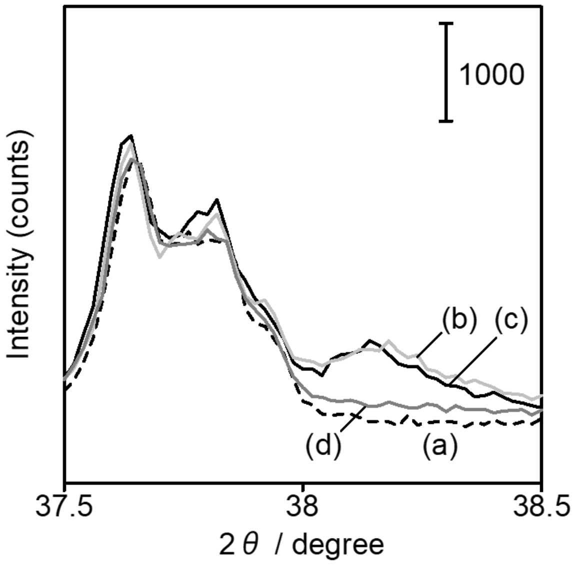

Figure 10. XRD patterns of (a) the pristine $BaTi_4O_9$ sample, (b) the Ag(1 wt%)/$BaTi_4O_9$_PD sample, (c) the Ag(1 wt%)/$BaTi_4O_9$_IMP sample, and (d) the Ag(1 wt%)/$BaTi_4O_9$_CR sample, after photocatalytic CO_2 reduction reaction.

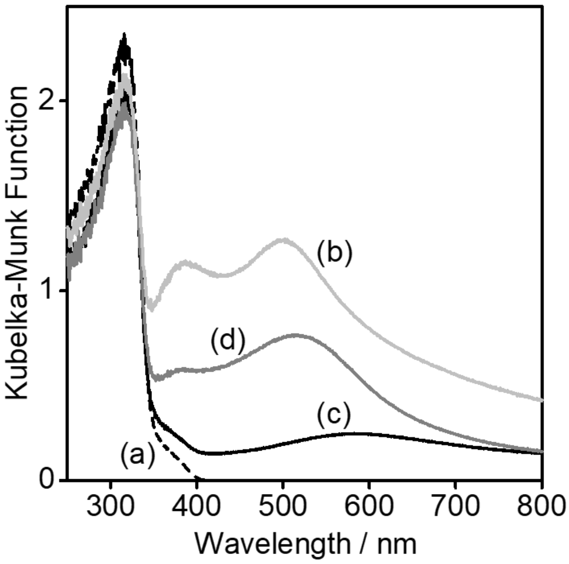

Figure 11. Diffuse reflectance UV-Vis spectra of (a) the pristine $BaTi_4O_9$ sample, (b) the Ag(1 wt%)/$BaTi_4O_9$_PD sample, (c) the Ag(1 wt%)/$BaTi_4O_9$_IMP sample, and (d) the Ag(1 wt%)/$BaTi_4O_9$_CR sample, before photocatalytic CO_2 reduction reaction.

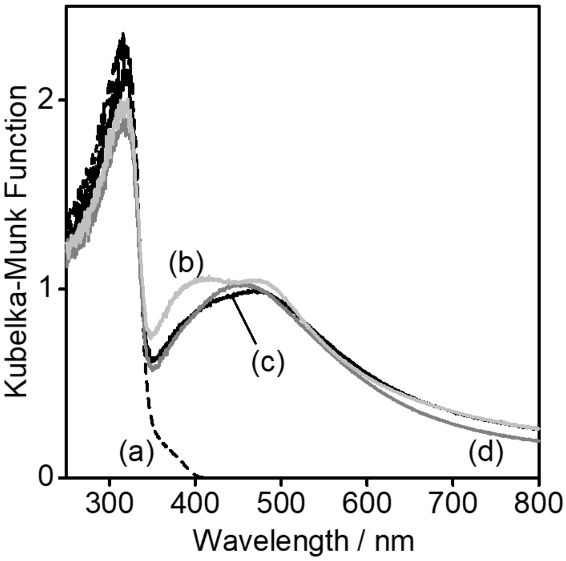

Figure 12. Diffuse reflectance UV-Vis spectra of (a) the pristine $BaTi_4O_9$ sample, (b) the Ag(1 wt%)/$BaTi_4O_9$_PD sample, (c) the Ag(1 wt%)/$BaTi_4O_9$_IMP sample, and (d) the Ag(1 wt%)/$BaTi_4O_9$_CR sample, after photocatalytic CO_2 reduction reaction.

Conclusion

In summary, $BaTi_4O_9$ photocatalyst was prepared by a solid-state reaction method and modified with Ag cocatalyst for the photocatalytic reduction of CO_2. As a result, we found that the Ag-loaded $BaTi_4O_9$ crystals is one of the most selective photocatalysts for the photocatalytic CO_2 reduction to CO and O_2 in an aqueous $NaHCO_3$ solution. The selectivity for the CO_2 reduction to CO reached 98%, where the water splitting to produce H_2 was almost completely suppressed even though the redox potential for H_2 formation is obviously higher than that for the CO formation. Ag loading method and loading amount affected the photocatalytic activity. The impregnation method was most effective to give a high CO formation rate.

References

[1] T. Inoue, A. Fujishima, S. Konishi, *Nature* **1979**, *277*, 637.

[2] O. Ishitani|, C. Inoue, Y. Suzuki, T. Ibusuki, *J. Photochem. Photobiol. A Chem.* **1993**, *72*, 269–271.

[3] K. Sayama, H. Arakawa, *J. Phys. Chem.* **1993**, *97*, 531–533.

[4] Y. Hori, H. Wakebe, T. Tsukamoto, O. Koga, *Electrochim. Acta* **1994**, *39*, 1833–1839.

[5] M. Azuma, K. Hashimoto, M. Hiramoto, M. Watanabe, T. Sakata, *J. Electrochem. Soc.* **2019**, *137*, 1772–1778.

[6] K. P. Kuhl, T. Hatsukade, E. R. Cave, D. N. Abram, J. Kibsgaard, T. F. Jaramillo, *J. Am. Chem. Soc.* **2014**, *136*, 14107–14113.

[7] H. Yoshida, L. Zhang, M. Sato, T. Morikawa, T. Kajino, T. Sekito, S. Matsumoto, H. Hirata, *Catal. Today* **2015**, *251*, 132–139.

[8] A. Anzai, N. Fukuo, A. Yamamoto, H. Yoshida, *Catal. Commun.* **2017**, *100*, 134–138.

[9] X. Zhu, A. Anzai, A. Yamamoto, H. Yoshida, *Appl. Catal. B Environ.* **2019**, *243*, 47–56.

[10] X. Zhu, A. Yamamoto, S. Imai, A. Tanaka, H. Kominami, H. Yoshida, *Chem. Commun.* **2019**, *55*, 13514–13517.

[11] X. Zhu, A. Yamamoto, S. Imai, A. Tanaka, H. Kominami, *Appl. Catal. B Environ.* **2020**, *274*, 119085.

[12] Y. Yamashita, K. Yoshida, **1999**, 61–66.

[13] Y. Inoue, Y. Asai, K. Sato, *J. Chem. Soc. Faraday Trans.* **1994**, *90*, 797–802.

[14] J. Sato, H. Kobayashi, Y. Inoue, **2003**, *4*, 7970–7975.

[15] J. Tauc, R. Grigorovici, A. Vancu, *Phys. Status Solidi* **1966**, *15*, 627–637.

[16] K. Teramura, K. Hori, Y. Terao, Z. Huang, S. Iguchi, Z. Wang, H. Asakura, S. Hosokawa, T. Tanaka, *J. Phys. Chem. C* **2017**, *121*, 8711–8721.

[17] Z. Huang, K. Teramura, S. Hosokawa, T. Tanaka, *Appl. Catal. B Environ.* **2016**, *199*, 272–281.

[18] D. H. Templeton, C. H. Dauben, *J. Chem. Phys.* **1960**, *32*, 1515–1518.

[19] Y. C. Liou, C. T. Wu, K. H. Tseng, T. C. Chung, *Mater. Res. Bull.* **2005**, *40*, 1483–1489.

[20] M. Kohno, T. Kaneko, S. Ogura, K. Sato, Y. Inoue, *J. Chem. Soc. - Faraday Trans.* **1998**, *94*, 89–94.

[21] M. Kohno, S. Ogura, Y. Inoue, *J. Mater. Chem.* **1996**, *6*, 1921–1924.

[22] S. Ogura, K. Sato, Y. Inoue, **2000**, 2449–2454.

[23] M. Kakihana, **2019**, *2053*, 2–5.

[24] Y. Hiramachi, H. Fujimori, A. Yamakata, Y. Sakata, *ChemCatChem* **2019**, *11*, 6213–6217.

[25] J. J. Mock, M. Barbic, D. R. Smith, D. A. Schultz, S. Schultz, *J. Chem. Phys.* **2002**, *116*, 6755–6759.

List of Publications

Chapter 1

Akihiko Anzai, Naoto Fukuo, Akira Yamamoto, Hisao Yoshida, Highly selective photocatalytic reduction of carbon dioxide with water over silver-loaded calcium titanate, Catalysis Communications, 100 (2017) 134‑138.

Chapter 5

Akihiko Anzai, Kenji Fujiwara, Akira Yamamoto, Hisao Yoshida, Platinum-loaded lanthanum-doped calcium titanate photocatalysts prepared by a flux method for photocatalytic steam reforming of methane, *Catal. Today*, 352 (2020) 1-9.

Acknowledgements

The studies presented in this thesis were performed at the Graduate School of Human and Environmental studies, Kyoto University, Japan from 2016 to 2021 under the supervision of Prof. Hisao Yoshida.

The author expressed my sincere gratitude to my supervisor, Prof. Hisao Yoshida for his exact guidance, insightful suggestions, kind encouragement, and valuable comments, throughout this study. The author expressed my great appreciation to Dr. Akira Yamamoto, assistant professor, Hisao Yoshida laboratory, Kyoto University, for his instructive discussions, warmhearted advices, and continual encouragement.

The author sincerely thanks to Dr. Eri Fudo, Prof. Atsuhiro Tanaka, and Prof. Hiroshi Kominami at Kindai University for technical support of TEM observation in Chapter 3.

The author expressed my great appreciation to Prof. Teppei Yoshida, Dr. Daiki Ootsuki, Prof. Tatsuhisa Kato, Prof. Naoki Komatsu, at the Graduate School of Human and Environmental Studies, Kyoto University, for technical support and valuable comments. The author expressed my great appreciation to Prof. Tomoko Yoshida at Osaka City University for technical support, valuable suggestions, warmhearted advices and cheerful messages. The author expressed my great appreciation to Prof. Akira Uedono at Tsukuba University for technical support and fruitful discussion on my research.

Special thanks to Prof. Setsuhisa Tanabe and Prof. Toshihiro Nakamura at the Graduate School of Human and Environmental Studies, Kyoto University, for their valuable comments to much improve this dissertation.

The author expresses my gratitude to Mr. Naoto Fukuo and Mr. Kenji Fujiwara for their significant contribution and extensive discussions on the study. The author expresses my appreciation to Dr. Xing Zhu, Mr. Surya Pratap Singh, Ms. Tomoko Ishii, Dr. Tayyebeh Kalat Soltani, and Dr. Ahmed Hammad, who were colleagues of the laboratory, and gave me chances to collaborate and many supports, and credited me as a co-author.

The author thanks to Mr. Shimpei Naniwa, who was a colleague of the laboratory, for his helpful discussions and advices. The author thanks to Dr. Muneaki Yamamoto and Mr. Masato

Akatsuka at Osaka City University for discussion at the conference and meeting. The author thanks to Lab Secretary Ms. Yuri Bonnitcha for their kind official supports. The author is grateful to all the members, previous and current, of the Hisao Yohida laboratory.

Finally, the author sincerely thanks to my parent, Misao Anzai for understanding, support, and encouragement throughout my student life.

Akihiko Anzai

Kyoto, Japan
30th January

※　著作権等

1. Akihiko Anzai, Naoto Fukuo, Akira Yamamoto, Hisao Yoshida, Highly selective photocatalytic reduction of carbon dioxide with water over silver-loaded calcium titanate, Catalysis Communications, 100 (2017) 134‑138. [DOI:10.1016/j.catcom.2017.06.046]
2. Akihiko Anzai, Kenji Fujiwara, Akira Yamamoto, Hisao Yoshida, Platinum-loaded lanthanum-doped calcium titanate photocatalysts prepared by a flux method for photocatalytic steam reforming of methane, *Catal. Today,* 352 (2020) 1-9. [DOI:10.1016/j.cattod.2020.02.027]